Louisiana State University
LSU Scholarly Repository

LSU Doctoral Dissertations | Graduate School

2013

Luminescence studies : Part I. Lanthanide nanoGUMBOS Part II. Near infrared photothermal nanoGUMBOS

Jonathan Carver Dumke
Louisiana State University and Agricultural and Mechanical College

Follow this and additional works at: https://repository.lsu.edu/gradschool_dissertations

 Part of the Chemistry Commons

Recommended Citation

Dumke, Jonathan Carver, "Luminescence studies : Part I. Lanthanide nanoGUMBOS Part II. Near infrared photothermal nanoGUMBOS" (2013). *LSU Doctoral Dissertations*. 1981.
https://repository.lsu.edu/gradschool_dissertations/1981

This Dissertation is brought to you for free and open access by the Graduate School at LSU Scholarly Repository. It has been accepted for inclusion in LSU Doctoral Dissertations by an authorized graduate school editor of LSU Scholarly Repository. For more information, please contactgradetd@lsu.edu.

LUMINESCENCE STUDIES:
PART I. LANTHANIDE NANOGUMBOS
PART II. NEAR INFRARED PHOTOTHERMAL NANOGUMBOS

A Dissertation

Submitted to the Graduate Faculty of the
Louisiana State University and
Agricultural and Mechanical College
in partial fulfillment of the
requirements for the degree of
Doctor of Philosophy

in

The Department of Chemistry

by
Jonathan Carver Dumke
B.S., Hillsdale College, 2006
May 2013

To my best friend, Alyce for your love and interest in my passion, and for your sedulous support through this meritorious endeavor; To my parents, Carver and Allison for your love and encouragement throughout my life to constantly strive to be better; To my sister, Kendra for giving me the confidence to pursue a degree in chemistry

To Grammy-Mom and Al, for knowing how to make me laugh; To Grandfather, for telling me that I deserve only the best; To Grandpa and Grandma Dumke, for your humorous 'Manhattan Project' encounter and motivation

To all of my teachers, professors, and advisors for their strenuous efforts in molding me into the educated person that I am today

To Pelé, for making me smile when I feel stress;

To Marlowe, for your amazing friendship

and

My Friends

Acknowledgements

There have been many amiable benefactors upon completion of this work:

Professor Isiah M. Warner: You have taught me how to persevere through challenges through dedication and determination. Because of your mentoring, I have gained confidence in myself. Without your belief in me and father-like persona, I doubt that I would have reached the Ph. D. educational level. I am extremely thankful for your comfort and concern for my well-being when it was needed most. I am also grateful for your financial support, because of which, you encouraged exploration in research to further learn and explore.

Professor Daniel J. Hayes: Your constructive "blunt" criticism was extremely helpful in completion of my research. I value your suggestions and our meetings in regards to the biological aspect of the research. You are a great mentor and friend.

Professors William Crowe and Andrew Maverick: In great regard I cherish our discussions and your warm-heartedness.

Professor Bilal El-Zahab: Your friendship and research guidance were paramount.

Drs. Leonard Moore Jr. and W. Adam Phelan: Your friendship was much appreciated, since it sustained my sanity.

Drs. Susmita Das, Noureen Siraj, Vivian Fernand, and Farhana Hasan: Your suggestions and assistance were welcomed during our discussions.

High School and Undergraduate Chemistry Professors: For not giving up on me while I struggled in your class and making nitrogen triiodide just for fun.

The Warner Research Group: I appreciate the helpful research discussions, conference road trips, and random lunches/night-outs being my Louisiana family.

Funding Agencies: Major funding came from National Institutes of Health, National Science Foundation, and the Philip W. West Endowment.

Table of Contents

Acknowledgements iii

List of Tables vii

List of Figures viii

List of Schemes xiii

List of Abbreviations xiv

Abstract xvii

Chapter 1. Introduction

1.1 Nanotechnology 1
1.1.1 Brief Historical Account of Nanomaterial Applications 1
1.1.2 Primitive Characterizations of Nanomaterials 1
1.1.3 Buckminsterfullerenes and Microtubules 2
1.1.4 Nanomaterials Synthesis 4
1.1.5 Aerosol and Reprecipitation Nanoparticle Techniques 5
1.1.5.1 Aerosol Nanoparticle Techniques 5
1.1.5.2 Sonochemical Reprecipitation Nanoparticle Technique 6
1.1.5.3 Microwave Reprecipitation Nanoparticle Technique 6
1.1.6 Applications of Nanomaterials 8
1.1.7 Microscopy of Nanomaterials 9
1.2 Molten Salts to GUMBOS 10
1.2.1 Ionic Liquid Overview 10
1.2.2 Brief Account of Ionic Liquid Origin 10
1.2.3 Applications of Ionic Liquids 12
1.2.4 Group of Uniform Materials Based on Organic Salts 13
1.2.4.1 Organic Salts Applications 15
1.3 Rare Earth Metals 15
1.3.1 Background of Rare Earth Metals 15
1.3.2 Luminescence Spectroscopy of Rare Earth Metals 17
1.3.3 Instruments for Spectroscopy 21
1.3.3.1 Absorption Spectrometry 21
1.3.3.2 Photophysical Spectrometry 22
1.3.4 Applicable Uses of Rare Earth Metals 24
1.3.5 Rare Earth Metals and Ionic Liquids 25
1.4 Hyperthermia as a Therapeutic 26
1.4.1 Hyperthermal Therapeutics in Antiquity 26
1.4.2 Induced Fever as a Cancer Hyperthermal Therapeutic 27
1.4.3 Early Hyperthermal Therapeutics 28
1.4.4 Infrared Spectrum 29
1.4.5 Light Amplification by Stimulated Emission Radiation 30

1.4.5.1 Brief Background on LASER Origins 30
1.4.5.2 LASER Components 31
1.4.6 Laser Hyperthermal Cancer Therapeutics Techniques 32
1.4.6.1 Laser Photothermal Origins 32
1.4.6.2 Near-Infrared Transparency of Human Tissue 33
1.4.7 Nanomaterials Used as a Hyperthermal Therapeutic 34
1.4.7.1 Hyperthermal Cancer Therapeutic Using Gold Nanomaterials 35
1.4.7.2 Hyperthermal Cancer Therapeutic Using Carbon Nanotubes 35
1.4.8 Magnetic Hyperthermal Method 35
1.5 Scope of Dissertation 36
1.6 References 37

Chapter 2. Lanthanide-Based NanoGUMBOS
2.1 Introduction 50
2.2 Synthesis and Characterization of Europium (III) GUMBOS and NanoGUMBOS 51
2.2.1 Synthesis and Characterization of Europium (III) GUMBOS 51
2.2.2 Synthesis and Characterization of Europium (III) NanoGUMBOS 53
2.3 Spectral Properties of Europium (III) GUMBOS and NanoGUMBOS 55
2.3.1 Calculation of Förster Resonance Energy Transfer (FRET) Parameters 55
2.4 Spectral Properties of the GUMBOS, $[C_6mim][Eu(tta)_4]$ and Derived Nanoparticles 57
2.4.1Absorbance Measurements of GUMBOS and NanoGUMBOS 57
2.4.2 Luminescence Measurements of GUMBOS and NanoGUMBOS 58
2.4.2.1 Imidazolium Fluorescence Influence 60
2.4.2.2 Förster Resonance Energy Transfer 62
2.4.2.3 Photostability and Lifetime Decay 64
2.5 Conclusion 66
2.6 References 66

Chapter 3. Photothermal Response of Near-Infrared NanoGUMBOS
3.1 Introduction 71
3.2 Experimental 73
3.2.1 Materials 73
3.2.2 Characterization 73
3.2.3 Synthesis of GUMBOS and NanoGUMBOS 74
3.2.4 Laser Irradiation 75
3.3 Results and Discussion 75
3.3.1 Characterization of NIR GUMBOS and NanoGUMBOS 75
3.3.1.1 [1048][Deoxycholate] 76
3.3.1.2 [1048][Ascorbate] 78
3.3.1.3 [1061][Deoxycholate] 80
3.3.1.4 [1061][Ascorbate] 82
3.4 Photospectral Characteristics of GUMBOS & NanoGUMBOS 83
3.5 Photothermal Characteristics 85
3.6 Band Gap Calculations 91
3.7 Conclusion 92
3.8 References 92

Chapter 4. Tumor-Targeting Hyperthermal Near-Infrared NanoGUMBOS
4.1 Introduction....97
4.2 Materials and Characterization....98
4.2.1 Materials....98
4.2.2 Characterization....99
4.2.3 Synthesis of GUMBOS and NanoGUMBOS....99
4.3 Methods....100
4.3.1 Laser Irradiation....100
4.3.2 Cytotoxicity/NanoGUMBOS Control....101
4.3.3 NIR Laser Irradiation Control....101
4.3.4 Hyperthermal Technique....102
4.3.5 Fluorescence Microscopy....102
4.3.6 Cellular Uptake....102
4.4 Results....103
4.4.1 NIR NanoGUMBOS Characterization....104
4.4.2 NIR NanoGUMBOS Cytotoxicity....105
4.4.3 Laser Irradiation Cytotoxicity....106
4.4.4 Laser Irradiation Photothermal Response....107
4.4.5 Hyperthermia Cancer Therapeutic....109
4.4.6 Cellular Uptake of NIR NanoGUMBOS....112
4.5 Conclusion....113
4.6 References....113

Chapter 5. Conclusion and Future Studies
5.1 Concluding Remarks....117
5.2 Future Studies....118

Appendix 1. Supplemental Information for Chapter 3....120

Appendix 2. Supplemental Information for Chapter 4....129

Appendix 3. Letters of Permission....133

Vita....134

List of Tables

Table 1.1 The loss tangent is a function of a solvents ability to absorb and convert energy into heat....8

Table 1.2 Ground state term symbols for trivalent lanthanides according to Hund's rule 20

Table 1.3 Variable gain media towards the production of high-intensity output results in different wavelengths of radiation emission. Adapted from reference 149....31

Table 2.1 Elemental analysis (CHNOFS-results) of the dry GUMBOS including the theoretical element percentage of the elements with the β-diketonate chelated to the europium (III) (i.e. GUMBOS and nanoGUMBOS) and if there was not chelation. The percent difference supports that the β-diketone chelates to the europium (III)....53

Table 2.2 The overlap integral (J) and energy transfer efficiency (E) from donor (C_6mim^+) to acceptor (Eu^{3+}) in a 1:1 ratio....56

Table 3.1 A compiled list of the [1048] nanoGUMBOS spectral and morphological characteristics for [Deoxycholate] and [Ascorbate], respectively, show a trend of aggregation and zeta-potential with an increased pH media. The bold lines represent the divisions of pKa values 80

Table 3.2 A compiled list of the [1061] nanoGUMBOS spectral and morphological characteristics for [Deoxycholate] and [Ascorbate], respectively, show a trend of aggregation and zeta-potential with an increased pH media. The bold lines represent the divisions of pKa values 83

Table 3.3 The heat capacities (Cp) for the GUMBOS were experimentally determined in triplicate by a modulated DSC instrument....90

Table 3.4 Photothermal efficiency (η) increases as band gap energy (eV) decreases due to the GUMBOS electron withdrawing groups....92

Table 4.1 The NIR nanoGUMBOS were monodisperse under microwave-assisted reprecipitation synthesis....104

Table 4.2 NIR nanoGUMBOS remained significantly insoluble in an aqueous suspension media....105

Table 4.3 The percent of nanoGUMBOS were calculated by difference in absorbance from the control (10% dissolved in DMSO) and from the concentration gradient equation (%Slope)....112

List of Figures

Figure 1.1 Nanowires forged into (A) Damascus swords ranged in (B) several hundred nanometers in length and 10 – 40 nm in diameter. Obtained from references 4 and 6, respectively 1

Figure 1.2 (A) Smoke particles, MgO, (B) fine particles, $AuCl_3$, and, (C) fibers, chrysotile asbestos, were imaged with a primitive electron microscope at 20,000 – 50,000 times the resolution of the human eye. Obtained from reference 14 2

Figure 1.3 Nanomaterials to perform work have become of great interest to researchers since Iijim's microtubules in 1991 3

Figure 1.4 Graphitic carbon microtubules that were discovered by Iijima in 1991 had varying diameters and layers: [a] 6.7 nm five-sheet, [b] 5.5 nm two-sheet, and [c] 6.5 nm (2.2 nm internal diameter) seven-sheet. Obtained from reference 20.....4

Figure 1.5 The aerosol method of fabricating nanoparticles is made up of eight components (A) air filter and pressure control, (B) nebulizer and sample reservoir, (C) silica gel dryer to remove moisture, (D) electrostatic classifier to neutralize the particles, (E) oven to dry off solvent, (F) flow direction valve, (G) sample collection onto a membrane, and (H) particle size & counter 5

Figure 1.6 Traditional and transmission electron microscopes have similar instrumentation design 9

Figure 1.7 Phase diagram of different mole percent ratios of aluminum chloride fused with ethyl pyridinium bromide, $AlCl_3$:[Etpyr][Br], shows a variable melting point trend (1:2 = 45 °C, 1:1 = 88 °C, and 2:1 = -40 °C). Obtained from ref 68 11

Figure 1.8 Research interest was low for these salts until Wilkes demonstrated metathesis with organic anions in his 1992 article 12

Figure 1.9 Properties and fabrication of GUMBOS and nanoGUMBOS have many opportunities 13

Figure 1.10 Mendeleev's attempt to of the periodic table shows confusion of where to place the lanthanide elements. Adapted from reference 88.....15

Figure 1.11 The atomic orbitals (s, p, d, and f) in Cartesian coordinates with magnetic quantum numbers, *ml*, are listed from largest to smallest.....16

Figure 1.12 Jabloński's (A) original diagram in 1933 and (B) modern diagram ~80 years later both similarly show a visualization for luminescence studies 18

Figure 1.13 A Jabloński diagram is used to represent lanthanide (i.e. europium) emission via antenna effect. (Note: Relaxation energies are not to scale.).....18

Figure 1.14 Photophysical spectra of europium (Eu^{3+}) reveals energy level term symbols for absorbance and luminescence. (I.) Spectra of aqueous 0.100 M $EuCl_3$ for absorbance and 0.8 µM Eu(thenotrifluoroacetone)$_3 \cdot 2H_2O$ in acetonitrile for luminescence. (II.) and (III.) are enlarged regions of spectra for absorbance and luminescence, respectively 19

Figure 1.15 A typical double-beam absorbance instrument was used to measure the absorbance of the solute in solvents.....21

Figure 1.16 Spectrofluorometer instrument is used to measure the luminescence intensity from a sample 23

Figure 1.17 The harsh methods of hyperthermal treatment by use of (A) pokers and (B) electrocautery treatments were primarily used 400 BC – 1800 AD and 1800-1900 AD, respectively. Obtained from references 118 and 120, respectively 27

Figure 1.18 Wavelengths (in nanometers) become longer and lesser energetic from left-to-right in the electromagnetic spectrum. (Note: Not to scale.) 28

Figure 1.19 The apparatus used by Herschel in 1800 was designed to measure radiant heat from refrangible invisible rays immediately beyond the prismatic spectrum. (A) and (B) are the stands used to hold the three thermometers, (C) and (D) are the prism, and (E) is the visible spectrum. Obtained from reference 137 29

Figure 1.20 Schematic of Townes' microwave amplification by stimulated emission radiation instrument was originally developed to be a high-resolution microwave spectrometer. Obtained from reference 145.....30

Figure 1.21 Hyperthermal therapeutics became more popular since the invention of the MASER in 1954.....32

Figure 1.22 The optical penetration depth (mm) of human skin is highest in the near infrared region. Obtained from reference 138 33

Figure 1.23 Nanomaterials studied *in vitro* and *in vivo* were used in concert with infrared laser irradiation hyperthermia as a cancer therapeutic. (A) Nanomaterial control, (B) saline control, (C) laser control, and (D) nanomaterials and laser. Obtained from references 163 and 160, respectively.....34

Figure 2.1 Differential scanning calorimetry melting point of the GUMBOS, [C_6mim][Eu(tta)$_4$] 52

Figure 2.2 TEM image of $[C_6mim][Eu(tta)_4]$ nanoGUMBOS prepared using the aerosolization process. The particles had an average diameter of 39.5 ± 8.4 nm 54

Figure 2.3 XPS spectra of the $[C_6mim][Eu(tta)_4]$ dry GUMBOS (gray) and dry nanoGUMBOS (black) 54

Figure 2.4 Energy transfer was observed from the $[C_6mim]$ to the europium (III) in aqueous (A) and ethanol (B) solutions. Concentrations of pure 0.5 M $[C_6mim]$ (dotted line) and pure 0.5 M europium (III) (dashed line) were compared to show that the mixture (bold line) had higher europium (III) emission intensity 56

Figure 2.5 Absorption of 0.1 M $EuCl_3$ dissolved in water 57

Figure 2.6 Absorbance spectra of the aqueous suspension of nanoGUMBOS (solid line) and a 0.8 μM ethanol solution of GUMBOS (dashed line) 58

Figure 2.7 (A) Excitation-Emission Matrix (EEM) of (A) 0.8 μM GUMBOS dissolved in ethanol and (B) nanoGUMBOS suspension in water. Emissions between 250-400 nm and 500-650 are due to second-order scattering 59

Figure 2.8 Excitation (340 nm, dashed line) and emission (613 nm, solid line) spectra of GUMBOS and nanoGUMBOS. (A) 0.8 μM GUMBOS dissolved in ethanol, (B) nanoGUMBOS suspension in water, and (C) GUMBOS dissolved in liquid $[C_6mim][Tf_2N]$ 61

Figure 2.9 Normalized emission spectra of GUMBOS dissolved in ethanol (solid) and $[C_6mim][Tf_2N]$ (dash), and nanoGUMBOS in water (dot) while focusing on the emissions directly from (A) [C6mim] and (B) europium (III) when excited at 340 nm. (Note: The ethanol Raman peaks were removed for clarity.) 62

Figure 2.10 Energy transfer was observed from the $[C_6mim]$ to the europium (III) as dissolved GUMBOS in ethanol (A) and suspended nanoGUMBOS in water (B) when excited at the absorption maxima (340 nm, dashed line) and absorption minima (395 nm, bold line) with slit widths at 5 nm 63

Figure 2.11 Time-domain europium (III) emission decay time of aerosolized nanoparticles, $[C_6mim][Eu(tta)_4]$, resuspended in water 65

Figure 3.1 Representative TEM images of [1048][Deoxycholate] NIR nanoGUMBOS prepared in different pH media yielded different sizes and shapes (scale bars are 100 nm) 76

Figure 3.2 TEM images of [1048][Ascorbate] NIR nanoGUMBOS prepared in different pH media yielded different sizes and shapes (scale bars are at 100 nm) 79

Figure 3.3 The NIR nanoGUMBOS, [1061][Deoxycholate] prepared in different pH media yielded different sizes and shapes (scale bars are at 100 nm).....81

Figure 3.4 The NIR nanoGUMBOS, [1061][Ascorbate] prepared in different pH media yielded different sizes and shapes (scale bars are at 100 nm).....82

Figure 3.5 The GUMBOS were dissolved in acetone at a concentration of 80 μM and absorbance normalized. (A) [1048] GUMBOS maxima were, respectively, 1035 and 1045 nm. (B) [1061] GUMBOS apexes were at 1045 nm.....84

Figure 3.6 The [1048] nanoGUMBOS showed spectral shifts among different pH, while it was difficult to ascertain with the [1061] nanoGUMBOS.....84

Figure 3.7 The nanoGUMBOS showed an inverse parabola trend of absorbance maximum with an increase in pH between the pKa values (grey vertical dashes).....85

Figure 3.8 Photothermal profile of a 4 mg bulk (A) [1048] and (B) [1061] GUMBOS sample under continuous NIR irradiation for five minutes at a 1000 mW shows a dramatic temperature increase 86

Figure 3.9 The absorbance at 1064 nm and photothermal response shows a trend as pH increases among the [1048] nanoGUMBOS.....87

Figure 3.10 The absorbance at 1064 nm and photothermal response shows a trend as pH increases among the [1061] nanoGUMBOS.....87

Figure 3.11 The slope of natural log of the driving force temperature versus time is an integral component for finding the photothermal efficiency of the nanoGUMBOS 89

Figure 4.1 Concentration absorbance at 1000 nm gradient of percent of 77.6 μg mL^{-1} (A) [1048][Folate] and (B) [1061][Folate] nanoGUMBOS in DMSO was used to determine the concentration of nanoGUMBOS that entered the MDA-MB-231 cells 103

Figure 4.2 The NIR nanoGUMBOS TEM micrograph shows particle sizes for (A) [1048][Folate] at 121 ± 32.5 nm and (B) [1061][Folate] at 144 ± 46.8 nm 104

Figure 4.3 Viability studies of (A) [1048][Folate] and (B) [1061][Folate] NIR nanoGUMBOS using an alamarBlue® assay was performed on breast cell lines.....105

Figure 4.4 The LD_{50} was calculated from the linear slope of the cytotoxicity in different cell lines of NIR nanoGUMBOS.....106

Figure 4.5 Laser irradiation over cancerous MDA-MB-231 (MDAs) and noncancerous HS-578-BST (BSTs) were observed.....107

Figure 4.6 Substantial heat was generated from the NIR nanoGUMBOS (A) [1048][Folate] and (B) [1061][Folate] 108

Figure 4.7 [1048][Folate] NIR nanoGUMBOS with MDA-MB-231 breast cancer cells shows live-green and dead-orange controls, nanoGUMBOS control-blue, and hyperthermal (laser and nanoGUMBOS)-red at (A) 10 minute, (B) 20 minute, and (C) 30 minute lasing time intervals.....109

Figure 4.8 [1061][Folate] NIR nanoGUMBOS with MDA-MB-231 breast cancer cells shows live-green and dead-orange controls, nanoGUMBOS control-blue, and hyperthermal (laser and nanoGUMBOS)-red at (A) 10 minute, (B) 20 minute, and (C) 30 minute lasing time intervals.....110

Figure 4.9 A fluorescence microscopy image distinctively shows cell death from the selective area where (A) laser irradiation occurred, (B) did not occur, and (inset) cusp of irradiation/nonirradiation. (Note: the diameter of the laser spot matches the laser focal spot in image, 2 mm.) 111

Figure A3.1 ^{1}H and ^{19}F NMR of the GUMBOS ([1048, 1061][Deoxycholate, Ascorbate]) in d-DMSO 120

Figure A3.2 FT-IR of the nanoGUMBOS synthesized in different pH media suggests that the material is deprotonated with an increasing pH media 124

Figure A4.1 ESI MS of the folate product after synthesis reveals that the folic acid precursor is higher in concentration by two fold. (The inset is a scan on only the folate.) 129

Figure A4.2 ^{19}F NMR was used to observe the anion exchange from the anion precursor [BF_4] to non-fluorinated product [Folate] for the (A) [1048] and (B) [1061] GUMBOS 130

Figure A4.3 Photothermal measurements were recorded by a thermocouple placed about 2 mm above the laser beam 131

Figure A4.4 Incubation of eight hours for 10,000 cells with the alamarBlue® assay was preferred due to the higher fluorescence intensity and smaller standard deviation.....131

Figure A4.5 *In vivo* hyperthermal experiments were conducted in a 96 well-plate.....132

Figure A4.6 Absorbance measurements were conducted for comparison of a fixed concentration (32 μg mL^{-1}) and of the top aqueous layer of post-centrifugation nanoGUMBOS. (A) [1048][Folate] was calculated to be 92.92% insoluble, and (B) [1061][Folate] was calculated to be 88.75% insoluble. Note: Absorbance shoulder between 1150 – 1200 nm was determined to be from the folate anion.....132

List of Schemes

Scheme 1.1 A neutralization method consisting of a Brønsted acid and base was used to synthesize ionic liquids 11

Scheme 1.2 A facile metathesis reaction of ionic liquids and like compounds allow for tailor-made materials 12

Scheme 1.3 GUMBOS synthesis using (A) Lewis acid and base method for 1-Butyl-2,3-dimethylimidazolium chloride and (B) S_N2 reaction for quaternization of hypergolic ionic liquids. Obtained from references 56 and 86 14

Scheme 2.1 Reaction scheme of the formation of $[C_6mim][Eu(tta)_4]$ 52

Scheme 3.1 Metathesis synthesis for the [1048] and [1061] GUMBOS were performed by an anion exchange method 74

Scheme 3.2 The protonation to deprotonation of desired anions (A, Deoxycholate; B, Ascorbate) and respective pKa assist to gain understanding of the nanoGUMBOS structural formation 77

Scheme 4.1 A metathesis reaction exchanging a folate anion with tetrafluoroborate was done in a 1:2 mol:mol ratio 100

List of Abbreviations

Abbreviations	Name
[1048]	4-[2-[2-Chloro-3-[(2,6-diphenyl-4*H*-thiopyran-4-ylidene)ethylidene]-1-cyclohexen-1-yl]ethenyl]-2,6-diphenylthiopyrylium
[1061]	1-Butyl-2-[2-[3-[(1-butyl-6-chlorobenz[cd]indol-2(1*H*)-ylidene)ethylidene]-2-chloro-1-cyclohexen-1-yl]ethenyl]-6-chlorobenz[cd]indolium
AB	Alamar Blue
AD	Anno Domini
ATP	adenosine triphosphate
BC	Before Christ
$-BF_4$	tetrafluoroborate
$[Bmim]^+$	1-butyl-3-methylimidazolium
°C	degree Celsius
C_{60}	buckminsterfullerene
C_p	heat capacity
CNT	carbon nanotube
CRT	cathode ray tube
DCM	dichloromethane
DLS	dynamic light scattering
DMEM	Dulbecco's modified eagle media
DMSO	dimethyl sulfoxide
DNP	2,4-dinitrophenol
EEM	excitation-emission matrix
ESI MS	electrospray ionization mass spectrometry
FIL	frozen ionic liquid

FRET	Förester resonanace energy transfer
FTIR	fourier transform infrared spectroscopy
Γ	orbital angular momentum quantum number
GHz	gigahertz
GPa	gigapascals
GUMBOS	group of uniform materials based on organic salts
Gy	gray
HEPES	4-(2-hydroxyethyl)-1-piperazineethanesulfonic acid
HOMO	highest occupied molecular orbital
IL	ionic liquid
J	total angular momentum quantum number
LD_{50}	median lethal dose
LASER	light amplification by stimulated emission radiation
LED	light emitting diode
LMCT	ligand-to-metal charge transfer
Ln	lanthanide
LUMO	lowest unoccupied molecular orbital
kHz	kilohertz
MHz	megahertz
M_L	total orbital quantum number
M_S	total spin quantum number
MASER	microwave amplified by stimulated emission radiation
NanoGUMBOS	nanoparticles made from a group of uniform materials based on organic salts
NEAA	non-essential amino acid

NIR	near-infrared
nm	nanometer
NMR	nuclear magnetic resonance
OIL	organic ionic liquid
PBS	phosphate buffer saline
RTIL	room temperature ionic liquid
S	spin angular momentum quantum number
S_0, S_1	singlet ground state, first excited state
T_1	excited triplet state
TEM	transmission electron microscope
TSIL	task-specific ionic liquid
Tf_2N	bis(trifluoromethanesulfonyl)imide
tta	2-thenoyltrifluoroacetone (beta-diketone)
UV	ultraviolet
Vis	visible
XPS	X-ray photoelectron spectroscopy

Abstract

Group of Uniform Materials Based on Organic Salts (GUMBOS) are a class of molten salts that have been focused to be specifically tailored towards applications. Primitively, from Davy to Walden molten salts were desirable for organic synthesis due to the properties. GUMBOS have been synthesized into nanoparticles (nanoGUMBOS) by various methods to be used for lanthanide luminescence and hyperthermal cancer therapeutics.

Lanthanide photochemistry has been frequently studied for its high luminescence intensity, narrow emission band, and stable luminescent lifetime decay. Aerosol-derived europium nanoGUMBOS were characterized using electron microscopy (39.5 ± 8.4 nm), XPS, and spectroscopic techniques. Spectroscopic measurements indicated intense and steady luminescence, which suggests a multitude of possible applications for lanthanide-based GUMBOS, especially in sensory and photovoltaic devices.

Several near infrared (NIR) nanoparticles of GUMBOS composed of cationic dyes coupled with biocompatible anions were investigated for their photothermal properties. These nanoparticles were synthesized using a reprecipitation method performed at increasing pH values. The cations for the nanoGUMBOS**,** [1048] and [1061], have absorbance maxima at wavelengths overlapping with human soft tissue absorbance minima. NIR nanoGUMBOS excited with a 1064 nm continuous laser led to heat generation (20.4 ± 2.7 °C) after five minutes. While the [1061][Deoxycholate] nanoGUMBOS generated the highest temperature increase (23.7 ± 2.4 °C), it was the least photothermally efficient compound (13.0%) due to its relatively large energy band gap of 0.892 eV. The energy band gap is a measurement of the HOMO and LUMO distance, and predictor of photothermal efficiency. The more photothermally efficient

compound, [1048][Ascorbate] (64.4%), had a smaller energy band gap of 0.861 eV provided an average photothermal temperature increase of 21.0 ± 2.1 °C.

Hyperthermal therapeutics originating from hot pokers has evolved into facilitation of NIR nanomaterials photothermal response. NanoGUMBOS can employ a variety of curative techniques by pairing fluorescent and biocompatible ions. NanoGUMBOS, [1048][Folate] and [1061][Folate], were evaluated using electron microscopy, spectroscopic, thermal imaging, and fluorescent assays. In order to generate highly responsive nanomaterials for NIR-laser-triggered hyperthermia, optimization of nanoparticle size, shape, and uniformity were investigated.

Chapter 1. Introduction

1.1 Nanotechnology

1.1.1 Brief Historical Accounts of Nanomaterial Applications

Nanomaterials were unknowingly created amidst the fabrication of ruby glass (containing gold nanoparticles)[1] and shears (containing nanorods) during the Roman province of Egypt (30 BC – 639 AD).[2] The nanomaterials in the shears were presently identified to be short rods, or grain-like structures, of iron carbonitrides (i.e. cementite, Fe_3C) and martensite.[2-3] The multiwalled carbon nanotubes enveloping cementite nanowires were measured to be about 10 – 40 nm in diameter (Figure 1.1).[4-5] These nanomaterials drastically increased the strength of the Damascus sword as it was reported that cementite nanowires had a hardness of 12 GPa compared to regular steel matrix of 2.5 GPa.[6]

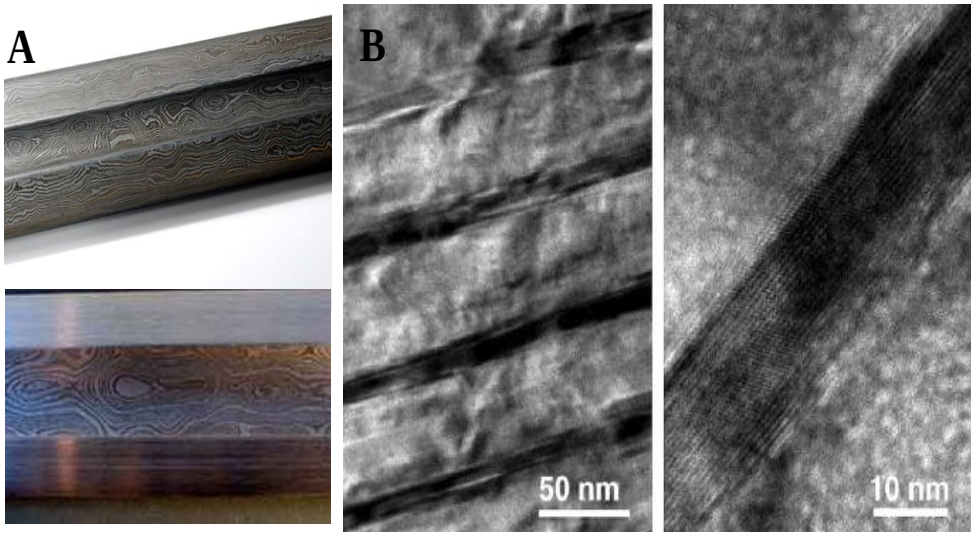


Figure 1.1. Nanowires forged into (A) Damascus swords ranged in (B) several hundred nanometers in length and 10 – 40 nm in diameter. Obtained from references [4] and [6] respectively.

1.1.2 Primitive Characterizations of Nanomaterials

In the early 1900s, materials now referred to as nanoparticles were called "fine particles," "dust/smoke particles," or "colloids."[7-9] These particles were being researched and observed by

spectroscopic techniques (e.g. light scattering),[7] and measured by extensive calculations[9] or centrifugal methods[10-11] until a suitable microscope was developed in 1931.[12] The microscope known as the electron microscope was first described as a cathode ray oscilloscope by Max Knoll and Ernst Ruska.[13] A couple of the smoke particles (e.g. ZnO and MgO) and gold particles analyzed ranged from 30 to 2000 Å (Figure 1.2).

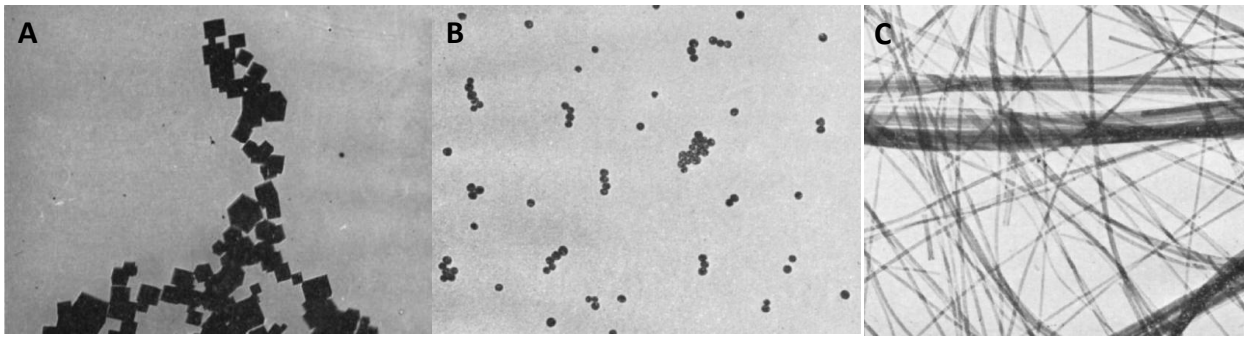


Figure 1.2. (A) Smoke particles, MgO, (B) fine particles, $AuCl_3$, and, (C) fibers, chrysotile asbestos, were imaged with a primitive electron microscope at 20,000 – 50,000 times the resolution of the human eye. Obtained from reference [14].

1.1.3 Buckminsterfullerenes and Microtubules

An American physicist named Richard Feynman proposed the idea of manipulating individual atoms to perform mechanical and chemical synthesis in his famous December 29, 1959 CalTech lecture, "There's plenty of room at the bottom."[15] Richard Feynman's lecture is considered to be the critical moment when researchers began to take more interest in the sub-micron world. The hype from his lecture thus began feverish studies of materials in the "very, very small world." The term, "nanotechnology" was coined in 1974 when a Tokyo Science University professor, Norio Taniguchi, was describing silicon machining smaller than one micron.[16]

Presently, the definition of "nano" in the context of materials is any substance that is smaller than 100 nm, otherwise materials greater than 100 nm use the prefix "meso." The first article to use the prefix "nano" was titled, "Colloids Distribution Conditions in the

Pharmaceutical Technology: Coacervation, Adsorption, and Micelle Polymerization" in 1976 by Swiss researchers at the Federal Institute of Technology in Zurich.[17-18] Since then, more than 350,000 articles have been published up-to-date concerning nanomaterials (Figure 1.3). Many of these articles on nanomaterials cover a multitude of subject areas from biomedical, sensors, lithography, energy conversion and storage, and separations.

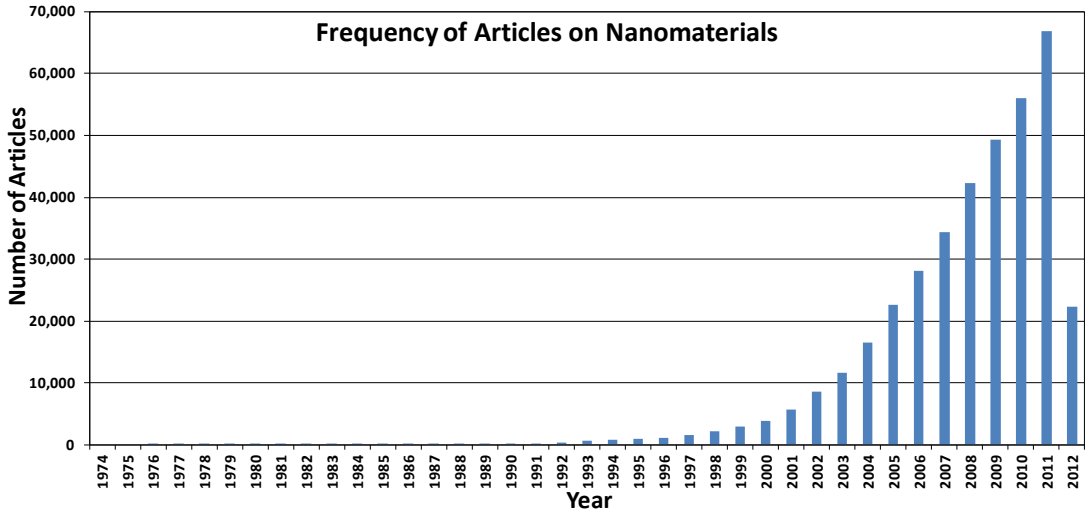


Figure 1.3. Nanomaterials to perform work have become of great interest to researchers since Iijim's microtubules in 1991.[a]

The most popular of all articles concerning nanomaterials (cited ~8,000 times) was the discovery and characterization of the ~7 Å buckminsterfullerene, C_{60}, by Richard Smalley in 1985 from Rice University.[19] This research was the breakthrough needed for Sumio Iijima to characterize the C_{60} cousin, the helical graphitic carbon "microtubules" in 1991 (Figure 1.4).[20] Today, Iijima's premier article on ~5.5 – 6.7 nm diameter carbon nanotubes has been referenced over 13,000 times. With the synthesis of the C_{60} and carbon "microtubules," researchers began to synthesize nanostructures of variable shapes and of different components for mechanical purposes.

[a] Histogram was derived from article frequency searching the following key phrases in the "Web of Knowledge" database: nano -wire, -particle, -tube, -shell, -drop, -film, -caps.

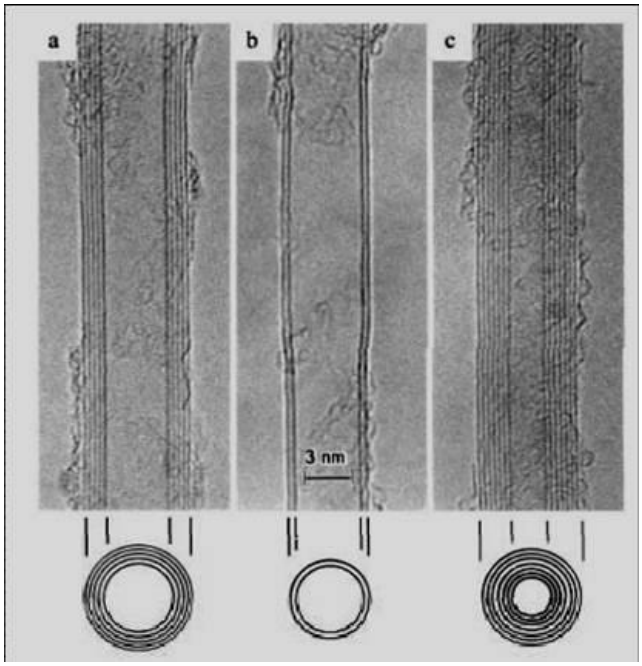


Figure 1.4. Graphitic carbon microtubules that were discovered by Iijima in 1991 had varying diameters and layers: [a] 6.7 nm five-sheet, [b] 5.5 nm two-sheet, and [c] 6.5 nm (2.2 nm internal diameter) seven-sheet. Obtained from reference [20].

1.1.4 Nanomaterials Synthesis

The synthesis of carbon nanostructures was the ignition needed for researchers to manipulate materials into the nanoscale. Carbon nanotubes (CNTs) are studied as either single-walled (SWCNT) or multi-walled (MWCNT). The excitement behind these sp^2 carbon structures is due to the application versatility, abundance, ease of synthesis, and physical properties.[21-23] Comprehensive research of CNT applications is in biomedical,[24-25] energy conversion,[26-27] circuits,[28] composites,[29] and chemical sensing.[30] Excitement over CNTs physical properties is the driving force for research on these multifaceted carbon graphene tubes.[22, 31] These properties would include 20 times the tensile strength of steel at 300 GPA[32] and more efficient electrical conductivity.[33]

The discovery and overwhelming use of graphene nanomaterials led researchers to manipulating other compounds into the nanoregime to perform mechanical work. Other than

graphene, silica and gold have been studied more than 60,000 and 55,000 times since 1989, respectively. The other common compounds synthesized into nanomaterials include: metal complexes (i.e. silver, copper, iron oxides), metal alloys (CdSe/ZnS, $CdTe_{1-X}Se_X$), liposomes, micelles, dendrimers, and polymer.[34] These compounds were synthesized into nanomaterials by various methods: laser ablation,[35] electric arc discharge,[36] vapor deposition,[37] aerosol,[38] electrospinning,[39] templating, seeding, reprecipitation, emulsion, and surfactant-based.[37, 40]

1.1.5 Aerosol and Reprecipitation Nanoparticle Techniques

1.1.5.1 Aerosol Nanoparticle Technique

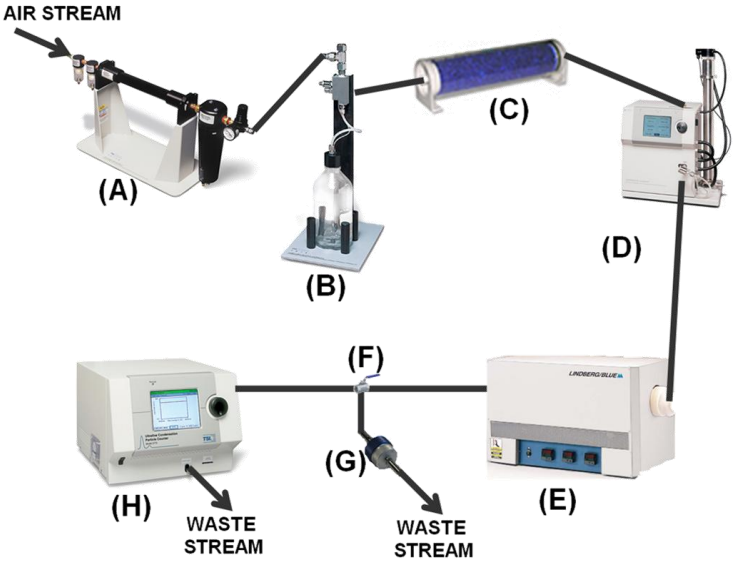


Figure 1.5. The aerosol method of fabricating nanoparticles is made up of eight components (A) air filter and pressure control, (B) nebulizer and sample reservoir, (C) silica gel dryer to remove moisture, (D) electrostatic classifier to neutralize the particles, (E) oven to dry off solvent, (F) flow direction valve, (G) sample collection onto a membrane, and (H) particle size & counter.

The various aforementioned methods in which to fabricate nanomaterials continues to be aggressively researched (including an attempt by the author) throughout academia and industry. However, in regards to this monograph, methods to synthesize nanoparticles were performed by aerosol and co-precipitation methods. Fabrication of nanoparticles by aerosol is a relatively facile exercise as long as the instrumental setup is properly installed (Figure 1.5). The bulk

sample must first be dissolved and connected to a nebulizer. The air pressure and oven is adjusted to optimize the size of nanoparticles. The solution of the material is placed under pressure to nebulize through a chamber connected to a moisture drying component. The air pressure continuously carries the nebulized solvent through an oven to dry off the solvent before being collected onto a membrane filter.

1.1.5.2 Sonochemical Reprecipitation Nanoparticle Technique

Reprecipitation methods for synthesizing nanoparticles have various techniques with the intent on precipitating the desired nanoparticles. These diverse procedures that have been attempted use two solvents for precipitation methods include (1) two miscible solvents with a sample that is soluble in one of the solvents, (2) two immiscible solvents with a sample that is soluble in one of the solvents, and (3) two immiscible solvents with soluble reactants that become insoluble in both solvents as a product. The reprecipitation method (1) was found to yield the more spherical and polydisperse nanoparticles, especially when assisted by an ultrasonic sonicator. This particular method is performed by dissolving the sample (e.g. in acetone), and then adding a small aliquot of the sample to the miscible/insoluble solvent (e.g. water). The insoluble sample gravitates toward cavitation ("bubble") sites which are created during sonication (20 kHz to 100 MHz).[41] Nanoparticles are formed when chemical bonds break (less than a nanosecond) resulting in the "bubble" collapsing. Crystallization of nanoparticles does not usually occur due to the high cooling rate. Another instrument which was used along with the reprecipitation method (1) was a microwave apparatus.

1.1.5.3 Microwave Reprecipitation Nanoparticle Technique

Microwave irradiation employs internal heating of a sample by two different ways: dipolar polarization and ionic conduction.[42] Dipolar polarization is the process of polar

solvent/reagents aligning to the microwave frequency (2.45 GHz) of the applied electric field. Oscillation of the alternating electric field forces the molecules to constantly realign resulting in molecular friction and dielectric heating. The microwave frequency of 2.45 GHz is the optimum frequency for molecules to not realign too quickly (lower frequency) or slowly (higher frequency) which would lead to insufficient heating. The other mode of heating by microwave irradiation, ionic conduction, is from charged particles in the sample. The ionic particles influenced under the alternating applied electric field create collisions with other particles resulting in heat.

The amount of thermal energy that samples and solvent create to uniformly heat a solution can be theoretically determined from the loss tangent factor (tan δ).

$$tan\delta = \frac{e''(dielectric\ heat\ loss)}{e'(dielectric\ constant)} \qquad \text{Equation 1.1}$$

This ratio of the efficiency of microwave frequency [converted to thermal energy (e'')] and the polarity of the molecules (e') provides an expression of the efficiency of electric absorption and heating. Generally, the more polar solvents have a higher loss tangent than lesser polar solvents when measured at room temperature (Table 1.1).[42] A study of the loss tangent at temperatures higher than a solvents boiling point revealed a decrease in the solvents capability to absorb and heat. Ethanol decrease in tan δ is attributed to the solvents change in viscosity (i.e. liquid-to-gas phase change), thus reducing friction from the molecules attempting to align with the applied electric field under dipolar polarization heating. Alternative solvents such as ionic liquids (*vide infra*), 1-butyl-3-methylimidazolium hexafluorophosphate or [Bmim][PF_6], are heated from ionic conduction due to being composed of charged ions. Friction among the molecules aligning to the electric field will not decrease due to a lack in boiling point for ionic liquids. Ionic liquids are efficient absorbers of heat and microwave frequencies among other extensive useful properties.

Table 1.1. The loss tangent is a function of a solvent's ability to absorb and convert energy into heat.

	at 20 °C	at 100 °C	at 200 °C
Solvent	**tan δ**		
Ethanol	0.941	0.270	0.080
DMSO	0.825	-	-
Methanol	0.659	-	-
[BMIM][PF_6]	0.185	1.804	3.592
DMF	0.161	-	-
Water	0.123	-	-
Acetonitrile	0.062	-	-
Acetone	0.054	-	-
Toluene	0.040	-	-
Hexane	0.020	-	-

1.1.6 Applications of Nanomaterials

Since Richard Feynman's inspirational talk, there have been numerous task-specific nanomaterials performing work. The most common nanomaterial, carbon nanotubes (CNTs), has been used in scientific research ranging from energy[43] to biomedical.[44] Energy research, such as optoelectronics, circuits, and thermoelectrics, was conducted using CNTs because of the high thermal (6 kW K^{-1} m^{-1})[45] and electrical conductivities (2.5 – 4.0 kS m^{-1}).[46] Biomedical research using CNTs comprised of functional compounds (e.g. fluorescent, magnetic, cancer-killing, or biocompatible). In order to synthesize functional compounds covalently to pristine CNTs, the graphene microtubulars were oxidized by an acidic solution (e.g. HNO_3) to create carboxylic acid sites.

Another widely used nanomaterial is gold nanoparticles. Gold nanoparticles have been functionalized by reduction of gold (III) in a thiol solution. Functionalized gold nanoparticles have been used as biomarkers and for biomedical therapeutics.[1] Gold nanoparticles inherently have a Mie scattering excitation peak around 530 nm and surface plasmon absorption in the near infrared spectrum (700 – 1000 nm). A change in diameter for gold nanoparticles will shift the surface plasmon absorption wavelength either red or blue (larger or smaller particles, respectively).

Gold nanoparticles and CNTs have been extensively used in biomedical research as biomarkers and/or drug delivery. An example of these nanomaterials used in therapeutics is hyperthermia for the destruction of cancerous tumors. The nanomaterials would absorb and release thermal energy (~42 – 60 °C) when irradiated by a near infrared laser.

1.1.7 Microscopy of Nanomaterials

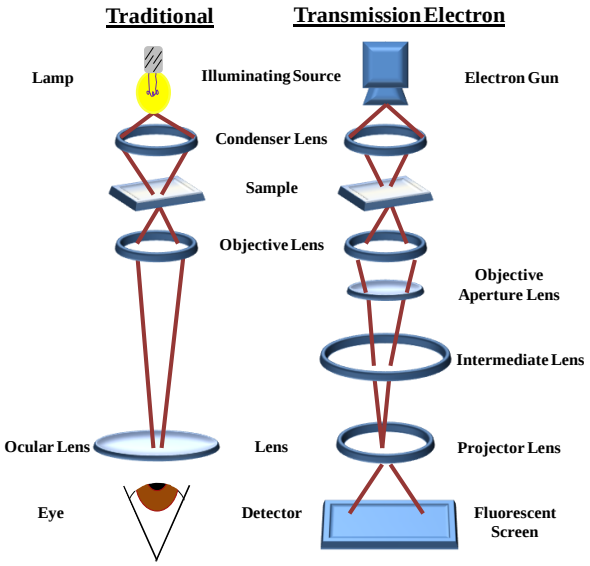


Figure 1.6. Traditional and transmission electron microscopes have similar instrumentation design.

The most common instrument to observe nanomaterials is a transmission electron microscope (TEM). TEM uses an electron gun as an "illuminating source" to be able to produce electron micrographs as seen in figures 1.1, 1.2, and 1.4. Electron guns are capable of producing 5 – 400 keV which is proportional to higher resolution and magnification of nanomaterials. Similar to traditional microscopes, the sample specimen for TEM is close to the "light source" (Figure 1.6). The sample is drop-casted onto a carbon grid (usually copper coated) and placed in a high vacuum prior to electron gun irradiation. The sample absorbs electrons during electron gun irradiation while the electrons not in the path of the sample pass freely to the fluorescent screen.

1.2 Molten Salts to GUMBOS

1.2.1 Ionic Liquid Overview

Scientific research interests occur cyclically due to reoccurring curiosity from new-supporting discoveries. Molten organic salts are not any different from this happenstance. Over centuries molten salts[47] have been called sirups [*sic*],[48] oils,[49] ionic liquids (IL),[50] room temperature ionic liquids (RTIL),[51-52] organic ionic liquids (OILs),[53] frozen ionic liquids (FIL),[54-55] and a group of uniform materials based on organic salts (GUMBOS).[56] In order to learn the origin of these "green" compounds it is first necessary to list the characteristics.[57-59] Presently, the definition of ionic liquids are molten salts with a defined melting point less than 100 ^{o}C.[60] Sodium chloride is considered a molten salt above 800 ^{o}C, when the cubic crystal lattice breaks down and becomes a liquid.[61] Ionic liquids and molten salts have been defined to have low volatility, conductive, and have high thermal stability.[62-64] In the past, ionic liquids were defined to be nonflammable; however, in 2008 the research time led by Ghanshyam Vaghjiani from Edwards Air Force Base research lab blended hypergolic ionic liquids with bipropellant rocket fuel to increase the oxidizing agent reactivity and lower volatility.[65] Organic salts with relatively low melting points are due to poor crystal packing, charge delocalization, and cation-anion asymmetry.

1.2.2 Brief Account of Ionic Liquid Origin

Paul Walden, a Latvian born research chemist, is credited for reporting the first ionic liquid.[47] Walden purposefully synthesized his ionic liquid, ethyl ammonium nitrate, by an acid-base neutralization technique.[66] An acid-base neutralization involves addition of a Brønsted acid to a Brønsted base in a chilled aqueous solution (Scheme 1.1).[67] He needed a solvent that could be heated with negligible vapor pressure and therefore looked towards the low melting

temperature salt (i.e. 12 °C). These low melting "solvents" would not be presented again until 1948 by Hurley and Wier.[68] In brief, their research consisted of pyridinium halides salts fused electrolytically with metallic chlorides. They concluded that a ~10-75 mole % of fused metallic chlorides (i.e. $AlCl_3$) with pyridinium halides lowered the melting point of the salt below 100 °C, thereby making it a doped ionic liquid (Figure 1.7).

Scheme 1.1. A neutralization method consisting of a Brønsted acid and base was used to synthesize ionic liquids.

$$CH_3CH_2NH_2 + HNO_3 \longrightarrow CH_3CH_2NH_3^+ + {}^-NO_3$$

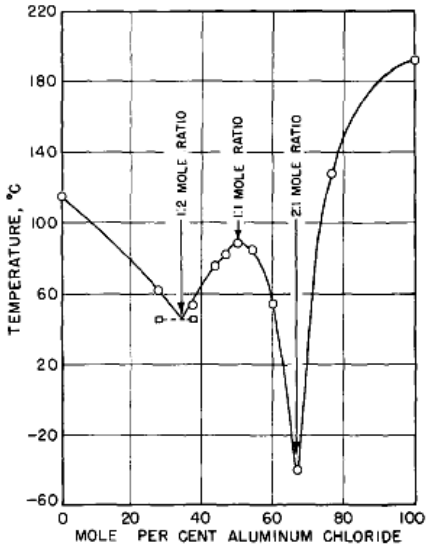
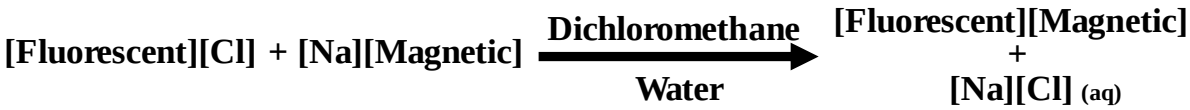


Figure 1.7. Phase diagram of different mole percent ratios of aluminum chloride fused with ethyl pyridinium bromide, $AlCl_3$:[Etpyr][Br], shows a variable melting point trend (1:2 = 45 °C, 1:1 = 88 °C, and 2:1 = -40 °C). Obtained from reference [68].

In 1982 John S. Wilkes introduced the imidazolium ionic liquid as an electrolyte for his electrochemical studies.[52] The imidazolium was a great discovery for ionic liquid research because of inefficient molecular packing resulting in a low melting point. Wilkes performed metathesis reactions (anion exchange) a decade later to the ionic liquid, [1-ethyl-3-methylimidazolium][iodide] with one of the following anions: NO_2, NO_3, BF_4, $MeCO_2$, and $SO_4 \cdot H_2O$.[69] The demonstration of exchanging the metal halide anion resulted in air and moisture

stable ionic liquids without spontaneously forming hydrates.[70] Exchanging counterions is the synthesis used to produce designer ionic liquids for a myriad of applications (Scheme 1.2). This new door of ambient stable ionic liquids gave rise to a multitude of functional uses, research areas, and spectacular findings (Figure 1.8).

Scheme 1.2. A facile metathesis reaction of ionic liquids and like compounds allow for tailor-made materials.



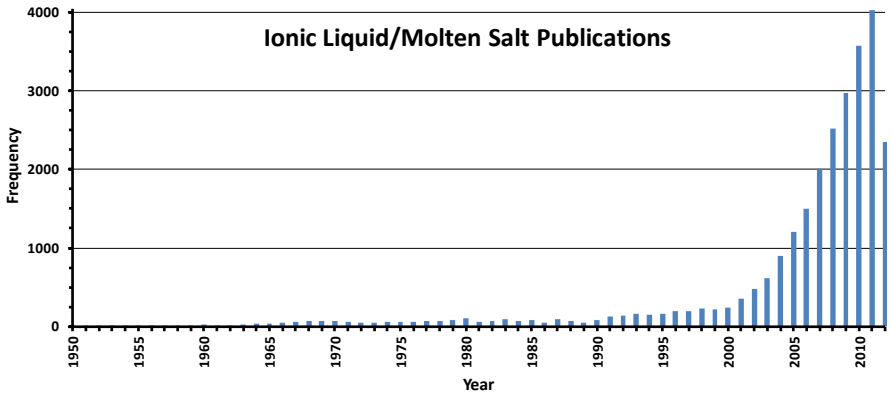


Figure 1.8. Research interest was low for these salts until Wilkes demonstrated metathesis with organic anions in his 1992 article.[b]

1.2.3 Applications of Ionic Liquids

Six years after Wilkes astonished the ionic liquid research community with the metathesis reaction, arguably the first ionic liquid for a practical application was presented.[53] The ionic liquid for practical purposes, or task-specific ionic liquid (TSIL), was [Miconazole][PF_6] an antifungal drug. Although demonstration of the antifungal ionic liquid was never fully realized, task-specific ionic liquids were on the horizon. Presently, ionic liquids are mostly being used for the following properties: separations, electrochemical, negligible volatility solvent, and catalysis.[71-73]

[b] Histogram was derived from article frequency searching the following key phrases in the "Web of Knowledge" database: ionic liquids and molten salts.

1.2.4 Group of Uniform Materials Based on Organic Salts

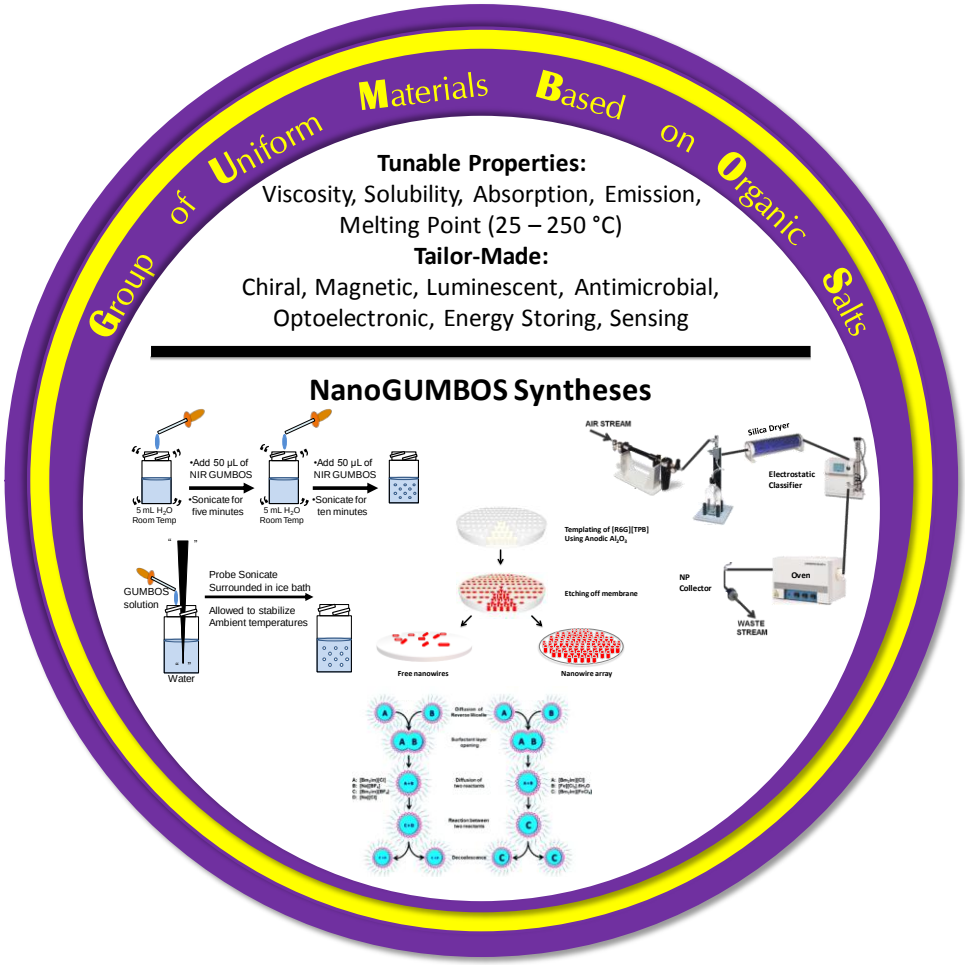
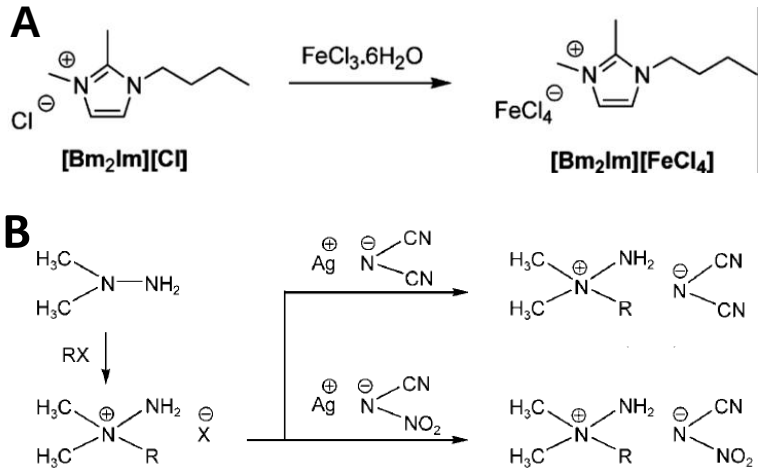


Figure 1.9. Properties and fabrication of GUMBOS and nanoGUMBOS have many opportunities.

A newer classification of molten salts simulating properties of ionic liquids was coined as a ***G***roup of ***U***niform ***M***aterials ***B***ased on ***O***rganic ***S***alts, or GUMBOS. These GUMBOS simulate ionic liquid properties except for functional use in the solid-state phase and the melting point range of 25 – 250 °C. A new term to describe these task-specific molten salts was needed due to the many interesting properties and applicable uses of molten salts in the solid-state phase. In early 2008, Aaron Tesfai under the guidance of Isiah Warner published the first paper concerning this new class of molten salts titled, "Controllable Formation of Ionic Liquid Micro-

and Nanoparticles via a Melt-Emulsion-Quench Approach."[55] Since this novel concept of having organic salts perform work, this research group has demonstrated seven applications for the newly-defined GUMBOS technology[38, 56, 74-78] and eight applications for traditional ionic liquids (Figure 1.9).[55, 79-85]

Scheme 1.3. GUMBOS synthesis using (A) Lewis acid and base method for 1-Butyl-2,3-dimethylimidazolium chloride and (B) S_N2 reaction for quaternization of hypergolic ionic liquids. Obtained from references [56] and [86].



Synthesis of GUMBOS includes the aforementioned methods and the following: combination of a Lewis acid and base, and quaternization. The Lewis acid and base synthesis was used to fabricate magnetic nanoGUMBOS (Scheme 1.3A).[56] The quaternization of an amine was performed by alkylation of tertiary amines to produce ionic liquids (Scheme 1.3B).[86-87]

Task-specific molten salt technology is not new in a sense of concept (*vide supra*),[53] but new life has been restored in the realization of many possibilities. A few of the molten salt applications with combinatorial properties using GUMBOS and TSIL technology are the following: magnetic and chiral,[80] fluorescent and chiral,[81] protic and chiral,[82] and magnetic, luminescent, and tumor-targeting.[85] Herein this dissertation are a few research projects that exemplify these task-specific ionic liquid-like salts.

1.2.4.1 Organic Salts Applications

Organic salts, such as GUMBOS have been demonstrated for purposes other than electrochemical or separations. The nanoGUMBOS consisting of [1,1',3,3,3',3'-Hexamethylindotricarbocyanine] [bis(2-ethylhexyl)sulfosuccinate] administered biocompatible infrared fluorescence characteristics.[74] The nanoGUMBOS ranged in sizes of 71 ± 16 nm easily penetrated within a monkey kidney fibroblast cell after 24 hour incubation. The nanoGUMBOS fluorescence resulted in a blue shift relative to dissolved bulk GUMBOS. A fluorescent microscope was used to image the nanoGUMBOS inside the cells.

Magnetic chiral GUMBOS was another study showing the vast opportunities that these novel compounds can possess.[80] The GUMBOS were derived from chiral amino acid cations and iron (III) chloride anion. Four different amino acid cations were studied to observe the influence onto the magnetic moment and fluorescence of the GUMBOS. The enantiomers had a difference in fluorescence intensity making these compounds viable for asymmetric catalysis and synthesis.

1.3 Rare Earth Metals

1.3.1 Background of Rare Earth Metals

Reihen	Gruppe I. $\frac{}{R^2O}$	Gruppe II. $\frac{}{RO}$	Gruppe III. $\frac{}{R^2O^3}$	Gruppe IV. $\frac{RH^4}{RO^2}$	Gruppe V. $\frac{RH^3}{R^2O^5}$	Gruppe VI. $\frac{RH^2}{RO^3}$	Gruppe VII. $\frac{RH}{R^2O^7}$	Gruppe VIII. $\frac{}{RO^4}$
1	H=1							
2	Li=7	Be=9,4	B=11	C=12	N=14	O=16	F=19	
3	Na=23	Mg=24	Al=27,3	Si=28	P=31	S=32	Cl=35,5	
4	K=39	Ca=40	—=44	Ti=48	V=51	Cr=52	Mn=55	Fe=56, Co=59, Ni=59, Cu=63
5	(Cu=63)	Zn=65	—=68	—=72	As=75	Se=78	Br=80	
6	Rb=85	Sr=87	?Yt=88	Zr=90	Nb=94	Mo=96	—=100	Ru=104, Rh=104, Pd=106, Ag=108
7	(Ag=108)	Cd=112	In=113	Sn=118	Sb=122	Te=125	J=127	
8	Cs=133	Ba=137	?Di=138	?Ce=140	—	—	—	— — — —
9	(—)	—	—	—	—	—	—	
10	—	—	?Er=178	?La=180	Ta=182	W=184	—	Os=195, Ir=197, Pt=198, Au=199
11	(Au=199)	Hg=200	Tl=204	Pb=207	Bi=208	—	—	
12	—	—	—	Th=231	—	U=240	—	— — — —

Figure 1.10. Mendeleev's attempt to of the periodic table shows confusion of where to place the lanthanide elements. Obtained from reference [88].[c]

[c] In regards to rare earths, the listed element Didymium (Di) was later found to be a lanthanide metal complex of both Praseodymium and Neodymium; and atomic symbol for Yttrium has changed from Yt to Y.

Rare earth metals are synonymously called lanthanides due to the first element in the respective row of the periodic table of elements, lanthanum. The lanthanide elements were given a separate row on the periodic table due to confusion of placement. The lanthanides troubled the creator of the table of elements, Dimitri Mendeleev, when he situated the elements according to atomic weight and properties in 1869.[89] In Figure 1.10, question marks next to the known lanthanides can be seen due to his confusion.[88]

Lanthanides are the first of the elements to have f-orbitals (Figure 1.11), experience lanthanide contractions (atomic radii decreases with increasing atomic number), and combined strong magnetic and luminescent behavior. The f-orbitals are smaller than the larger radial closed 5s and 5p orbitals, and thus are strongly shielded. This shielding protects lanthanides from solvation effects which would broaden and/or shift the photophysical spectrum from variable environments.

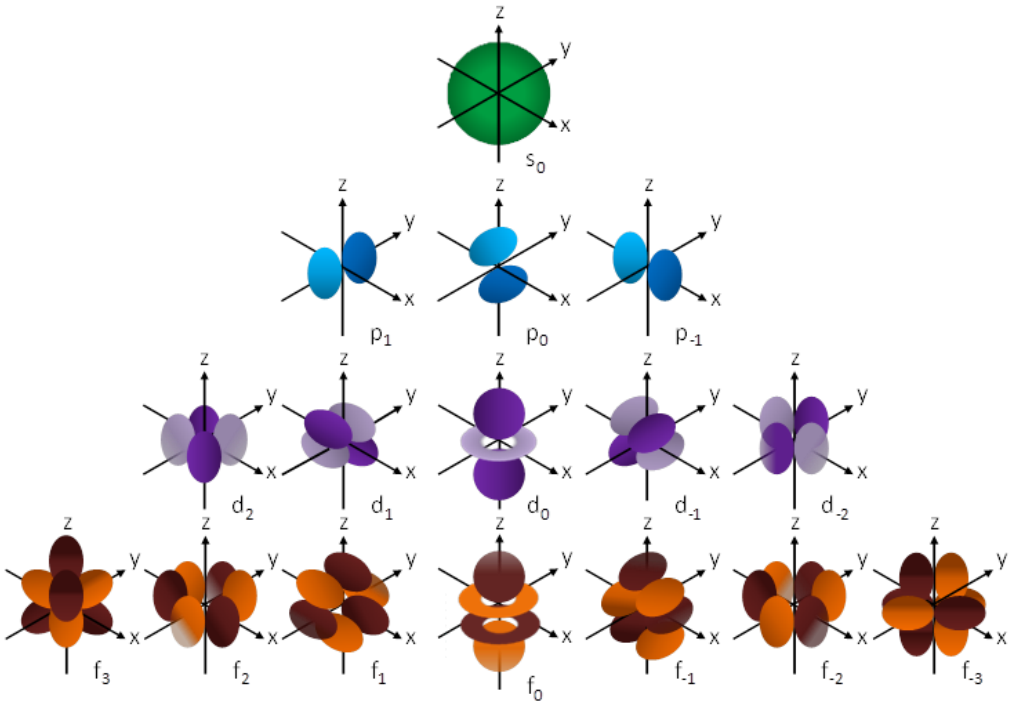


Figure 1.11. The atomic orbitals (s, p, d, and f) in Cartesian coordinates with magnetic quantum numbers, m_l, are listed from largest to smallest.

1.3.2 Luminescence Spectroscopy of Rare Earth Metals

The luminescence of lanthanides has been researched for nearly 90 years since Tomaschek and Deutschbein first studied the spectral lines, phosphorescence properties, and involvement of the f-orbitals in 1924.[90-91] Contribution of the f-orbitals to lanthanide luminescent behavior leads to an increase in quantum yield, long radiative lifetime (phosphorescence), and narrow luminescence intensity. Trivalent lanthanides cannot be directly excited to produce luminescence due to the higher-lying filled 5s and 5p orbitals, and thus rely on excitation transfer to the f-orbitals.[d] The f-orbitals of the lanthanides must be directly excited to employ these properties by ways of Förster resonance energy transfer (FRET) or ligand-to-metal charge transfer (LMCT). This antenna effect (excitation transfers) follows a system of nonradiative pathways to lanthanide energy levels ultimately leading to large red-shift and intense luminescence. The importance of the antenna effect to surpass the spin-forbidden transition was observed 20 years after luminescence from lanthanides were discovered for europium in 1942 by Weismann.[92] The red-shift, as observed by Sir George Gabriel Stokes in 1852, is typical with emission as the excitation energy put into a luminescence compound is greater than the output.[93] In addition, Niels Bohr in communication with Ernest Rutherford produced a *solar system* model of the atom and spectral lines (energy levels) in 1914.[94-96] These conjoined theories led to Aleksander Jabloński's famous diagram to explain electron promotion upon excitation and relaxation emission (Figure 1.12).[97-98] Jabloński introduced the diagram as a simplistic way of explaining phosphorescence of fluoresceine. In his diagram, the energy levels N stood for normal state, M for metastable state, and F for fluorescing state. The actions represented a for

[d] The concept of orbital filling depends heavily on the Aufbau ("building up" of electrons to postulate an atoms outer most orbital shells) and Pauli exclusion (no two electrons of the same spin can occupy the same space) principles.

absorption, b for fluorescence, c for transition to metastable state, d for thermoexcitation, e and f for phosphorescence, and g for slight probability of absorption.

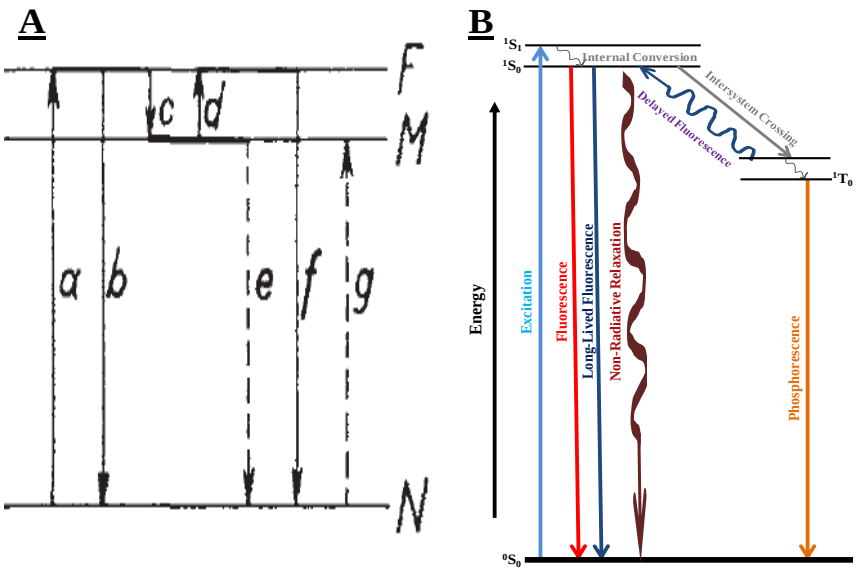


Figure 1.12. Jabloński's (A) original diagram[98] in 1933 and (B) modern diagram ~80 years later both similarly show a visualization for luminescence studies.

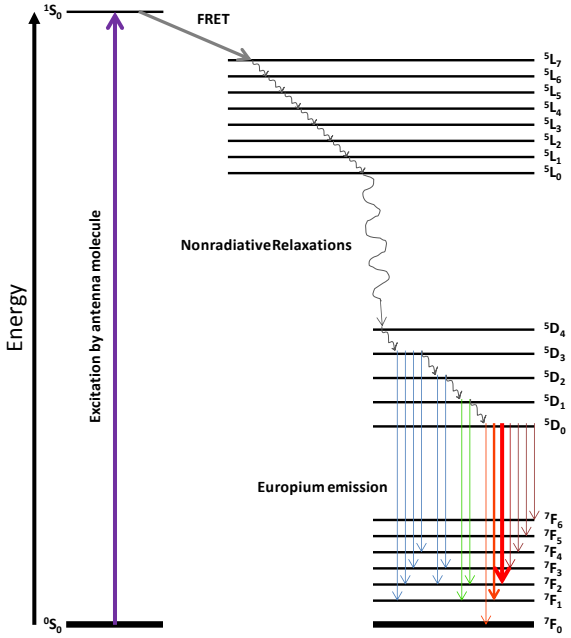


Figure 1.13. A Jabloński diagram is used to represent lanthanide (i.e. europium) emission via antenna effect. (Note: Relaxation energies are not to scale.)

The spectroscopic profiles of lanthanides are unlike most organic fluorophores, in that each energy level for absorbance or luminescence is depicted on the spectrum (Figure 1.13).

Unlike organic or transition metal absorbance spectra, lanthanides appear as atomic spectra as the multiple 4f-4f energy level transitions are visible (Figure 1.14).[99] In addition to the spectral lines being visible, the higher-lying 5s and 5p orbitals protect from solvent luminescent quenchers. Luminescent quenchers ultimately reduce the emission quantum yield of a fluorophore. Static quenchers can affect luminescence by inhibiting excitation energy, or altering the absorbance spectrum by complexing with the luminescent molecule. The following are examples of dynamic quenchers (and cause): collisional (solvent or paramagnetic/dissolved oxygen), heavy atom effect (halogens and other electron scavengers; protons, NO_3^-, Cu^{2+}, Pb^{2+}, Cd^{2+}, and Mn^{2+}), excimers (unstable dimers changing excitation/emission spectrum), and FRET. Otto Stern and Max Volmer devised an equation to describe luminescent quenching in 1919:[100]

$$\frac{F_0}{F} = 1 + K_{SV} \qquad \text{Equation 1.2}$$

The pair established, K_{SV} as the Stern-Volmer quenching constant equaling to the product of the bimolecular quenching constant, k_q, and lifetime of the fluorophore without quencher, τ_0. Fluorescence intensities with and without quencher were respectively assigned as F and F_0.

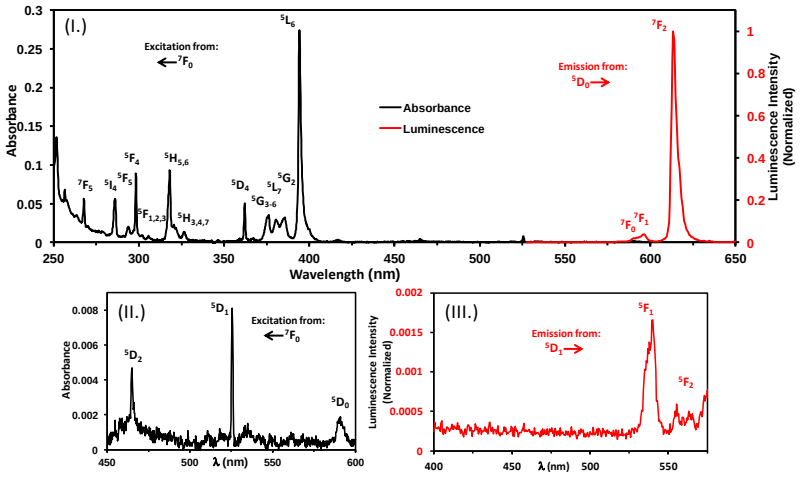


Figure 1.14. Photophysical spectra of europium (Eu^{3+}) reveals energy level term symbols for absorbance and luminescence. (I.) Spectra of aqueous 0.100 M $EuCl_3$ for absorbance and 0.8 µM Eu(thenoyltrifluoroacetone)$_3 \cdot 2H_2O$ in acetonitrile for luminescence. (II.) and (III.) are enlarged regions of spectra for absorbance and luminescence, respectively.

A set of rules were devised in the 1925 by Friedrich Hund for ground state energy level (quantum) transitions to be written.[101] These three consecutive set of rules that rightfully came to be known as Hund's rule are as follows:

(1) the ground state term has the largest spin multiplicity,

(2) largest orbital multiplicity,

(3) if number of electrons, $n < 2(M_L)+1$ then $J = J_{min}$, but if $n > 2(M_L)+1$ then $J=J_{max}$.

The electronic configuration for the lanthanides is written with term symbols, $^{2S+1}\Gamma_J$, that derive from M_L and M_S quantum numbers.[102] The total orbital and spin quantum numbers, M_L and M_S, are the respective sums of m_l *and* m_s. The term symbols designate M_L and M_S as angular momentum Γ (orbital) and S (spin) quantum numbers, respectively. The orbital angular momentum quantum number, Γ, is appointed by the following quantum letters: S, P, D, F, G, … (alphabetically excluding J thereafter) corresponding to M_L (0, 1, 2, 3, 4, …). The spin angular momentum quantum number, S, is the product of the number of electrons in the outermost subshell and ½ electron spin. The product of spin multiplicity, 2S+1, and orbital multiplicity, $2M_L+1$, is the number of possible microstates (or atomic states). The total angular momentum quantum number, J, is the sum of the orbital angular and spin angular momentum quantum numbers. From these calculations the ground state terms for trivalent lanthanides can be determined (Table 1.2).

Table 1.2. Ground state term symbols for trivalent lanthanides according to Hund's rule.

Lanthanide Atomic Symbol		f^n		Ground State Term	
La	Lu	f^0	f^{14}	$^1S_0$	$^1S_0$
Ce	Yb	f^1	f^{13}	$^2F_{5/2}$	$^2F_{7/2}$
Pr	Tm	f^2	f^{12}	$^3H_4$	$^3H_6$
Nd	Er	f^3	f^{11}	$^4I_{9/2}$	$^4I_{15/2}$
Pm	Ho	f^4	f^{10}	$^5I_4$	$^5I_8$
Sm	Dy	f^5	f^9	$^6H_{5/2}$	$^6H_{15/2}$
Eu	Tb	f^6	f^8	$^7F_0$	$^7F_6$
Gd		f^7		$^8S_{7/2}$	

1.3.3 Instruments for Spectroscopy

1.3.3.1 Absorption Spectrometry

Molecular absorbance can be measured by an ultraviolet-visible-near-infrared (UV-Vis-NIR) absorbance instrument (Figure 1.15). The absorbance instrument uses a light source (e.g. xenon arc, tungsten filament, and deuterium lamps) to promote a sample's electron from the highest occupied molecular orbital (HOMO) to the lowest unoccupied molecular orbital (LUMO). Electron promotion to a molecular orbital is typically referred to as excitation from the singlet ground state (S_0) to the first excited singlet state (S_1) and occurs at a rate of picoseconds to femtoseconds.

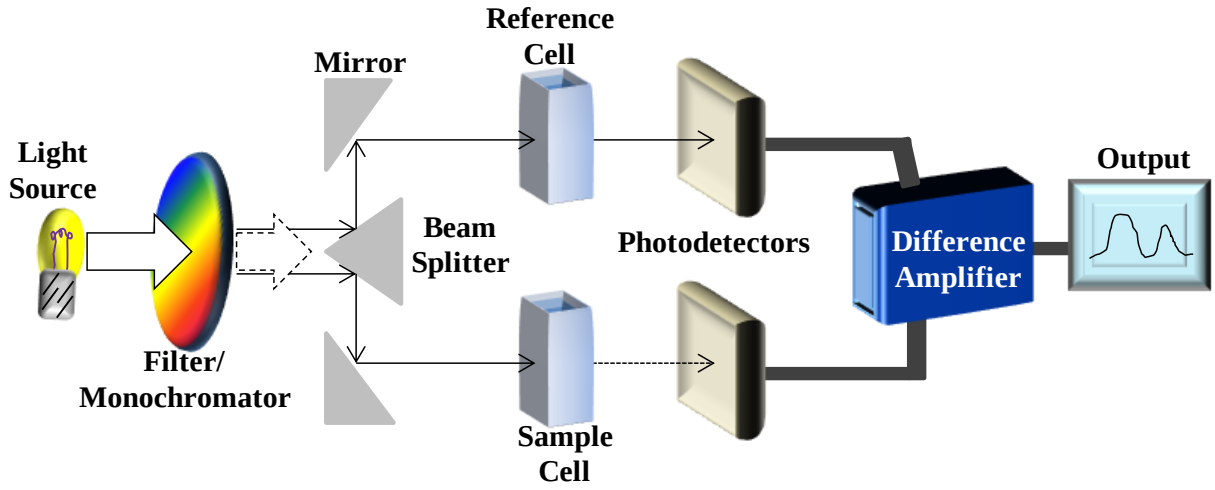


Figure 1.15. A typical double-beam absorbance instrument was used to measure the absorbance of the solute in solvents.

The absorbance instrument measures the electronic transitions by filtering selected wavelengths from the light source by a monochromator. The light is then split into two by mirrors to have one-half of the beam measure absorbance from the reference cell, and the other half measuring the sample. The two results are detected by transducers (e.g. photomultiplier tube or photodiode) and compared by a difference amplifier measuring the solute absorbance with respect to the solvent. The spectrum is then displayed onto an output device (e.g. computer or

light-emitting diode (LED) display). A mathematical representation of absorbance spectroscopy is expressed through the Beer-Lambert Law.

$$A = -\log(T) = log\frac{I_0}{I} = \varepsilon bc \qquad \text{Equation 1.3}$$

The Beer-Lambert Law indicates that absorbance (A) is inversely proportional to the log of transmittance (T). Since absorbance is the amount of light that is used to promote a solution to an excited state, intuitively transmittance is the amount of light that traverses through a solution. To measure the amount of light taken up by solution Lambert's law states that the log ratio of incident light from the source (I_0) is compared to the incident light that passed through the solution (I). Lastly, the more common usage of Beer's Law is the product of molar absorptivity (ε), cell path length (b), and sample concentration (c). Beer's Law can be used to quantitatively acquire an unknown concentration after performing a series of known concentrations resulting in a plotted calibration curve (y=mx+b). The slope (m) of the curve would equate to molar absorptivity (ε).

1.3.3.2 Photophysical Spectrometry

Luminescence is the radiative relaxation, called emission, of an electron from an excited state to ground state. In order for the luminescence to occur for organic molecules, the molecule must contain an aromatic compound that is conjugated (e.g. anthracene) or attached to a conjugated double bond (e.g. cyclanone). The radiative transitions can labeled as "spin-allowed" when the electron spin multiplicity is not changed during excitation or emission, such as singlet to singlet ($S_0 \rightarrow S_n$ or $S_1 \rightarrow S_0$, respectively). A radiative transition called, "spin-forbidden" is when the spin multiplicity is changed during excitation or emission. Spin-forbidden transitions during excitation usually result in a weak molar absorptivity; however, during emission these transitions take relatively longer to reach ground state than spin-allowed transitions. Emission

from a spin-allowed transition is referred to as fluorescence and can have radiative lifetimes ranging from microseconds to nanoseconds. Contrastingly, spin-forbidden transitions are referred to as phosphorescence and can have long radiative lifetimes ranging from milliseconds to seconds. Long-lived or delayed fluorescence is similar to phosphorescence having long radiative lifetimes, but the radiative relaxation occurs from the excited singlet state opposed to excited triplet state as depicted in a Jabloński diagram (figure 1.12B).

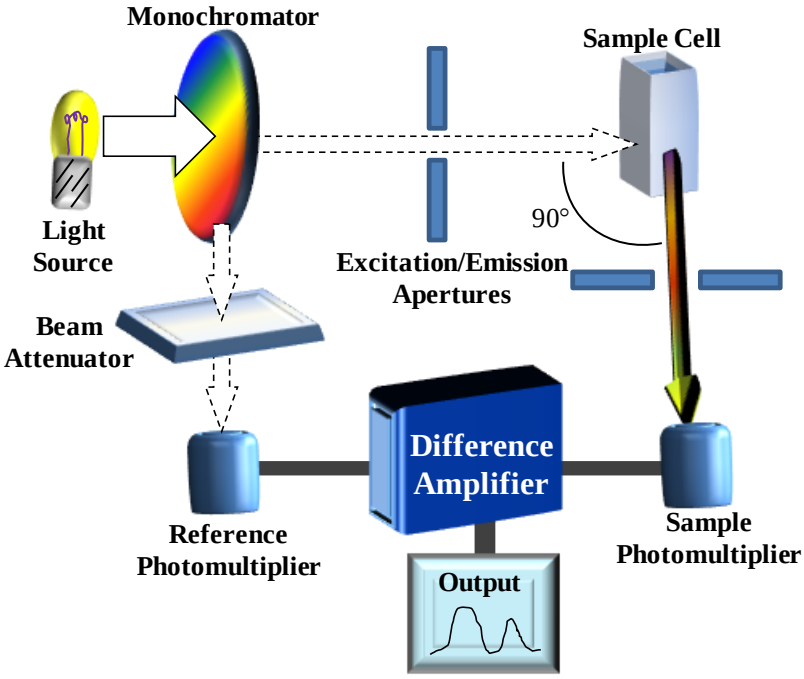


Figure 1.16. Spectrofluorometer instrument is used to measure the luminescence intensity from a sample.

Luminescence spectra are acquired by a light source (e.g. xenon arc lamp or Nd:YAG laser) shining through a monochromator (wavelength selector) exciting the sample (Figure 1.16). The excitation wavelength typically is the absorbance wavelength maximum. The excitation wavelength is then measured as a reference of light intensity and later compared to the samples emission intensity. The excitation light towards the sample passes through apertures (or slits) to control excitation light intensity. The apertures are adjusted (1 – 10 nm) depending on whether

the sample requires more light due to being too diluted, or less light due to being over concentrated. The sample cell is excited orthogonally from the detector to avoid light source saturation. The resulting emission passes through another aperture that controls the intensity to the photomultiplier tube. The emission spectrum with respect to the reference is displayed onto an output device.

Emission from a sample is usually incapable of achieving a 100% quantum emission yield due several factors. The factors disallowing a 100% quantum yield would include photobleaching, collisional quenching, heavy-atom effects, dynamic quenching, and radiationless processes. The radiationless processes encompass internal conversion ($S_1 \rightarrow S_0$ + heat, or $T_1 \rightarrow S_0$ + heat) and intersystem crossing ($S_1 \rightarrow T_1$ + heat). In the succeeding sections (1.4) the heat produced from inefficient luminescence is important towards photothermal generation for cancer destruction.

1.3.4 Applicable Uses of Rare Earth Metals

Since the understanding of lanthanide properties there have been many practical uses for medical and commercial purposes. The earliest use for a trivalent lanthanide, europium, was in cathode-ray tube television (CRT) screens.[103] By using the intense luminescent behavior of europium, television manufacturers were able to make the image more vibrant. These luminescent properties are currently be studied by various academic, government, and independent research facilities mainly to work as biomarkers.[104] Various rare earth metal complexes are currently in use for cancer patients under the drug brand names (lanthanide): Antrin (lutetium), Optrin (lutetium), and Omniscan (gadolinium).[105] The drugs listed are for the following purposes, respectively: removal of plaque in the artery, macular degeneration, and as a magnetic resonance imaging (MRI) contrast agent.[106] Lutin is a drug that employs lutetium for

cancer therapy by creating singlet oxygen ($^1O_2$) from photodynamic irradiation at 732 nm. Singlet oxygen species are generated during relaxation of triplet state after excitation of a molecule.[107] Oxygen is an excellent photo quencher; therefore, the molecules excited relaxation energy is transferred to neighboring molecular oxygen creating singlet oxygen. This form of oxygen has been found to be cytotoxic as it is an intermediate in the oxidation of biomolecules (e.g. DNA, proteins, and lipids).[108-109]

1.3.5 Rare Earth Metals and Ionic Liquids

Lanthanides have been easily dissolved into ionic liquids which can be attributed to the ether or hydroxyl functional groups on the alkyl chain on a cation.[110] However, lanthanide compounds as an ionic liquid become immiscible in water at room temperature. Trivalent lanthanide beta-diketone complexes dissolved in ionic liquids (i.e. [1-hexyl-3-methylimidazolium] [bis(trifluoromethylsulfonyl)imide], were found to have higher quantum yield and more photostability than if dissolved in an organic solvents (i.e. acetonitrile).[111-112]

Ionic liquids have been used as a solvent for the separation of lanthanide ions by a liquid-liquid phase extraction method.[113-115] Hydrophobic ionic liquids were used to separate lanthanides (i.e. europium, neodymium, and lanthanum) from aqueous solutions. The process was performed by adding the mixture of [1-alkyl-2-methylimidazolium][bis((trifluoromethyl)sulfonyl)imide] ($[C_n mim][Tf_2N]$) and 2-thenoyltrifluoroacetone (tta) to the trivalent lanthanide hydrated complexes ($Ln(H_2O)_n^{3+}$). The water molecules were removed from the inner coordination sphere due to the presence of the imidazolium cation and anionic exchange pathway from the ionic liquid (Scheme 1.4).

Scheme 1.4. Liquid-liquid extraction using an ionic liquid and β-diketone were used to separate a lanthanide from a hydrate complex.[113]

$$Ln(H_2O)_n^{3+} + 4Htta + [C_n mim][Tf_2N] \leftrightarrow [C_n mim][Ln(tta)_4] + 4H^+ + Tf_2N^- + nH_2O$$

Ionic liquids within a silica network of ionogels have been doped with a trivalent lanthanide β-diketone complex resulting in the gel emitting luminescence upon ultraviolet irradiation.[116] Ionogels consisting of a porous silica matrix and ionic liquid residing in the pores did not affect the luminescence intensity.

Ionic liquids have also been used as the priority solvent in a microwave nanoparticle synthesis. Lanthanide complexes dissolved in the ionic liquid were subjected to five minutes of microwave irradiation (*ibid.*) resulting in a lanthanide nanoparticle diameter of 15 nm.

1.4 Hyperthermia as a Therapeutic

1.4.1 Hyperthermal Therapeutics in Antiquity

Over the millennia, dating back to Greek antiquity mankind has used barbaric forms of photodynamic therapy by ways of heat production[117] and light[107] to cure their ailments. Early civilizations would use heat via hot pokers to cauterize surface tumors or induced fevers to reduce ailments.[117-118] In 500 BC, Parmenides introduced the idea of using fevers to cure saying, "Give me the power to produce a fever and I'll cure all diseases."[119] Over a century (370 BC) later Hippocrates popularized the medical therapeutic using internal and external heat to treat diseases saying, "diseases that medicines do not cure are cured by the knife. Those the knife does not cure are cured by fire. Those that fire does not cure, must be considered incurable."[117] This use of fire led to more 'sophisticated' forms of hyperthermal methods using selective pokers (Figure 1.17).[118] Hyperthermal methods were primarily performed by externally heating up a device to interact with the location of interest. This approach was not limited to heating up metal pokers, but also in the 1800-1900s electrically heated cautery probes were used. John Byrne devised an effective method on reducing tumors (i.e. uterine) with little chance of recurrence by creating a set of electrocautery tools.[120]

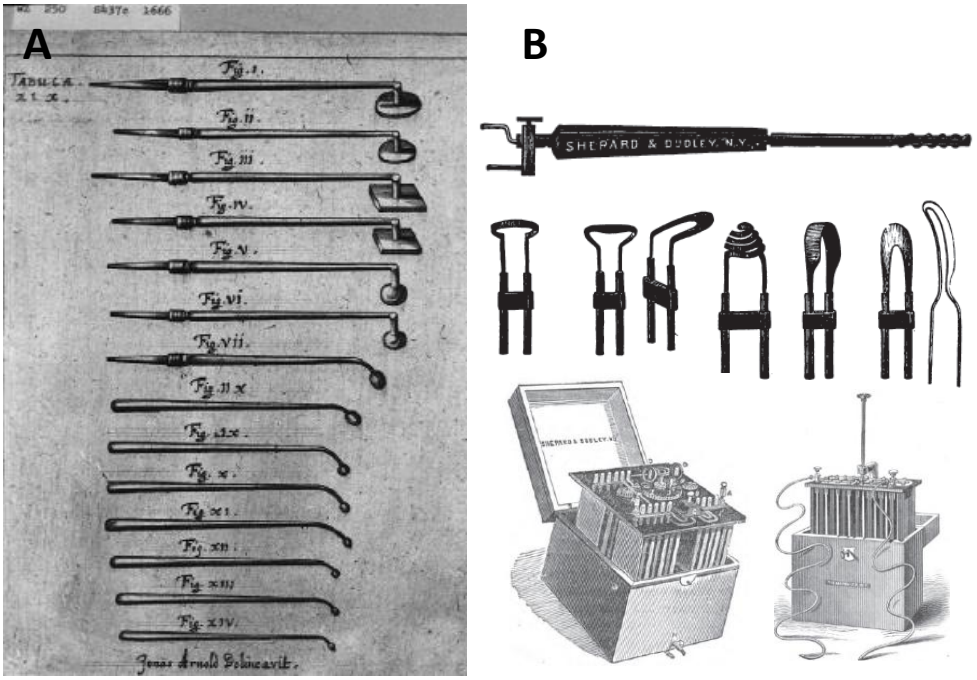


Figure 1.17. The harsh methods of hyperthermal treatment by use of (A) pokers and (B) electrocautery treatments were primarily used 400 BC – 1800 AD and 1800-1900 AD, respectively. (Obtained from references [118] and [120], respectively.)

1.4.2 Induced Fever as a Cancer Hyperthermal Therapeutic

A fever is part of the systemic inflammatory response when the body creates a hostile environment for bacteria. The hostile environment includes an increase in white blood cells, increased heart rate, and a raise in core body temperature.[121] Fevers can also be caused by the protein interleukin-1 in pyrogens.[122] This type of therapeutic was observed in Hippocrates time,[123] but seemed largely ignored by physicians until 1866.[124] A German physician, Wilhelm Busch, was routinely checking on a patient that had a facial tumor and abruptly contracted an erysipelas (Streptococcus) infection. A symptom of erysipelas is a raise in body temperature due to the fever. The patient's fever was very high and carried on for several days resulting in a decrease in the tumor mass.[124] This medical record since then provided patients with an alternative method to cauterization for the removal of tumors and cure from other ailments (e.g. small pox, malaria, and typhoid) by having self-induced fevers.[125] These slight rises in body

temperature were sufficient to destroy tumor cells as supported by Byrne in 1889. Byrne determined that malignant cells would die at temperatures greater than 42°C.[126] In the 20th century great progress towards alternative hyperthermal therapeutic methods were researched. Chemists began to formulate drugs that would cause the body to create fever-like symptoms without jeopardizing the patients overall health with injecting strains of bacteria.[127] In 1933 a chemical compound originally designed for weight-loss, DNP (or 2,4-dinitrophenol) was able to raise the body temperature by increasing the metabolic rate.[128-129] An increase in metabolic rate was due to DNP easily penetrating through the cellular lipid bilayers as a protonophore and reducing efficiency of the chemical energy, ATP (adenosine triphosphate).[130-132]

1.4.3 Early Hyperthermal Therapeutics

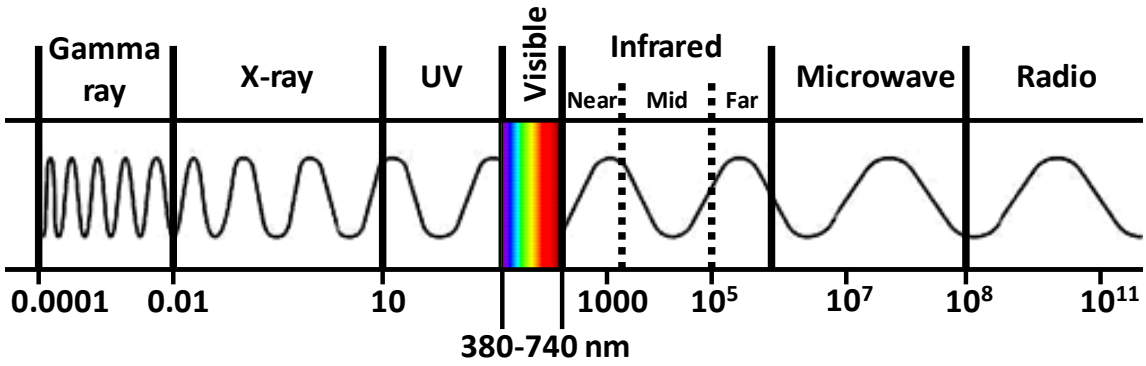


Figure 1.18. Wavelengths (in nanometers) become longer and lesser energetic from left-to-right in the electromagnetic spectrum. (Note: Not to scale.)

Light radiation therapy uses heat generated from emission energy; unfortunately, the exposure of higher energy wavelengths can lead to more serious side effects. Throughout the 1940s – 1980s various light radiation therapies in concert with other drugs were being tested using different radiative sources (i.e. gamma rays from radon or cobalt-60). More presently, in the beginning of the 21st century a more selective hyperthermal (or "radiothermal") therapeutic device was put into the medical practice by introducing the trademarked name, Cyberknife.[133-134]

The Cyberknife system has operated to emit 45-70 Gy[e] of X-ray irradiation to selectively treat malignant tumors.[135-136] Research for irradiation therapy has shifted to the near-infrared spectrum with the invention of the laser (*vide infra*) (Figure 1.18).

1.4.4 Infrared Spectrum

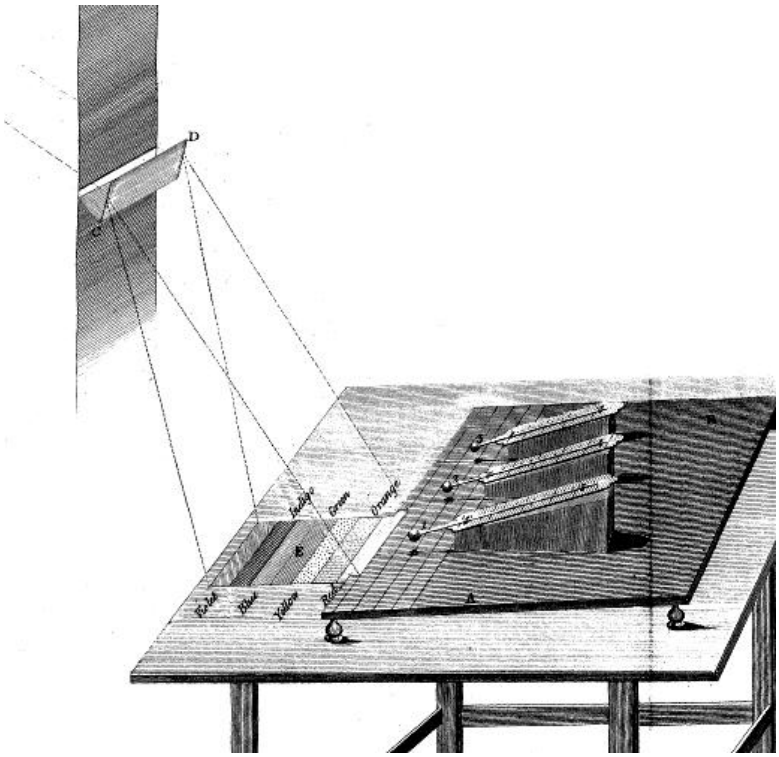


Figure 1.19. The apparatus used by Herschel in 1800 was designed to measure radiant heat from refrangible invisible rays immediately beyond the prismatic spectrum. (A) and (B) are the stands used to hold the three thermometers, (C) and (D) are the prism, and (E) is the visible spectrum. Obtained from reference [137].

Academic research has been making strong grounds using lesser energetic and tissue absorbent wavelengths to treat malignant tumors.[138-139] The wavelength of use is attributed to Sir Frederick William Herschel, and his notable discovery of infrared light and observation of radiant heat ($\lambda \approx 740$ nm – 1 mm).[137] Herschel discovered infrared light by obtaining a chromatic spectrum from prisms produced by the sun and placing thermometers next to both "vanishing

[e] A Gray (Gy) is the SI (*Système International d'unités*) unit of absorbed radiation energy from gamma ray or X-ray. 1 Gy = 1 J · kg^{-1}

rays," violet and red (Figure 1.19). The radiant heat absorbed by the refracted invisible violet and red rays respectively resulted in 0.5-1 °C and 8-9 °C temperature increases. Herschel proposed calling these invisible rays that were "not fit for vision [yet] still exerting increasing energy," the thermometrical spectrum.

1.4.5 Light Amplification by Stimulated Emission Radiation

1.4.5.1 Brief Background on LASER Origins

Research has dramatically progressed since the observation of radiant heat from the "thermometrical spectral" infrared wavelength. Combining the previous statements on eradicating tumors conclude the necessity for artificially-produced infrared light emission of scientific purposes. The theoretical notion for light amplification by stimulated emission was from Albert Einstein's 1917 article, *Zur Quantentheorie der Strahlung* (On the Quantum Theory of Radiation).[140] Einstein's paper along with other subsequent physicists (Ladenburg,[141] Fabrikant,[142] Lamb and Retherford,[143] and Kastler[144]) formulated the necessary ground work towards Charles H. Townes development of such an instrument (Figure 1.20).[145]

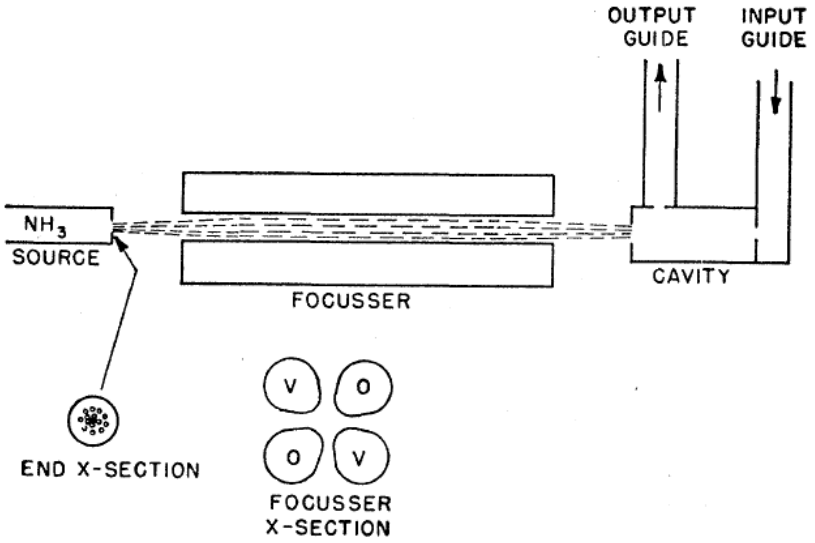


Figure 1.20. Schematic of Townes' microwave amplification by stimulated emission radiation instrument was originally developed to be a high-resolution microwave spectrometer. Obtained from reference [145].

1.4.5.2 LASER Components

In 1954 the principal investigator, Townes, developed the first device to amplify stimulated emission of microwave radiation. The microwave amplification by stimulated emission radiation (MASER) is comprised of three components to maintain high frequency emissions: gain medium, pump source, and focusing resonant cavity.[146-147] Similarly to MASERs, light amplification by stimulated emission radiation instruments (LASER or laser) has employed solid-state materials, liquid solutions, or gas mixtures as a gain medium since its inception in 1960.[148] Gain media are used excite the electronic energy levels and feasibility to stimulate a population inversion within the pumping source. Population inversion is when probability of molecules to be in excited state is greater than ground state. Stimulated emission of radiation is amplified by a series of cavity mirrors within the gain medium. In the focusing cavity component, all but one of the mirrors (i.e. resonant mirror) is 100% reflective allowing for release of high-intensity radiation output. Gain media that lasers have used to generating high-intensity radiation have ranged from noble and inert gases, transition metal vapors, transition metal complexes, and lanthanide-doped metal complexes (Table 1.3).

Table 1.3. Variable gain media towards the production of high-intensity output results in different wavelengths of radiation emission. Adapted from reference [146].

Type	Gain Medium	Wavelength (nm)
Gas	He(g), Ne(g)	3391, 1151, 632, 544
Gas	N_2 (g)	337
Gas	Ar^+(g)	488, 515
Gas	K^+(g)	647
Gas	CO_2(g)	10,000
Gas	Cu(g)	510
Gas	He(g), Cd(g)	441, 325
Solid-State	Cr^{3+}:Al_2O_3	694
Solid-State	Nd^{3+}:$Y_3Al_5O_{15}$	1064
Solid-State	Nd^{3+}:$Y_3Li_xF_y$	1054
Solid-State	Ti^{3+}:Al_2O_3	780

1.4.6 Laser Hyperthermal Cancer Therapeutics Techniques

1.4.6.1 Laser Photothermal Origins

Presently, hyperthermal techniques to destroy cancerous tumors use nanomaterials activated by a near-infrared $Nd^{3+}:Y_3Al_5O_{15}$ (Nd:YAG) laser. These studies employ nanomaterials to absorb the near-infrared (NIR) lasing wavelength to result in thermal emissions. John F. Ready and T. J. Harris determined photothermal effects from laser irradiation absorption in 1963.[149-151] The material (i.e. Al, Fe, Cu, W, and Pt) used to absorb the laser emissions had an immediate rise (i.e. 1 ns) in temperature that resulted in vaporization. The metals under laser power density of 5 $TW \cdot cm^{-2}$ at 10 ns pulses (0.2 mm diameter focal spot) experienced temperature increases of 500 °C before an observed "plume of vaporized material."[151] Since then hyperthermal therapeutics has increasingly become a popular approach on treating cancerous tumors opposed to cautery or induced-fever techniques (Figure 1.21).

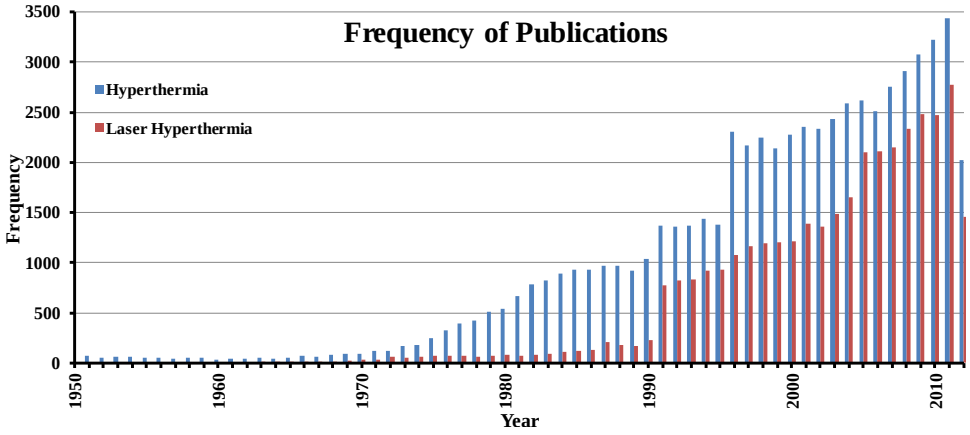


Figure 1.21. Hyperthermal therapeutics became more popular since the invention of the MASER in 1954.[f]

A team of physicians led by Paul McGuff used a solid-state ruby ($Cr^{3+}:Al_2O_3$) laser to destroy 20 different types of cancer cells in 1964.[152] Unlike Ready and Harris, McGuff used

[f] Histogram was derived from article frequency searching the following key phrases in the "Web of Knowledge" database: Hyperthermia (hypertherm- and phototherm-), and Laser Hyperthermia (hypertherm- or phototherm-, and laser or maser).

relatively lower power density of 4 MW·cm^{-2} at 3 ms pulses to eradicate the malignant tumors. The cancerous tumors were destroyed with a lasing focal spot diameter of 2 mm ultimately resulting in a temperature increase (distance from lasing area): 380 °C (2 mm), 94 °C (5 mm), and 46 °C (10 mm). Cancer cells are more prone to heat due to poorer vascularization than healthy cells.[153] This method proved to be successful and less invasive than previous hyperthermal therapeutics such as gamma irradiation and cautery techniques.[152, 154-158] Although there seemed to be excitement for hyperthermal cancer therapeutics, research efforts using laser technology only progressed 35 years after McGuff's publication.

1.4.6.2 Near-Infrared Transparency of Human Tissue

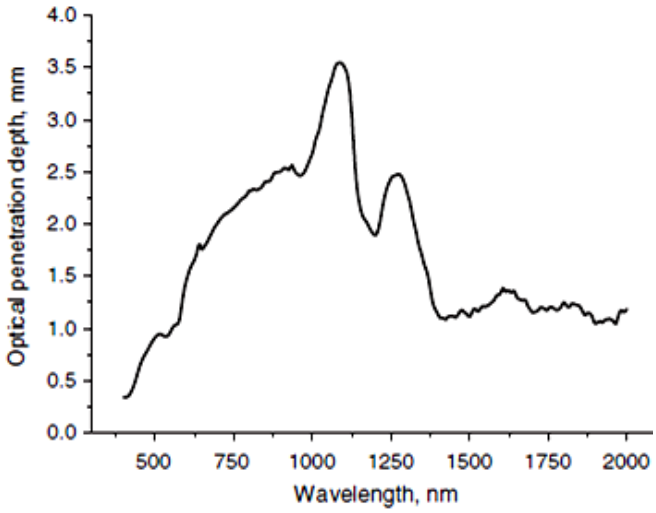


Figure 1.22. The optical penetration depth (mm) of human skin is highest in the near infrared region. Obtained from reference [138].

From 1964 to 1999 there were about 600 publications on hyperthermal techniques towards cancer therapy, but that number has more than doubled since the millennia with 1,400 publications. Most of these publications use lasers that emit infrared irradiation for the purpose of reaching a malignant tumor percutaneously. Human tissue (i.e. skin) weakly absorbs infrared wavelengths allowing infrared laser irradiation to penetrate without a prior incision or resection

(Figure 1.22).[138] Therefore, infrared irradiation has been absorbed by various nanomaterials towards a hyperthermal cancer therapeutic.

1.4.7 Nanomaterials Used as a Hyperthermal Therapeutic

Nanomaterials (e.g. particles, rods, shells, etc.) that have been researched to produce hyperthermia upon near-infrared laser irradiation include the following: Au,[139] CuS,[159] carbon nanotubes,[160] and porphysomes.[161] The hyperthermal nanomaterials use surface plasmon resonance (*sans* carbon nanotubes) and absorbance to generate thermal effects. Variable infrared laser irradiation wavelengths were used (e.g. 660, 760, 820, 980, and 1064 nm) based upon the nanomaterials absorbance maxima. These materials have generated above the 42 °C threshold for hyperthermia.[153, 162] The hyperthermal effects (e.g. cellular apoptosis or necrosis) using nanomaterials were demonstrated with *in vitro* and *in vivo* models (Figure 1.23). Cellular apoptosis death is when a cell is triggered to complete a final metabolic process before dying, while necrosis is immediate death.

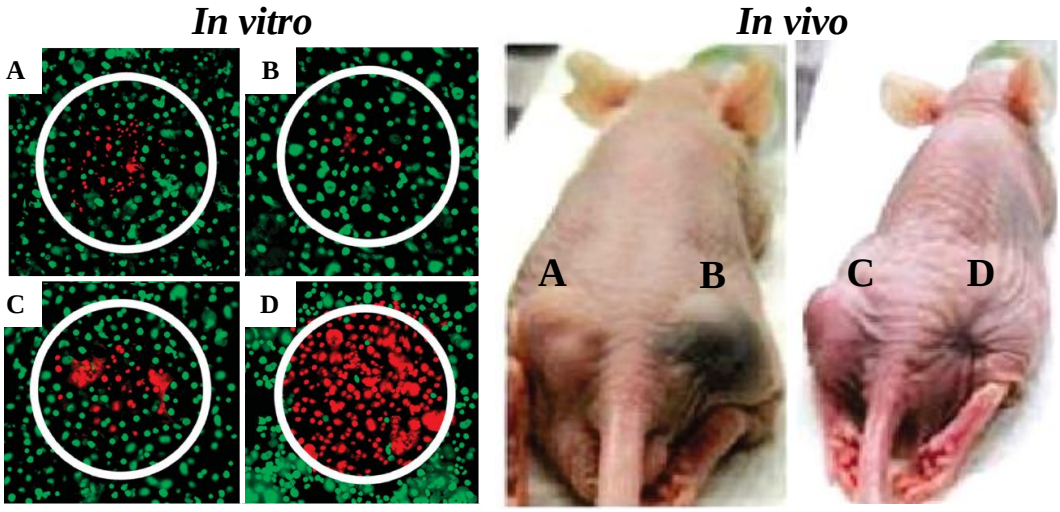


Figure 1.23. Nanomaterials studied *in vitro*[163] and *in vivo*[160] were used in concert with infrared laser irradiation hyperthermia as a cancer therapeutic. (A) Nanomaterial control, (B) saline control, (C) laser control, and (D) nanomaterials and laser. Obtained from references [163] and [160] respectively.

1.4.7.1 Hyperthermal Cancer Therapeutic Using Gold Nanomaterials

Gold nanomaterials for the purpose of hyperthermal cancer research have existed in many shapes such as particles (spheres), rods, and shells. Regardless of the shape, the gold nanomaterials tend to have to have an absorbance maximum around 820 nm.[139] A NIR laser at 820 nm is used for optimal photothermal heating since that is the absorbance maximum. Gold nanomaterials (150 – 300 μg mL^{-1}) were capable of generating an increase of 40 – 60 °C heat upon laser irradiation. The generated heat was proven successful in the destruction of cancerous cells as depicted in figure 1.21.

1.4.7.2 Hyperthermal Cancer Therapeutic Using Carbon Nanotubes

Carbon nanotubes (~400 nm) were also capable of achieving a laser generated heat increase of 40 – 60 °C at concentrations 5 – 30 μg mL^{-1}.[25, 160] The laser wavelength used for carbon nanotubes was at 980 or 1064 nm. The carbon nanotubes were synthesized to become more biocompatible such as encasing (held by π-π stacking) with DNA, or conjugating folate to the carboxylic sites.

1.4.8 Magnetic Hyperthermal Method

Magnetic hyperthermia is cancer therapeutic that does not use NIR laser to produce heat, but instead by a magnetic field. Magnetic hyperthermia functions by the alternating magnetic field (230 kHz) on the compound. The magnetic moment of a compound is proportional to the amount heat generated.[164] Nanoparticles that have demonstrated magnetic hyperthermia are iron-based (e.g. iron oxides and iron cobalt). The magnetic nanoparticles were capable of producing 20 – 35 °C heat using 10 mg mL^{-1}.[165] Cancer cells under the influence of magnetic nanoparticles and an alternating field were 70% destroyed.

1.5 Scope of Dissertation

The objective of the research was to study the spectroscopic properties of nanoGUMBOS using a lanthanide (i.e. europium) or near infrared dyes (i.e. 1048 and 1061). Herein this dissertation a comparative discussion on the bulk and nanoparticle luminescence of lanthanide-based nanoGUMBOS is detailed. In addition, an alternate hyperthermal technique using nanomaterials based on GUMBOS will be discussed. The nanoGUMBOS will use an infrared cationic dye and biocompatible anions to be used as a cancer therapeutic.

In Chapter 2, lanthanide-based nanoGUMBOS were produced by an aerosol method resulting in particle sizes of 39.5 ± 8.4 nm. An intense luminescence peak at 613 nm from europium (III) was prevalent when bulk lanthanide-GUMBOS, $[C_6mim][Eu(tta)_4]$, was dissolved in ethanol. Contrastingly, luminescence from the lanthanide nanoGUMBOS was less intense at 613 nm and fluorescence from the imidazolium cation was prominent at 420 nm. It is concluded that the cation surrounds the anion negatively affecting europium luminescence intensity.

In Chapter 3, NIR nanoGUMBOS were synthesized in various pH media (2, 5, 7, 9, and 11) by a reprecipitation method using an ultrasonic probe sonicator. The nanoGUMBOS varied in sizes, aggregation, and structural makeup due to the different pH. A photothermal study of the NIR nanoGUMBOS was conducted. The aqueous suspended NIR nanoGUMBOS released a thermal energy increase of 13 – 23 °C when irradiated for five minutes by a 1064 nm NIR ($Nd:YVO_4$) laser. Photothermal efficiency was calculated to range from 13 – 64% and inversely correlated with the band gap energies from the NIR nanoGUMBOS, [1048][Ascorbate], [1061][Ascorbate], [1048][Deoxycholate], and [1061][Deoxycholate].

In Chapter 4, NIR nanoGUMBOS synthesized from a microwave-assisted reprecipitation method was used for a hyperthermal therapeutic on MDA-MB-231 breast cancer cells. The NIR

nanoGUMBOS employ a [Folate] anion for targeting the overexpressed folate-receptor alpha proteins that jacket cancer cells. The NIR nanoGUMBOS, [1048][Folate] and [1061][Folate], had limited cytotoxicity *sans* 1064 nm NIR ($Nd:YVO_4$) laser irradiation. However, the photothermal energy emitted by the NIR nanoGUMBOS during irradiation in cell media increased 25 – 35 °C. The NIR irradiation and NIR nanoGUMBOS in concert successfully destroyed breast cancer cells after 20 minutes of continuous irradiation.

1.6 References

1. Daniel, M. C.; Astruc, D. Gold Nanoparticles: Assembly, Supramolecular Chemistry, Quantum-Size-Related Properties, and Applications Toward Biology, Catalysis, and Nanotechnology. *Chem. Rev.* **2004,** *104 (1)*, 293-346.

2. Notis, M. R.; Shugar, A. N., Roman Shears: Metallography, Composition and a Historical Approach to Investigation. In *Archaeometallurgy in Europe*, Milan, Italy, 2003; Vol. 1, pp 109-118.

3. Liu, K. H.; Chan, H.; Notis, M. R.; Pigott, V. C., Analytical Electron Microscopy of Early Steel from the Bacqah Valley, Jordan. In *Microbeam Analysis - 1984*, Romig, A. D., Jr.; Goldstein, J. I., Eds. San Francisco Press, Inc.: San Francisco, CA, 1984; pp 261-263.

4. Reibold, M.; Paufler, P.; Levin, A. A.; Kochmann, W.; Patzke, N.; Meyer, D. C. Materials - Carbon Nanotubes in an Ancient Damascus Sabre. *Nature* **2006,** *444 (7117)*, 286-286.

5. Reibold, M.; Patzke, N.; Levin, A. A.; Kochmann, W.; Shakhverdova, I. P.; Paufler, P.; Meyer, D. C. Structure of Several Historic Blades at Nanoscale. *Cryst. Res. Technol.* **2009,** *44 (10)*, 1139-1146.

6. Kochmann, W.; Reibold, M.; Goldberg, R.; Hauffe, W.; Levin, A. A.; Meyer, D. C.; Stephan, T.; Muller, H.; Belger, A.; Paufler, P. Nanowires in Ancient Damascus Steel. *J. Alloy. Compd.* **2004,** *372 (1-2)*, L15-L19.

7. Barnes, J. The Light Scattered and Transmitted by Fine Particles. *Phys. Rev.* **1902,** *15 (6)*, 368-373.

8. Tyndall, J. Action of an Intermittent Beam of Radiant Heat Upon Gaseous Matter. **1881,** *2 (38)*, 110-114.

9. Henri, V. The Determination of the Size of Colloidal Particles. *Trans. Faraday Soc.* **1913,** *9 (1/2)*, 47-53.

10. Svedberg, T.; Nichols, J. B. Determination of Size and Distribution of Size of Particle by Centrifugal Methods. *J. Am. Chem. Soc.* **1923,** *45*, 2910-2917.

11. Svedberg, T.; Rinde, H. The Ultra-Centrifuge, A New Instrument for the Determinition of Size and Distribution of Size of Particle in Amicroscopic Colloids. *J. Am. Chem. Soc.* **1924,** *46*, 2677-2693.

12. Knoll, M.; Ruska, E. The Electron Microscope. *Z. Phys.* **1932,** *78 (5-6)*, 318-339.

13. Ruska, E. In *The Development of the Electron Microscope and of Electron Microscopy*, Nobel Lectures in Physics 1981-1990, Stockholm, Sweden, Frängsmyr, T.; Ekspång, G., Eds. World Scientific Publishing Co.: Stockholm, Sweden, 1986; pp 355-380.

14. Turkevich, J. The World of Fine Particles. *Am. Scientist* **1959,** *47 (1)*, 97-119.

15. Feynman, R. P. There's Plenty of Room at the Bottom. *Eng. Sci.* **1960,** *23 (5)*, 22-36.

16. Edwards, S. A. *The Nanotech Pioneers: Where Are They Taking Us?* 1 ed.; Wiley-VCH Verlag GmbH & Co. KGaA: Weinheim, Germany, 2006; p 257.

17. Speiser, P. Controlled Release of Drugs from Microcapsules and Nanocapsules. **1976,** *13*, 35-35.

18. Speiser, P. Colloids Distribution Conditions in the Pharmaceutical Technology: Coacervation, Adsorption, and Micelle Polymerization. *Prog. Colloid Polym. Sci.* **1976,** *59*, 48-54.

19. Kroto, H. W.; Heath, J. R.; Obrien, S. C.; Curl, R. F.; Smalley, R. E. C_{60}: Buckminsterfullerene. *Nature* **1985,** *318 (6042)*, 162-163.

20. Iijima, S. Helical Microtubules of Graphitic Carbon. *Nature* **1991,** *354 (6348)*, 56-58.

21. Delgado, J. L.; Herranz, M. A.; Martin, N. The Nano-Forms of Carbon. *J. Mater. Chem.* **2008,** *18 (13)*, 1417-1426.

22. Lu, W. B.; Zu, M.; Byun, J. H.; Kim, B. S.; Chou, T. W. State of the Art of Carbon Nanotube Fibers: Opportunities and Challenges. *Adv. Mater.* **2012,** *24 (14)*, 1805-1833.

23. Paradise, M.; Goswami, T. Carbon Nanotubes - Production and Industrial Applications. *Mater. Des.* **2007,** *28 (5)*, 1477-1489.

24. Zhu, Z. G.; Song, W. H.; Burugapalli, K.; Moussy, F.; Li, Y. L.; Zhong, X. H. Nano-Yarn Carbon Nanotube Fiber Based Enzymatic Glucose Biosensor. *Nanotechnology* **2010,** *21 (16)*, 165501.

25. Zhou, F. F.; Xing, D.; Ou, Z. M.; Wu, B. Y.; Resasco, D. E.; Chen, W. R. Cancer Photothermal Therapy in the Near-Infrared Region by Using Single-Walled Carbon Nanotubes. *J. Biomed. Opt.* **2009,** *14 (2)*, 021009.

26. Samanta, S. K.; Pal, A.; Bhattacharya, S.; Rao, C. N. R. Carbon Nanotube Reinforced Supramolecular Gels with Electrically Conducting, Viscoelastic and Near-Infrared Sensitive Properties. *J. Mater. Chem.* **2010,** *20 (33)*, 6881-6890.

27. Gruner, G. Carbon Nanotube Films for Transparent and Plastic Electronics. *J. Mater. Chem.* **2006,** *16 (35)*, 3533-3539.

28. Li, C. L.; Gu, L.; Tong, J. W.; Maier, J. Carbon Nanotube Wiring of Electrodes for High-Rate Lithium Batteries Using an Imidazolium-Based Ionic Liquid Precursor as Dispersant and Binder: A Case Study on Iron Fluoride Nanoparticles. *ACS Nano* **2011,** *5 (4)*, 2930-2938.

29. Mamedov, A. A.; Kotov, N. A.; Prato, M.; Guldi, D. M.; Wicksted, J. P.; Hirsch, A. Molecular Design of Strong Single-Wall Carbon Nanotube/Polyelectrolyte Multilayer Composites. *Nat. Mater.* **2002,** *1 (3)*, 190-194.

30. Kong, J.; Franklin, N. R.; Zhou, C. W.; Chapline, M. G.; Peng, S.; Cho, K. J.; Dai, H. J. Nanotube Molecular Wires as Chemical Sensors. *Science* **2000,** *287 (5453)*, 622-625.

31. Carlson, L. J.; Krauss, T. D. Photophysics of Individual Single-Walled Carbon Nanotubes. *Acc. Chem. Res.* **2008,** *41 (2)*, 235-243.

32. Yu, M. F.; Lourie, O.; Dyer, M. J.; Moloni, K.; Kelly, T. F.; Ruoff, R. S. Strength and Breaking Mechanism of Multiwalled Carbon Nanotubes Under Tensile Load. *Science* **2000,** *287 (5453)*, 637-640.

33. Collins, P. G.; Avouris, P. Nanotubes for Electronics. *Sci.Am.* **2000,** *283 (6)*, 62-69.

34. Rycenga, M.; Cobley, C. M.; Zeng, J.; Li, W. Y.; Moran, C. H.; Zhang, Q.; Qin, D.; Xia, Y. N. Controlling the Synthesis and Assembly of Silver Nanostructures for Plasmonic Applications. *Chem. Rev.* **2011,** *111 (6)*, 3669-3712.

35. Zeng, H. B.; Du, X. W.; Singh, S. C.; Kulinich, S. A.; Yang, S. K.; He, J. P.; Cai, W. P. Nanomaterials via Laser Ablation/Irradiation in Liquid: A Review. *Adv. Funct. Mater.* **2012,** *22 (7)*, 1333-1353.

36. Saito, Y.; Nakahira, T.; Uemura, S. Growth Conditions of Double-Walled Carbon Nanotubes in Arc Discharge. *J. Phys. Chem. B* **2003,** *107 (4)*, 931-934.

37. Burda, C.; Chen, X. B.; Narayanan, R.; El-Sayed, M. A. Chemistry and Properties of Nanocrystals of Different Shapes. *Chem. Rev.* **2005,** *105 (4)*, 1025-1102.

38. Dumke, J. C.; El-Zahab, B.; Challa, S.; Das, S.; Chandler, L.; Tolocka, M.; Hayes, D. J.; Warner, I. M. Lanthanide-Based Luminescent NanoGUMBOS. *Langmuir* **2010,** *26 (19)*, 15599-15603.

39. Li, D.; Xia, Y. N. Electrospinning of Nanofibers: Reinventing the Wheel? *Adv. Mater.* **2004,** *16 (14)*, 1151-1170.

40. Cushing, B. L.; Kolesnichenko, V. L.; O'Connor, C. J. Recent Advances in the Liquid-Phase Syntheses of Inorganic Nanoparticles. *Chem. Rev.* **2004,** *104 (9)*, 3893-3946.

41. Lv, W. Z.; Liu, B.; Qiu, Q.; Wang, F.; Luo, Z. K.; Zhang, P. X.; Wei, S. H. Synthesis, Characterization and Photocatalytic Properties of Spinel $CuAl_2O_4$ Nanoparticles by a Sonochemical Method. *J. Alloy. Compd.* **2009,** *479 (1-2)*, 480-483.

42. Baghbanzadeh, M.; Carbone, L.; Cozzoli, P. D.; Kappe, C. O. Microwave-Assisted Synthesis of Colloidal Inorganic Nanocrystals. *Angew. Chem. Int. Ed.* **2011,** *50 (48)*, 11312-11359.

43. Avouris, P.; Freitag, M.; Perebeinos, V. Carbon-Nanotube Photonics and Optoelectronics. *Nat. Photonics* **2008,** *2 (6)*, 341-350.

44. Liu, Z.; Tabakman, S.; Welsher, K.; Dai, H. J. Carbon Nanotubes in Biology and Medicine: In vitro and in vivo Detection, Imaging and Drug Delivery. *Nano Res.* **2009,** *2 (2)*, 85-120.

45. Xu, Z. P.; Buehler, M. J. Nanoengineering Heat Transfer Performance at Carbon Nanotube Interfaces. *ACS Nano* **2009,** *3 (9)*, 2767-2775.

46. Li, Z. R.; Kandel, H. R.; Dervishi, E.; Saini, V.; Xu, Y.; Biris, A. R.; Lupu, D.; Salamo, G. J.; Biris, A. S. Comparative Study on Different Carbon Nanotube Materials in Terms of Transparent Conductive Coatings. *Langmuir* **2008,** *24 (6)*, 2655-2662.

47. Walden, P. About the Molecular Size and Electrical Conductivity of Some Molten Salts. *Bull. Acad. Imper. Sci. (St. Petersburg)* **1914,** *8*, 405-422.

48. Davy, H. *Researches, Chemical and Philosophical; Chiefly Concerning Nitrous Oxide: or Dephlogisticated Nitrous Air, and its Respiration*. Biggs and Cottle: Bristol, 1800; p 582.

49. Murrill, P. Halides and Perhalides of the Picolines. *J. Am. Chem. Soc.* **1899,** *21 (10)*, 828-854.

50. Leontjewa, A. A. Value of Activation Energy for Ionic Liquids. *Acta Physicochim. URSS* **1939,** *11 (6)*, 861-864.

51. Chum, H. L.; Koch, V. R.; Miller, L. L.; Osteryoung, R. A. Electrochemical Scrutiny of Organometallic Iron Complexes and Hexamethylbenzene in a Room-Temperature Molten-Salt. *J. Am. Chem. Soc.* **1975,** *97 (11)*, 3264-3265.

52. Wilkes, J. S.; Levisky, J. A.; Wilson, R. A.; Hussey, C. L. Dialkylimidazolium Chloroaluminate Melts - A New Class of Room-Temperature Ionic Liquids for Electrochemistry, Spectroscopy, and Synthesis. *Inorg. Chem.* **1982,** *21 (3)*, 1263-1264.

53. Davis, J. H.; Forrester, K. J.; Merrigan, T. Novel Organic Ionic Liquids (OILs) Incorporating Cations Derived From the Antifungal Drug Miconazole. *Tetrahedron Lett.* **1998,** *39 (49)*, 8955-8958.

54. Rutten, F. J. M.; Tadesse, H.; Licence, P. Rewritable Imaging on the Surface of Frozen Ionic Liquids. *Angew. Chem. Int. Ed.* **2007,** *46 (22)*, 4163-4165.

55. Tesfai, A.; El-Zahab, B.; Bwambok, D. K.; Baker, G. A.; Fakayode, S. O.; Lowry, M.; Warner, I. M. Controllable Formation of Ionic Liquid Micro- and Nanoparticles via a Melt-Emulsion-Quench Approach. *Nano Lett.* **2008,** *8 (3)*, 897-901.

56. Tesfai, A.; El-Zahab, B.; Kelley, A. T.; Li, M.; Garno, J. C.; Baker, G. A.; Warner, I. M. Magnetic and Nonmagnetic Nanoparticles from a Group of Uniform Materials Based on Organic Salts. *ACS Nano* **2009,** *3 (10)*, 3244-3250.

57. Freemantle, M. Designer Solvents - Ionic Liquids May Boost Clean Technology Development. *Chem. Eng. News* **1998,** *76 (13)*, 32-37.

58. Handy, S. T. Greener Solvents: Room Temperature Ionic Liquids from Biorenewable Sources. *Chem. Eur. J.* **2003,** *9 (13)*, 2938-2944.

59. Wilkes, J. S. A Short History of Ionic Liquids - From Molten Salts to Neoteric Solvents. *Green Chem.* **2002,** *4 (2)*, 73-80.

60. Del Pópolo, M. G.; Voth, G. A. On the Structure and Dynamics of Ionic Liquids. *J. Phys. Chem. B* **2004,** *108 (5)*, 1744-1752.

61. *CRC Handbook of Chemistry and Physics*. 88th ed.; Lide, D. R., Ed. CRC Press: Boca Raton, FL, 2008; Chapter 8, p 42-51.

62. Earle, M. J.; Esperanca, J.; Gilea, M. A.; Lopes, J. N. C.; Rebelo, L. P. N.; Magee, J. W.; Seddon, K. R.; Widegren, J. A. The Distillation and Volatility of Ionic Liquids. *Nature* **2006,** *439 (7078)*, 831-834.

63. Welton, T. Room-Temperature Ionic Liquids. Solvents for Synthesis and Catalysis. *Chem. Rev.* **1999,** *99 (8)*, 2071-2083.

64. Rogers, R. D.; Seddon, K. R. Ionic Liquids - Solvents of the Future? *Science* **2003,** *302 (5646)*, 792-793.

65. Chambreau, S. D.; Schneider, S.; Rosander, M.; Hawkins, T.; Gallegos, C. J.; Pastewait, M. F.; Vaghjiani, G. L. Fourier Transform Infrared Studies in Hypergolic Ignition of Ionic Liquids. *J. Phys. Chem. A* **2008,** *112 (34)*, 7816-7824.

66. Plechkova, N. V.; Seddon, K. R. Applications of Ionic Liquids in the Chemical Industry. *Chem. Soc. Rev.* **2008,** *37 (1)*, 123-150.

67. Greaves, T. L.; Drummond, C. J. Protic Ionic Liquids: Properties and Applications. *Chem. Rev.* **2008,** *108 (1)*, 206-237.

68. Hurley, F. H.; Wier, T. P. Electrodeposition of Metals from Fused Quaternary Ammonium Salts. *J. Electrochem. Soc.* **1951,** *98 (5)*, 203-206.

69. Wilkes, J. S.; Zaworotko, M. J. Air and Water Stable 1-Ethyl-3-Methylimidazolium Based Ionic Liquids. *J. Chem. Soc. Chem. Commun.* **1992,** *(13)*, 965-967.

70. Appleby, D.; Hussey, C. L.; Seddon, K. R.; Turp, J. E. Room-Temperature Ionic Liquids as Solvents for Electronic Absorption-Spectroscopy of Halide-Complexes. *Nature* **1986,** *323 (6089)*, 614-616.

71. Dupont, J. From Molten Salts to Ionic Liquids: A "Nano" Journey. *Acc. Chem. Res.* **2011,** *44 (11)*, 1223-1231.

72. Davis, J. H. Task-Specific Ionic Liquids. *Chem. Lett.* **2004,** *33 (9)*, 1072-1077.

73. Tang, S. K.; Baker, G. A.; Zhao, H. Ether- and Alcohol-Functionalized Task-Specific Ionic Liquids: Attractive Properties and Applications. *Chem. Soc. Rev.* **2012,** *41 (10)*, 4030-4066.

74. Bwambok, D. K.; El-Zahab, B.; Challa, S. K.; Li, M.; Chandler, L.; Baker, G. A.; Warner, I. M. Near-Infrared Fluorescent NanoGUMBOS for Biomedical Imaging. *ACS Nano* **2009,** *3 (12)*, 3854-3860.

75. Das, S.; Bwambok, D.; El-Zahab, B.; Monk, J.; de Rooy, S. L.; Challa, S.; Li, M.; Hung, F. R.; Baker, G. A.; Warner, I. M. Nontemplated Approach to Tuning the Spectral Properties of Cyanine-Based Fluorescent NanoGUMBOS. *Langmuir* **2010,** *26 (15)*, 12867-12876.

76. Regmi, B. P.; Monk, J.; El-Zahab, B.; Das, S.; Hung, F. R.; Hayes, D. J.; Warner, I. M. A Novel Composite Film for Detection and Molecular Weight Determination of Organic Vapors. *J. Mater. Chem.* **2012,** *22 (27)*, 13732-13741.

77. de Rooy, S. L.; Das, S.; Li, M.; El-Zahab, B.; Jordan, A.; Lodes, R.; Weber, A.; Chandler, L.; Baker, G. A.; Warner, I. M. Ionically Self-Assembled, Multi-Luminophore One-Dimensional Micro- and Nanoscale Aggregates of Thiacarbocyanine GUMBOS. *J. Phys. Chem. C* **2012,** *116 (14)*, 8251-8260.

78. Jordan, A. N.; Das, S.; Siraj, N.; de Rooy, S. L.; Li, M.; El-Zahab, B.; Chandler, L.; Baker, G. A.; Warner, I. M. Anion-Controlled Morphologies and Spectral Features of Cyanine-Based NanoGUMBOS - An Improved Photosensitizer. *Nanoscale* **2012,** *4 (16)*, 5031-5038.

79. Li, M.; Gardella, J.; Bwambok, D. K.; El-Zahab, B.; de Rooy, S.; Cole, M.; Lowry, M.; Warner, I. M. Combinatorial Approach to Enantiomeric Discrimination: Synthesis and F-19 NMR Screening of a Chiral Ionic Liquid-Modified Silane Library. *J. Comb. Chem.* **2009,** *11 (6)*, 1105-1114.

80. Li, M.; De Rooy, S. L.; Bwambok, D. K.; El-Zahab, B.; DiTusa, J. F.; Warner, I. M. Magnetic Chiral Ionic Liquids Derived from Amino Acids. *Chem. Commun.* **2009,** *(45)*, 6922-6924.

81. Bwambok, D. K.; Challa, S. K.; Lowry, M.; Warner, I. M. Amino Acid-Based Fluorescent Chiral Ionic Liquid for Enantiomeric Recognition. *Anal. Chem.* **2010,** *82 (12)*, 5028-5037.

82. de Rooy, S. L.; Li, M.; Bwambok, D. K.; El-Zahab, B.; Challa, S.; Warner, I. M. Ephedrinium-Based Protic Chiral Ionic Liquids for Enantiomeric Recognition. *Chirality* **2011,** *23 (1)*, 54-62.

83. Cole, M. R.; Li, M.; El-Zahab, B.; Janes, M. E.; Hayes, D.; Warner, I. M. Design, Synthesis, and Biological Evaluation of beta-Lactam Antibiotic-Based Imidazolium- and Pyridinium-Type Ionic Liquids. *Chem. Biol. Drug Des.* **2011,** *78 (1)*, 33-41.

84. Deng, N.; Li, M.; Zhao, L. J.; Lu, C. F.; de Rooy, S. L.; Warner, I. M. Highly Efficient Extraction of Phenolic Compounds by Use of Magnetic Room Temperature Ionic Liquids for Environmental Remediation. *J. Hazard. Mater.* **2011,** *192 (3)*, 1350-1357.

85. Li, M.; Ganea, G. M.; Lu, C. F.; De Rooy, S. L.; El-Zahab, B.; Fernand, V. E.; Jin, R. Y.; Aggarwal, S.; Warner, I. M. Lipophilic Phosphonium-Lanthanide Compounds with Magnetic, Luminescent, and Tumor Targeting Properties. *J. Inorg. Biochem.* **2012,** *107 (1)*, 40-46.

86. Zhang, Y. Q.; Gao, H. X.; Guo, Y.; Joo, Y. H.; Shreeve, J. M. Hypergolic N,N-Dimethylhydrazinium Ionic Liquids. *Chem. Eur. J.* **2010,** *16 (10)*, 3114-3120.

87. Berg, U.; Gallo, R. Steric Effects in S_N2 Reactions - Determination of Transition-State Structures for the Quaternization of 2-Alklpyridines and 2-Alkylthiazoles by a Combined

Experimental and Molecular Mechanics Procedure. *Acta Chem. Scand. B* **1983,** *37 (8)*, 661-673.

88. Mendeleev, D. I. The Periodic Regularity of the Chemical Elements. *Ann. Chem. Pharm.* **1871,** *8*, 133-229.

89. Mendeleev, D. I. The Correlation of the Properties and Atomic Weights of the Elements. *Zh. Russ. Khim. Obshch.* **1869,** *1*, 60-77.

90. Tomaschek, R. Phosphorescence Characteristics of the Rare Earths in the Earth-Alkali Phosphors. *Ann. d. Physik* **1924,** *75 (18)*, 109-142.

91. Tomaschek, R.; Deutschbein, O. Fluorescence of Pure Salts of the Rare Earths. *Nature* **1933,** *131*, 473-473.

92. Weissman, S. I. Intramolecular Energy Transfer - The Fluorescence of Complexes of Europium. *J. Chem. Phys.* **1942,** *10 (4)*, 214-217.

93. Stokes, G. G. On the Change of Refrangibility of Light. *Phil. Trans. R. Soc. Lond.* **1852,** *142*, 463-562.

94. Rutherford, E. The Structure of the Atom. *Phil. Mag. S. 6* **1914,** *27 (157-62)*, 488-498.

95. Bohr, N. On the Series Spectrum of Hydrogen and the Structure of the Atom. *Phil. Mag. S. 6* **1915,** *29 (170)*, 332-335.

96. Bohr, N. On the Effect of Electric and Magnetic Fields on Spectral Lines. *Phil. Mag. S. 6* **1914,** *27 (157-62)*, 506-524.

97. Jablonski, A. About the Emergence of the Broad Absorption and Fluorescence Bands in Dye Solutions. *Z. Phys.* **1932,** *73 (7-8)*, 460-469.

98. Jablonski, A. Efficiency of Anti-Stokes Fluorescence in Dyes. *Nature* **1933,** *131*, 839-840.

99. Binnemans, K.; Görller-Walrand, C. On the Color of the Trivalent Lanthanide Ions. *Chem. Phys. Lett.* **1995,** *235 (3-4)*, 163-174.

100. Stern, O.; Volmer, M. The Fading Time of Fluorescence. *Phys. Z.* **1919,** *20*, 183-188.

101. Hund, F. Concerning the Interpretation of Complex Spectra, Especially the Elements Scandium to Nickel. *Z. Phys.* **1925,** *33*, 345-371.

102. Bünzli, J.-C. G.; Eliseeva, S. V. Basics of Lanthanide Photophysics. In *Lanthanide Luminescence: Photophysical, Analytical, and Biological Aspects*, 1st ed.; Hänninen, P.; Härmä, H., Eds. Springer: Berlin, 2011; Vol. 7, pp 1-45.

103. Bril, A.; Wanmaker, W. L. Fluorescent Properties of Some Europium-Activated Phosphors. *J. Electrochem. Soc.* **1964,** *111 (12),* 1363-1368.

104. Bünzli, J.-C. G. Lanthanide Luminescence for Biomedical Analyses and Imaging. *Chem. Rev.* **2010,** *110 (5),* 2729-2755.

105. Kostova, I. Lanthanides as Anticancer Agents. *Curr. Med. Chem. - Anti-Cancer Agents* **2005,** *5 (6),* 591-602.

106. Bünzli, J.-C. G. Luminescent Lanthanide Probes as Diagnostic and Therapeutic Tools. In *Metal Complexes in Tumor Diagnosis and as Anticancer Agents*, 1st ed.; Sigel, H., Ed. Marcel Dekker Inc.: New York, 2004; Vol. 42, pp 39-75.

107. Celli, J. P.; Spring, B. Q.; Rizvi, I.; Evans, C. L.; Samkoe, K. S.; Verma, S.; Pogue, B. W.; Hasan, T. Imaging and Photodynamic Therapy: Mechanisms, Monitoring, and Optimization. *Chem. Rev.* **2010,** *110 (5),* 2795-2838.

108. Epstein, J. H. Phototherapy and Photochemotherapy. *N. Engl. J. Med.* **1990,** *322 (16),* 1149-1151.

109. Briviba, K.; Klotz, L. O.; Sies, H. Toxic and Signaling Effects of Photochemically or Chemically Generated Singlet Oxygen in Biological Systems. *Biol. Chem.* **1997,** *378 (11),* 1259-1265.

110. Binnemans, K. Lanthanides and Actinides in Ionic Liquids. *Chem. Rev.* **2007,** *107 (6),* 2592-2614.

111. Nockemann, P.; Beurer, E.; Driesen, K.; Van Deun, R.; Van Hecke, K.; Van Meervelt, L.; Binnemans, K. Photostability of a Highly Luminescent Europium Beta-Diketonate Complex in Imidazolium Ionic Liquids. *Chem. Commun.* **2005,** *(34),* 4354-4356.

112. Puntus, L. N.; Schenk, K. J.; Bünzli, J.-C. G. Intense Near-Infrared Luminescence of a Mesomorphic Ionic Liquid Doped with Lanthanide Beta-Diketonate Ternary Complexes. *Eur. J. Inorg. Chem.* **2005,** *(23),* 4739-4744.

113. Jensen, M. P.; Neuefeind, J.; Beitz, J. V.; Skanthakumar, S.; Soderholm, L. Mechanisms of Metal Ion Transfer into Room-Temperature Ionic Liquids: The Role of Anion Exchange. *J. Am. Chem. Soc.* **2003,** *125 (50),* 15466-15473.

114. Cocalia, V. A.; Jensen, M. P.; Holbrey, J. D.; Spear, S. K.; Stepinski, D. C.; Rogers, R. D. Identical Extraction Behavior and Coordination of Trivalent or Hexavalent f-Element Cations Using Ionic Liquid and Molecular Solvents. *Dalton Trans.* **2005,** *(11),* 1966-1971.

115. Mekkii, S.; Wai, C. M.; Billard, I.; Moutiers, G.; Burt, J.; Yoon, B.; Wang, J. S.; Gaillard, C.; Ouadi, A.; Hesemann, P. Extraction of Lanthanides from Aqueous Solution by Using Room-Temperature Ionic Liquid and Supercritical Carbon Dioxide in Conjunction. *Chem. Eur. J.* **2006,** *12 (6)*, 1760-1766.

116. Lunstroot, K.; Driesen, K.; Nockemann, P.; Van Hecke, K.; Van Meervelt, L.; Görller-Walrand, C.; Binnemans, K.; Bellayer, S.; Viau, L.; Le Bideau, J.; Vioux, A. Lanthanide-Doped Luminescent Ionogels. *Dalton Trans.* **2009,** *(2)*, 298-306.

117. Hornback, N. B. Historical Aspects of Hyperthermis in Cancer Therapy. *Radiol. Clin. N. Am.* **1989,** *27 (3)*, 481-488.

118. Glazer, E. S.; Curley, S. A. The Ongoing History of Thermal Therapy for Cancer. *Surg. Oncol. Clin. N. Am.* **2011,** *20 (2)*, 229-235.

119. Duffell, E. Curative Power of Fever. *Lancet* **2001,** *358 (9289)*, 1276-1276.

120. Byrne, J. *Clinical Notes on the Electric Cautery in Uterine Surgery*. William Wood & Company: New York, 1873; p 68.

121. Bone, R. C.; Balk, R. A.; Cerra, F. B.; Dellinger, R. P.; Fein, A. M.; Knaus, W. A.; Schein, R. M. H.; Sibbald, W. J. Definitions for Sepsis and Organ Failure and Guidelines for the Use of Innovative Therapies in Sepsis. *Chest* **1992,** *101 (6)*, 1644-1655.

122. Dinarello, C. A. Infection, Fever, and Exogenous and Endogenous Pyrogens: Some Concepts Have Changed. *J. Endoxtin Res.* **2004,** *10 (4)*, 201-222.

123. Atkins, E. Fever - The Old and the New. *J. Infect. Dis.* **1984,** *149 (3)*, 339-348.

124. Busch, W. Proceedings on the Influence of Severe Erysipela on Organized Sarcoma. *Akad. Wiss. Nat. Lng. Wirtschaftswiss. Vortr.* **1866,** *23*, 28.

125. Whitrow, M. Wagner-Jauregg and Fever Therapy. *Med. Hist.* **1990,** *34 (3)*, 294-310.

126. Byrne, J. A Digest of 20 Years' Experience in the Treatment of Cancer of the Uterus by Galvanocautery. *Am. J. Obstet. Gynecol.* **1899,** *22*, 1052.

127. Coley, W. B. The Treatment of Malignant Tumors by Repeated Innoculations of Erysipela with a Report of Ten Original Cases. *Am. J. Med. Sci.* **1893,** *105*, 487.

128. McCarty, M. F.; Whitaker, J. Manipulating Tumor Acidification as a Cancer Treatment Strategy. *Altern. Med. Rev.* **2010,** *15 (3)*, 264-272.

129. Tainter, M. L.; Stockton, A. B.; Cutting, W. C. Use of Dinitrophenol in Obesity and Related Conditions - A Progress Report. *J. Am. Med. Assoc.* **1933,** *101 (19)*, 1472-1475.

130. Blaikie, F. H.; Brown, S. E.; Samuelsson, L. M.; Brand, M. D.; Smith, R. A. J.; Murphy, M. P. Targeting Dinitrophenol to Mitochondria: Limitations to the Development of a Self-Limiting Mitochondrial Protonophore. *Biosci. Rep.* **2006,** *26 (3)*, 231-243.

131. Andreyev, A. Y.; Bondareva, T. O.; Dedukhova, V. I.; Mokhova, E. N.; Skulachev, V. P.; Tsofina, L. M.; Volkov, N. I.; Vygodina, T. V. THE ATP/ADP-Antiporter is Involved in the Uncoupling Effect of Fatty-Acids on Mitochondria. *Eur. J. Biochem.* **1989,** *182 (3)*, 585-592.

132. Michels, M.; Bakker, E. P. Generation of a Large, Protonophore-Sensitive Proton Motive Force and pH Difference in the Acidophilic Bacteria Thermoplasma Acidophilum and Bacillus-Acidocaldarius. *J. Bacteriol.* **1985,** *161 (1)*, 231-237.

133. Adler, J. R.; Murphy, M. J.; Chang, S. D.; Hancock, S. L. Image-Guided Robotic Radiosurgery. *Neurosurgery* **1999,** *44 (6)*, 1299-1306.

134. Chang, S. D.; Adler, J. R. Robotics and Radiosurgery - The CyberKnife. *Stereotact. Funct. Neurosurg.* **2001,** *76 (3-4)*, 204-208.

135. King, C. R.; Lehmann, J.; Adler, J. R.; Hai, J. CyberKnife Radiotherapy for Localized Prostate Cancer: Rationale and Technical Feasibility. *Technol. Cancer Res. Treat.* **2003,** *2 (1)*, 25-29.

136. Podder, T.; Fried, D.; Holland, B.; Rosenman, J.; Biswas, T. SU-E-T-412: Can Cyberknife SBRT be an Alternative to Brachytherapy for Cervical Cancer Treatment? *Med. Phys.* **2012,** *39 (6)*, 3799.

137. Herschel, W. Experiments on the Refrangibility of the Invisible Rays of the Sun. *Phil. Trans. R. Soc. Lond.* **1800,** *90*, 284-292.

138. Bashkatov, A. N.; Genina, E. A.; Kochubey, V. I.; Tuchin, V. V. Optical Properties of Human Skin, Subcutaneous and Mucous Tissues in the Wavelength Range from 400 to 2000 nm. *J. Phys. D: Appl. Phys.* **2005,** *38 (15)*, 2543-2555.

139. Hirsch, L. R.; Stafford, R. J.; Bankson, J. A.; Sershen, S. R.; Rivera, B.; Price, R. E.; Hazle, J. D.; Halas, N. J.; West, J. L. Nanoshell-Mediated Near-Infrared Thermal Therapy of Tumors Under Magnetic Resonance Guidance. *Proc. Natl. Acad. Sci. USA* **2003,** *100 (23)*, 13549-13554.

140. Einstein, A. On the Quantum Theory of Radiation. *Phys. Z.* **1917,** *18*, 121-128.

141. Ladenburg, R. W. Studies on the Anomalous Dispersion of Excited Gases. *Z. Phys.* **1928,** *48 (1-2)*, 15-25.

142. Fabrikant, V. A. The Emission Mechanism of a Gas Discharge. *Electronic and Ion Devices (Trudy of VEI)* **1940,** *41*, 236-296.

143. Lamb, W. E.; Retherford, R. C. Fine Structure of the Hydrogen Atom by a Microwave Method. *Phys. Rev.* **1947,** *72 (3)*, 241-243.

144. Brossel, J.; Kastler, A. The Detection of Excited Magnetic Resonance Levels - The Effect of Depolarized Optical Resonance and Fluorescence Radiation. *Comptes Rendus* **1949,** *229 (23)*, 1213-1215.

145. Gordon, J. P.; Zeiger, H. J.; Townes, C. H. Molecular Microwave Oscillator and New Hyperfine Structure in the Microwave Spectrum of NH_3. *Phys. Rev.* **1954,** *95 (1)*, 282-284.

146. McQuarrie, D. A.; Simon, J. D. Lasers, Laser Spectroscopy, and Photochemistry. In *Physical Chemistry: A Molecular Approach*, 1st ed.; McGuire, A., Ed. University Science Books: Sausalito, 1997; pp 604-609.

147. Schawlow, A. L.; Townes, C. H. Infrared and Optical Masers. *Phys. Rev.* **1958,** *112 (6)*, 1940-1949.

148. Maiman, T. H. Stimulated Optical Radiation in Ruby. *Nature* **1960,** *187 (4736)*, 493-494.

149. Harris, T. J. High-Speed Photograms of Laser-Induced Heating. *IBM J. Res. Dev.* **1963,** *7 (4)*, 342-344.

150. Ready, J. F. Development of Plume of Material Vaporized by Giant-Pulse Laser. *Appl. Phys. Lett.* **1963,** *3 (1)*, 11-13.

151. Ready, J. F. Effects Due to Absorption of Laser Radiation. *J. Appl. Phys.* **1965,** *36 (2)*, 462-468.

152. McGuff, P. E.; Roeber, F.; Gottlieb, L. S.; Bushnell, D.; Deterling, R. A.; Fahimi, H. D. Laser Treatment of Experimental Malignant Tumours. *Can. Med. Assoc. J.* **1964,** *91 (21)*, 1089-1095.

153. Cavalier, R.; Ciocatto, E. C.; Giovanella, B. C.; Heidelbe, C.; Johnson, R. O.; Margotti, M.; Mondovi, B.; Moricca, G.; Rossifan, A. Selective Heat Sensitivity of Cancer Cells - Biochemical and Clinical Studies. *Cancer* **1967,** *20 (9)*, 1351-1381.

154. Crile, G. Selective Destruction of Cancers After Exposure to Heat. *Ann. Surg.* **1962,** *156 (3)*, 404-407.

155. Giovanella, B. C.; Lohman, W. A.; Heidelbe, C. Effects of Elevated Temperatures and Drugs on Viability of L1210 Leukemia Cells. *Cancer Res.* **1970,** *30 (6)*, 1623-1631.

156. Hall, R. R.; Schade, R. O. K.; Swinney, J. Effects of Hyperthermia on Bladder Cancer. *Br. Med. J.* **1974,** *2 (5919)*, 593-594.

157. Overgaar, K.; Overgaar, J. Investigations on Possibility of a Thermic Tumor Therapy: Short-Wave Treatment of a Transplanted Isologous Mouse Mammary Carcinoma. *Eur. J. Cancer* **1972,** *8 (1)*, 65-68.

158. Stehlin, J. S.; Giovanella, B. C.; Ipolyi, P. D. D.; Muenz, L. R.; Anderson, R. F. Results of Hyperthermic Perfusion for Melanoma of Extremities. *Surg. Gynecol. Obstet.* **1975,** *140 (3)*, 339-348.

159. Tian, Q. W.; Tang, M. H.; Sun, Y. G.; Zou, R. J.; Chen, Z. G.; Zhu, M. F.; Yang, S. P.; Wang, J. L.; Wang, J. H.; Hu, J. Q. Hydrophilic Flower-Like CuS Superstructures as an Efficient 980 nm Laser-Driven Photothermal Agent for Ablation of Cancer Cells. *Adv. Mater.* **2011,** *23 (31)*, 3542-3547.

160. Ghosh, S.; Dutta, S.; Gomes, E.; Carroll, D.; D'Agostino, R.; Olson, J.; Guthold, M.; Gmeiner, W. H. Increased Heating Efficiency and Selective Thermal Ablation of Malignant Tissue with DNA-Encased Multiwalled Carbon Nanotubes. *ACS Nano* **2009,** *3 (9)*, 2667-2673.

161. Lovell, J. F.; Jin, C. S.; Huynh, E.; Jin, H. L.; Kim, C.; Rubinstein, J. L.; Chan, W. C. W.; Cao, W. G.; Wang, L. V.; Zheng, G. Porphysome Nanovesicles Generated by Porphyrin Bilayers for Use as Multimodal Biophotonic Contrast Agents. *Nat. Mater.* **2011,** *10 (4)*, 324-332.

162. Loeb, L. Further Investigations in Transplantation of Tumors. *J. Med. Res.* **1902,** *8 (1)*, 44-73.

163. Bardhan, R.; Chen, W. X.; Perez-Torres, C.; Bartels, M.; Huschka, R. M.; Zhao, L. L.; Morosan, E.; Pautler, R. G.; Joshi, A.; Halas, N. J. Nanoshells with Targeted Simultaneous Enhancement of Magnetic and Optical Imaging and Photothermal Therapeutic Response. *Adv. Funct. Mater.* **2009,** *19 (24)*, 3901-3909.

164. Hayashi, K.; Moriya, M.; Sakamoto, W.; Yogo, T. Chemoselective Synthesis of Folic Acid-Functionalized Magnetite Nanoparticles via Click Chemistry for Magnetic Hyperthermia. *Chem. Mat.* **2009,** *21 (7)*, 1318-1325.

165. Bae, K. H.; Park, M.; Do, M. J.; Lee, N.; Ryu, J. H.; Kim, G. W.; Kim, C.; Park, T. G.; Hyeon, T. Chitosan Oligosaccharide-Stabilized Ferrimagnetic Iron Oxide Nanocubes for Magnetically Modulated Cancer Hyperthermia. *ACS Nano* **2012,** *6 (6)*, 5266-5273.

Chapter 2. Lanthanide-Based Luminescent NanoGUMBOS*

2.1 Introduction

The transfer of excitation energy directly to the lanthanide metal results in relaxation through photon emission. Therefore, trivalent lanthanide (Ln) luminescence requires energy transfer from a donor molecule because of shielded 4*f* valence subshells as a result of higher outlying subshells ($5s^2$ and $5p^6$) from the Xe core.[1-2] The process of lanthanide luminescence is enabled when a donor (i.e. ligand) absorbs a photon followed by transfer of energy through processes of nonradiative relaxations (e.g. intersystem crossing, intra-ligand charge transfer, or ligand-to-metal charge transfer). Common characteristics of lanthanide emission are intense-narrow peaks, with relatively long lifetimes, and good photostability due to shielded 4*f*-orbital. Owing to these distinctive luminescence properties, lanthanides have found many interesting analytical applications.[3-5] Recently, several studies reporting some of the unique spectral properties of lanthanides have also been reported. For example, near infrared emission,[6] upconversion capabilities,[7-8] and biological therapeutic applications[9-10] have made them attractive alternatives to organic fluorophores, quantum dots, and laser materials.[11]

Covalently binding or encapsulating lanthanides in nanoparticles have also been reported to yield fluorescent and paramagnetic nanoparticles.[10, 12-13] The most commonly used nanocarrier of lanthanide containing species is silica. In a recent report, lanthanide-containing silica nanoparticles have been prepared by coordinating lanthanides to polymers, such as terephthalates, for integrated optics and electroluminescent materials, and doped as antennas for biolabels in immunoassays.[8-9, 14-16] Lanthanide-containing nanoparticles have been found to maintain their characteristic emission lines relative to Ln (III) ions dissolved in solution.[17-20]

* Reprinted (adapted) with permission from Dumke, J. C.; El-Zahab, B.; Challa, S.; Das, S.; Chandler, L.; Tolocka, M.; Hayes, D. J.; Warner, I. M. Lanthanide-Based Luminescent NanoGUMBOS. *Langmuir* **2010**, *26 (19)*, 15599-15603. Copyright 2012, American Chemical Society.

Lanthanides coordinated with ionic liquids have also been reported.[21] Combining ionic liquids with lanthanides allows for a concerted use of the favorable photoproperties of the rare earths and exploitation of the tunability of ionic liquids.[22] Ionic liquids have also been used as alternative solvents in synthesis and catalysis to replace conventional organic solvents.[23] By definition, ionic liquids consist solely of cations and anions and have melting points at 100 ºC or below.[24] Since many higher melting salts are of interest to our research group and do not fit this general definition (25 – 250 ºC), we have recently coined the term ***G***roup of ***U***niform ***M***aterials ***B***ased on ***O***rganic ***S***alts (**GUMBOS**) for our studies.[25]

Herein, we report on the preparation, characterization, and studies of the spectral properties of lanthanide containing nanoGUMBOS. The possibility of tuning the properties of GUMBOS by exchanging the cation or anion allows for a wide range of potential applications that extend into photochemical catalysis, sensory devices, photovoltaics, and many analytical applications.[24-27]

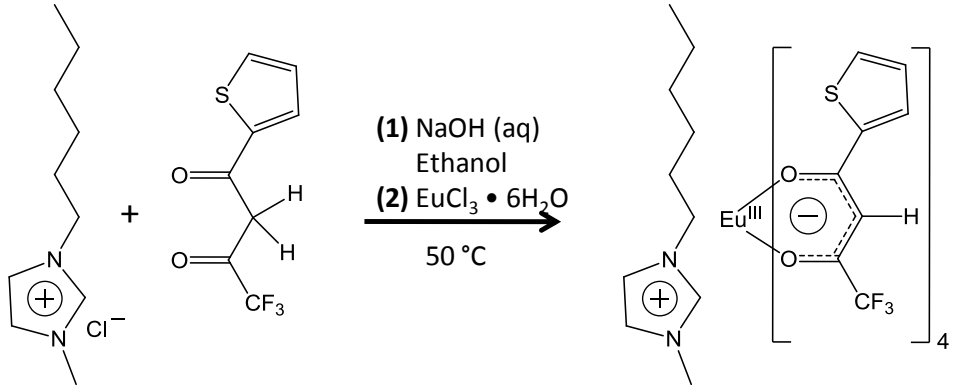
2.2 Synthesis and Characterization of Europium (III) GUMBOS and NanoGUMBOS

2.2.1 Synthesis and Characterization of Europium (III) GUMBOS

The following synthetic procedure was modified from Nockemann, *et al.*: 1.5 mmol 1-hexyl-3-methylimidazolium chloride ([C_6mim][Cl]), 6 mmol 2-thenoyltrifluoroacetone (tta) β-diketone, and 6 mmol of 1.0 M aqueous sodium hydroxide (NaOH) were mixed simultaneously, followed by addition of spectroscopic-grade ethanol (Scheme 2.1).[28] The mixture was vortexed until the material was fully dissolved at room temperature. An aqueous solution of 0.1 M of europium (III) chloride hexahydrate was added to the sample at 50 °C under agitation for 90 minutes. The sample was allowed to cool to room temperature overnight. The decantant was removed and the remaining precipitate was washed and filtered using a Büchner funnel with

chilled triply-distilled water. The solid was lyophilized for 30 hours to remove excess water. The final $[C_6mim][Eu(tta)_4]$ product was a yellow powder and was stored in the dark at room temperature. A DSC q100 Differential Scanning Calorimeter instrument was used to measure the melting point of the solid bulk GUMBOS, 121.33 °C (Figure 2.1)

Scheme 2.1 Reaction scheme of the formation of $[C_6mim][Eu(tta)_4]$.



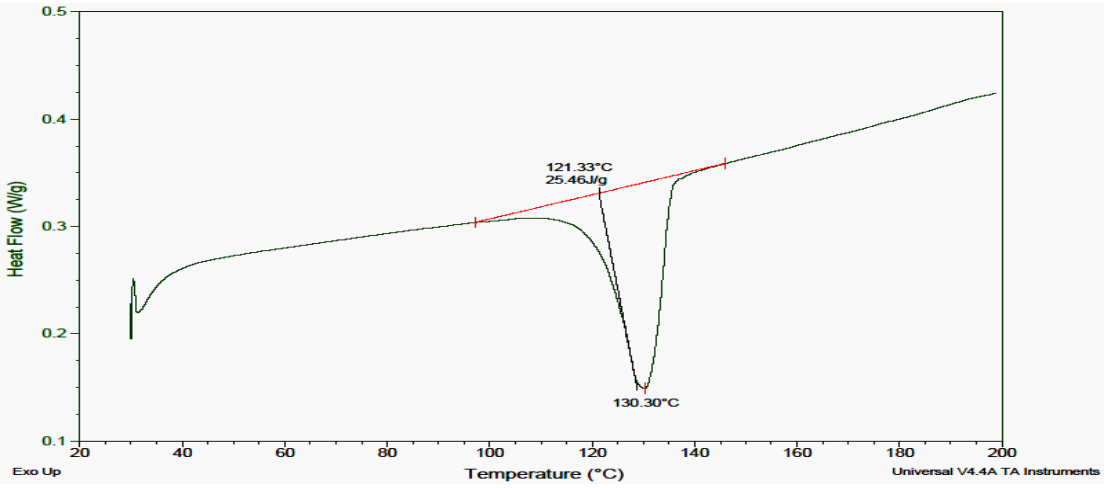
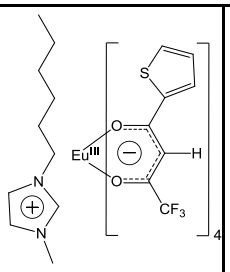
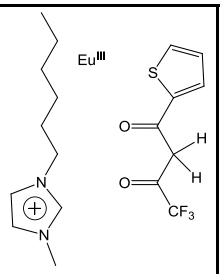


Figure 2.1 Differential scanning calorimetry melting point of the GUMBOS, $[C_6mim][Eu(tta)_4]$.

Elemental analysis supports the complete formation of the GUMBOS opposed to the materials existing independently (Table 2.1). Chelation of the β-diketone to the europium (III) metal can be qualitatively confirmed by exciting the material with a long-wave UV lamp. The europium (III) will not emit luminescence unless a donor molecule is chelated and transfers energy to the lower-lying f-orbitals.

Table 2.1 Elemental analysis (CHNOFS-results) of the dry GUMBOS including the theoretical element percentage of the elements with the β-diketonate chelated to the europium (III) (i.e. GUMBOS and nanoGUMBOS) and if there was not chelation. The percent difference supports that the β-diketone chelates to the europium (III).

Elemental Analysis					
Element	Experimental %	 Theor.%	%Diff.	 Theor.%	%Diff.
C	41.24	41.90	1.6	41.76	1.2
H	2.78	2.93	5.1	3.25	14.5
N	2.36	2.33	1.3	2.32	1.7
O	11.15	10.63	4.9	10.60	5.2
F	19.21	18.94	1.4	18.87	1.8
S	10.29	10.65	3.4	10.62	3.1

2.2.2 Synthesis and Characterization of Europium (III) NanoGUMBOS

A 0.24 mM $[C_6mim][Eu(tta)_4]$ solution in acetonitrile was prepared and then pressure nebulized at 32 psi to generate aerosol. The aerosol was then carried through a silica drier to remove humidity, followed by passage through a 400 °C tube furnace to evaporate the solvent. The dry particles were then collected on a 0.45 μm PTFE membrane filter (Whatman Gmbh) and then resuspended in distilled water through bath sonication. To characterize the particles, 2 μL of the suspension were drop cast on a 400 mesh ultrathin carbon-film copper grid. Transmission

electron microscope (TEM) images from a Delong LVEM5 instrument showed relatively uniform and near-spherical particles with an average particle size of 39.5 ± 8.4 nm (Figure 2.2).

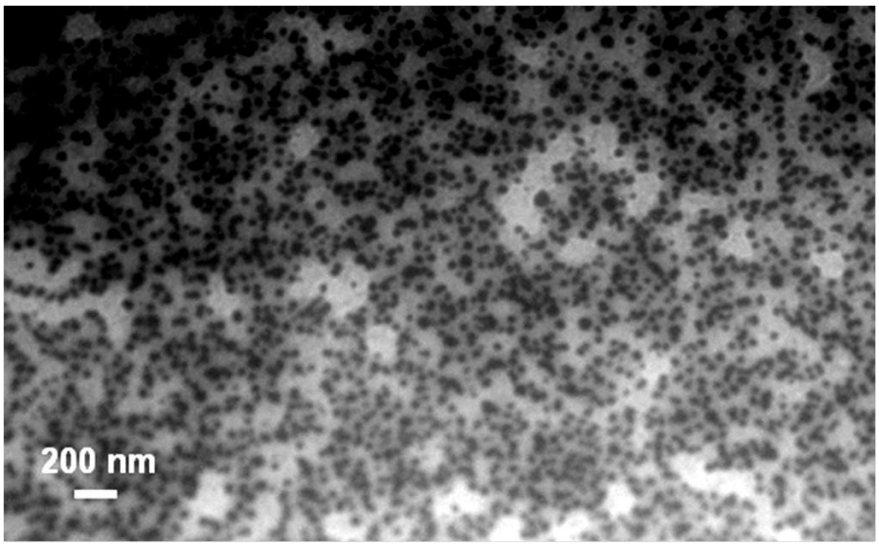


Figure 2.2 TEM image of $[C_6mim][Eu(tta)_4]$ nanoGUMBOS preparated using the aerosolization process. The particles had an average diameter of 39.5 ± 8.4 nm.

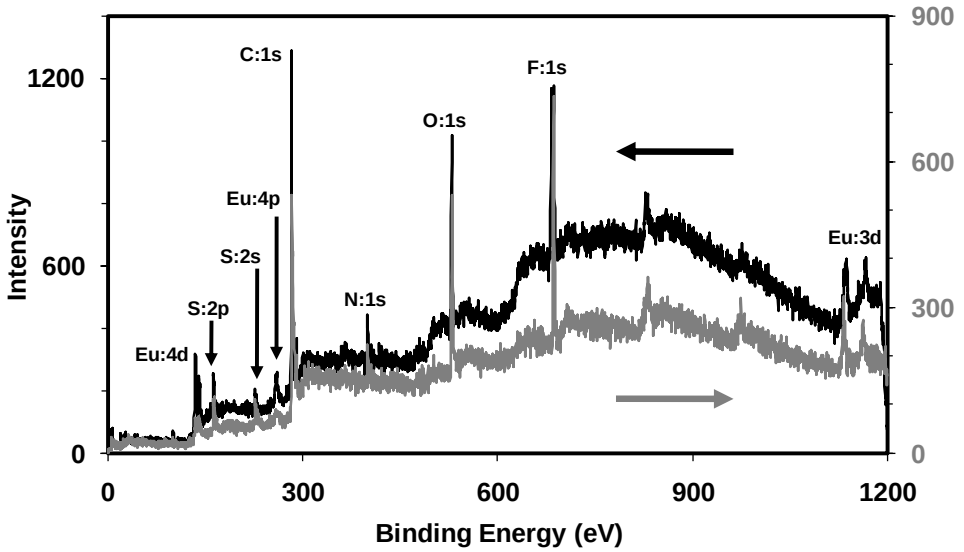


Figure 2.3 XPS spectra of the $[C_6mim][Eu(tta)_4]$ dry GUMBOS (gray) and dry nanoGUMBOS (black).

Confirmation of the molecular composition of the nanoGUMBOS was performed using a Kratos Axis 165 X-ray photoelectron spectroscopy (XPS) with an Al K_α (1486.6 eV) anode. XPS provides information on inner-shell electrons at the valence levels in order to determine the

electronic states and composition of the unknown material.[29] As shown in Figure 2.3, the XPS spectrum of the dry GUMBOS was nearly identical when compared to the dry nanoGUMBOS. Nevertheless, the overall intensity increased and the binding energy of europium's 3d level increased in intensity, suggesting more exposure of europium's valence shell in the nanoGUMBOS than in the bulk GUMBOS.[29]

2.3 Spectral Properties of Europium (III) GUMBOS and NanoGUMBOS

2.3.1 Calculation of Förster Resonance Energy Transfer (FRET) Parameters

The spectral overlap integrals for donor ([C_6mim]):acceptor (europium (III)) was calculated using the formula[2]

$$J(\lambda) = \int_0^\infty \varepsilon(\lambda) f(\lambda) \lambda^4 d\lambda \qquad \text{Equation 2.1}$$

where, J(λ) is the overlap integral, ε is the extinction coefficient of the of the acceptor, f is the normalized emission spectrum of the donor and λ is the wavelength. In this manuscript, the overlap integrals are also expressed as percentages of the maximum value possible.[30] The energy transfer efficiencies are calculated using the formula

$$E = 1 - \frac{F_{DA}}{F_D} \qquad \text{Equation 2.2}$$

where, F_{DA} and F_D are the integrated fluorescence intensity of the donor in the presence and absence of acceptor, respectively.[31] The J(λ) and E values in Table 2.2 were calculated from the observed energy transfer from the [C_6mim] to the europium (III) in aqueous and ethanol solutions when excited at 340 nm with slit widths at 5 nm. A concentration of 0.5 M [C_6mim] and 0.5 M europium (III) was compared to show that the pure 0.5 M [C_6mim] has higher emission intensity than when 0.5 M europium (III) is in the solution (Figure 2.4). In addition, the emission intensity for europium (III) is higher with [C_6mim] than without, supporting that the

imidazolium is contributing energy transfer to the lanthanide. The energy transfer was more efficient in an organic solvent than aqueous due to the polarity differences of the compounds.[32]

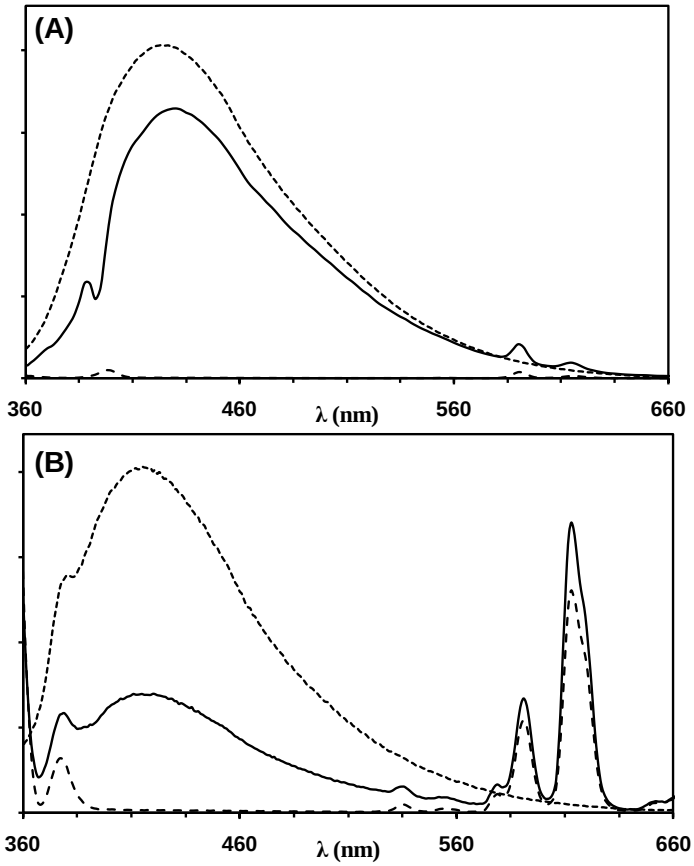


Figure 2.4 Energy transfer was observed from the [C_6mim] to the europium (III) in aqueous (A) and ethanol (B) solutions. Concentrations of pure 0.5 M [C_6mim] (dotted line) and pure 0.5 M europium (III) (dashed line) were compared to show that the mixture (bold line) had higher europium (III) emission intensity.

Table 2.2 The overlap integral (J) and energy transfer efficiency (E) from donor (C_6mim^+) to acceptor (Eu^{3+}) in a 1:1 ratio.

Material (solvent)	J (cm^6mol^{-1})	E
1) GUMBOS (ethanol)	3.96×10^{-15}	65.7%
2) NanoGUMBOS (water)	2.36×10^{-16}	7.48%

2.4 Spectral Properties of the GUMBOS, $[C_6mim][Eu(tta)_4]$ and Derived Nanoparticles

2.4.1 Absorbance Measurements of GUMBOS and NanoGUMBOS

Absorbance properties were studied for the bulk GUMBOS dissolved in ethanol, while the nanoGUMBOS studied involved suspensions in deionized water (18.2 MΩ). All absorbance measurements were performed in 1 cm path length quartz cuvette, with a scan rate of 0.17 nm s^{-1} at 1 nm slit width using a Shimadzu UV-3101PC UV-Vis-NIR scanning spectrophotometer. Due to low molar absorptivity of the europium (III) (Figure 2.5), the absorption spectrum of the GUMBOS was predominately from the β-diketonate complex. A broader absorbance peak was observed for the nanoGUMBOS suspension as compared to the dissolved GUMBOS (Figure 2.6). Another observed absorbance shoulder of nanoGUMBOS was a slight emerging peak at 290 nm. This peak is due to the imidazolium cation and the minute impurities from the starting material.[33] This emergence of $[C_6mim]$ cation absorbance peak indicates that the imidazolium plays an important role within the morphology of the nanoGUMBOS. This role is further explored in the subsequent sections.

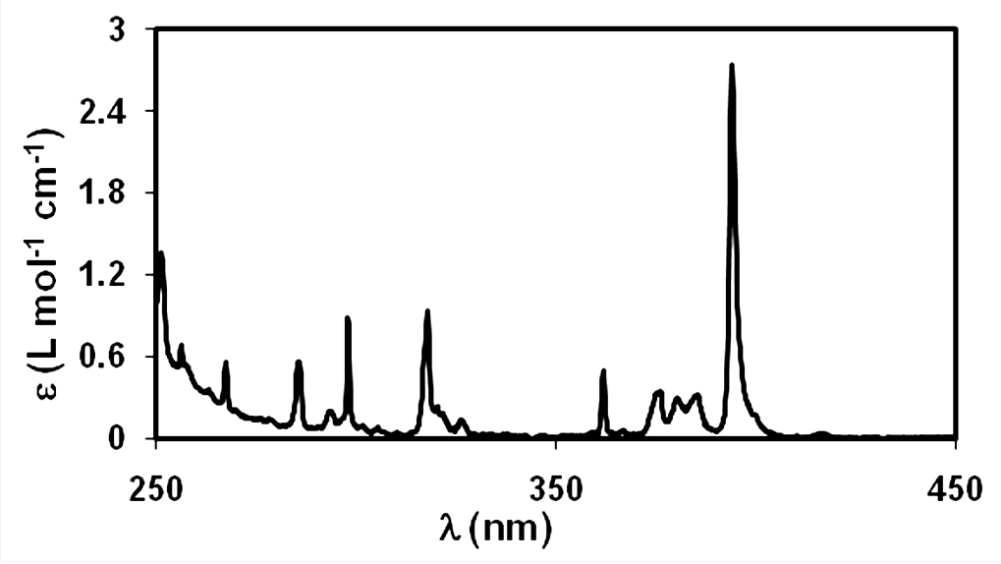


Figure 2.5 Absorption of 0.1 M $EuCl_3$ dissolved in water.

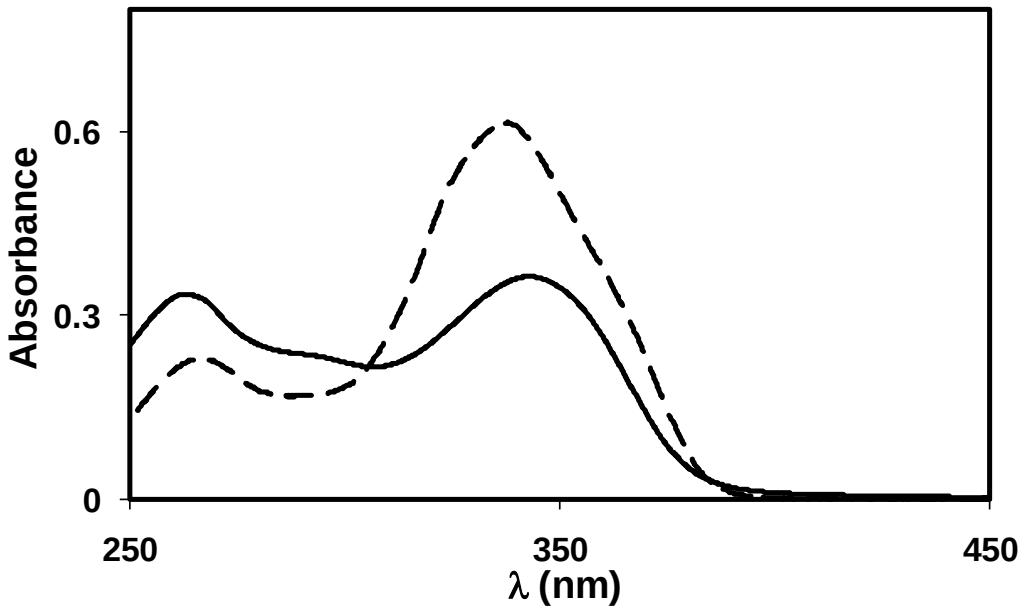


Figure 2.6 Absorbance spectra of the aqueous suspension of nanoGUMBOS (solid line) and a 0.8 μM ethanol solution of GUMBOS (dashed line).

2.4.2 Luminescence Measurements of GUMBOS and NanoGUMBOS

Luminescence measurements were performed on both the nanoparticle aqueous suspension and bulk material dissolved in ethanol using orthogonal instrument geometry and a 1 cm path length quartz cuvette. The GUMBOS and nanoGUMBOS emission intensities were monitored with the excitation and emission slit widths set to 5 nm using a SPEX Fluorolog-3 Jobin Yvon spectrophotometer. An excitation-emission matrix (EEM) was collected and a contour luminescence map was plotted for both the dissolved GUMBOS and the suspended nanoparticles (Figure 2.7). The EEM contour maps were collected by exciting the samples using previously mentioned slit widths at every 5 nm and emission was collected in 2.5 nm increments. Single emission spectra were collected by exciting at every 1 nm and recording emission at every nanometer. This luminescence is associated with europium's most intense transition ($^5D_0 \rightarrow {}^7F_2$) at 613 nm when excited at the complexes' excitation apex of 340 nm. The most immediately observed difference in the nanoGUMBOS emission spectrum was the appearance of a broad

peak at 420 nm. This emission phenomenon was visible in the nanoparticle suspension and also when $[C_6mim][Eu(tta)_4]$ was dissolved in $[C_6mim][Tf_2N]$ as explained later (Figure 2.8). In contrast, $[C_6mim][Eu(tta)_4]$ dissolved in ethanol and other organic solvents did not have a noticeable emission peak at 420 nm. The europium (III) characteristic emission peaks at 596 ($^5D_0 \rightarrow {}^7F_1$) and 613 nm ($^5D_0 \rightarrow {}^7F_2$) were however presented in all dissolved and particle suspension samples.

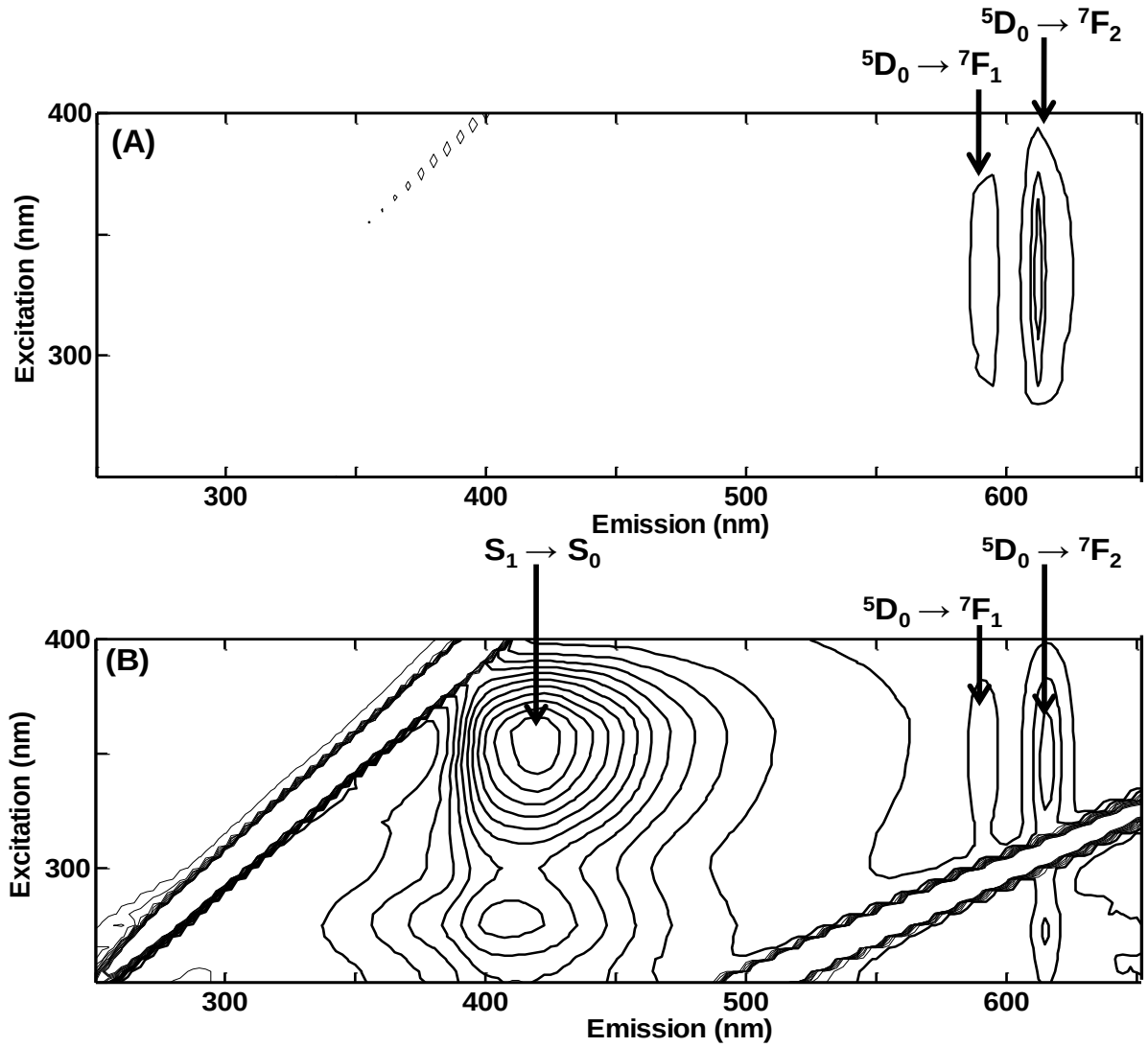


Figure 2.7 (A) Excitation-Emission Matrix (EEM) of (A) 0.8 µM GUMBOS dissolved in ethanol and (B) nanoGUMBOS suspension in water. Emissions between 250-400 nm and 500-650 are due to second-order scattering.

2.4.2.1 Imidazolium Fluorescence Influence

Further studies were performed to characterize the emission profile of the nanoGUMBOS, including the intense fluorescence spectral phenomenon observed at 420 nm and the europium (III) emission peaks. The emission peak at 420 nm could be thought to originate from uncommon luminescence of europium (III) at the $^5D_3 \rightarrow {}^7F_1$ transition, light scattering from the particles, or the spin-favored 5*d*-4*f* transition of europium (II).[1, 34-35] However, since ionic liquids are not generally known to be reducing solvents and the energy required for the 5*d*-4*f* transition of europium (II) is greater,[16] it was concluded and supported by XPS analysis that europium (III) was the predominant species in all samples (Figure 2.3). Therefore, the emission at 420 nm was found to result from fluorescence of the cationic species, [C_6mim].[36] Thus, the excitation of the nanoGUMBOS accentuates emission from europium (III) and imidazolium cation (Figure 2.8). It can be further supported from Figure 2.8B that the broad 420 nm emission derives from the imidazolium cation. Figure 2.8C is a depiction of the GUMBOS dissolved in an ionic liquid that has the identical cation species. The overexpression of imidazolium emerges in the emission spectrum unlike in Figure 2.8A which has a 1:1 mole ratio of imidazolium to europium (III).

Dissolution of the GUMBOS (0.8 µM) into liquid [C_6mim][Tf_2N] also produced the imidazolium 420 nm emission peak in addition to europium (III) luminescence at 613 nm as is shown in Figure 2.8C. The normalized imidazole and europium (III) luminescence peaks reveal close overlap with the previously described emission profiles (Figure 2.9).[37] The nanoGUMBOS having an abnormal reduction in lanthanide emission and increased imidazolium fluorescence suggests a quenching behavior.[38-39] This behavior can be explained through the formation of an organization of imidazolium cations surrounding the lanthanide anion, as suggested by

Chaumont *et al*.[40-41] The proposed reasoning of an assembly of imidazoles surrounding the anion would overwhelmingly quench the luminescence released by europium (III) as supported by the emission spectrum of nanoGUMBOS. The dissolved GUMBOS in ethanol lack the formation of such a quenching opportunity as ions are randomly flowing in solution; thereby, the europium (III) luminescence quenches the [C_6mim] fluorescence via collisions. As shown with the ionic liquid solvent in Figure 2.8C, the addition of excess [C_6mim] enhances the 420 nm fluorescence.

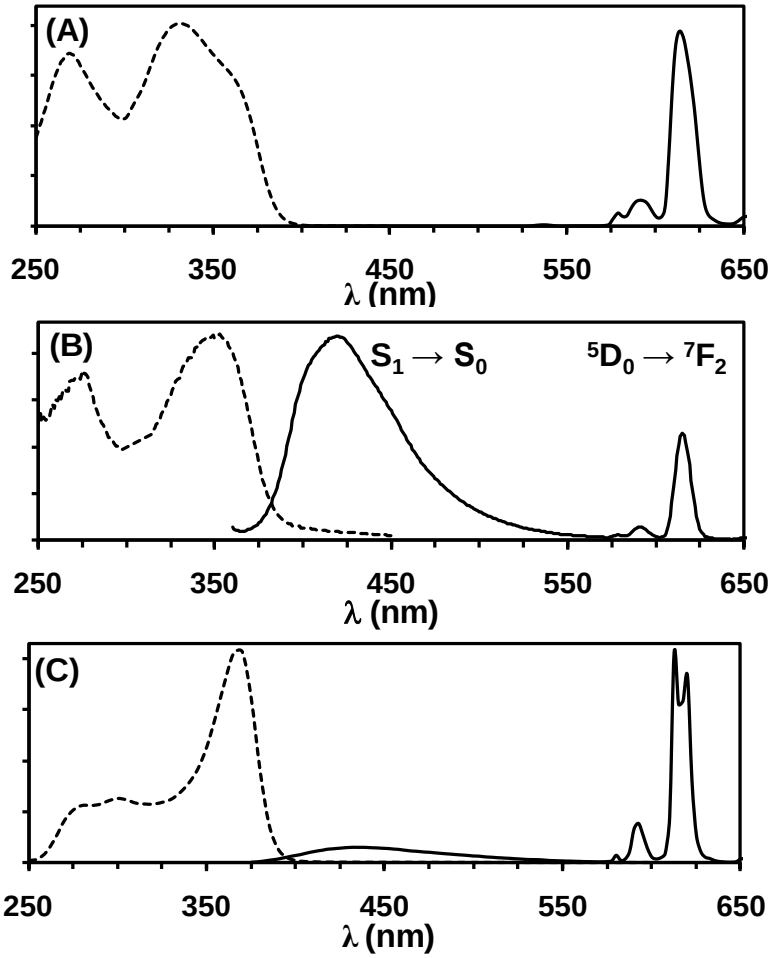


Figure 2.8 Excitation (340 nm, dashed line) and emission (613 nm, solid line) spectra of GUMBOS and nanoGUMBOS. (A) 0.8 μM GUMBOS dissolved in ethanol, (B) nanoGUMBOS suspension in water, and (C) 0.8 μM GUMBOS dissolved in liquid [C_6mim][Tf_2N].

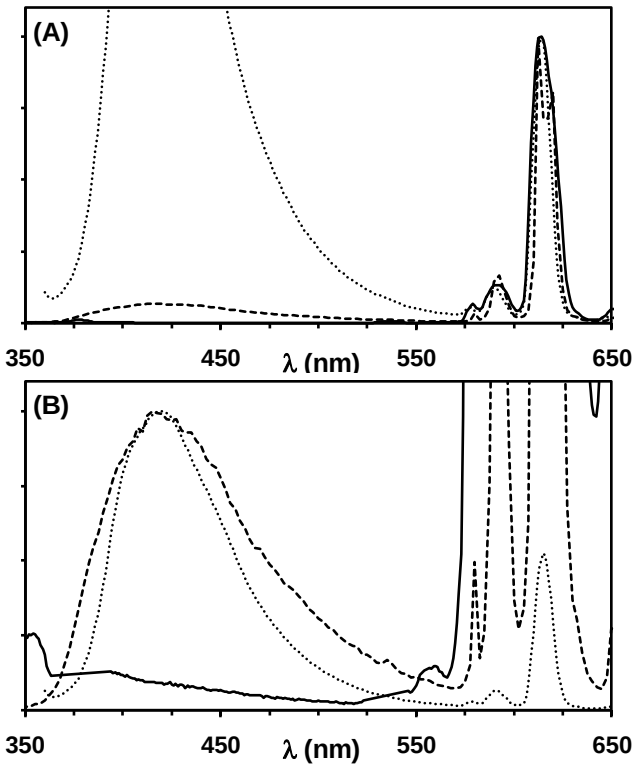


Figure 2.9 Normalized emission spectra of GUMBOS dissolved in ethanol (solid) and $[C_6mim][Tf_2N]$ (dash), and nanoGUMBOS in water (dot) while focusing on the emissions directly from (A) $[C_6mim]$ and (B) europium (III) when excited at 340 nm. (Note: The ethanol Raman peaks were removed for clarity.)

2.4.2.2 Förster Resonance Energy Transfer

The enhanced luminescence of europium (III) in the GUMBOS and nanoGUMBOS is attributed to ligand-to-metal charge transfer from the β-diketone and FRET from the $[C_6mim]$ to europium (III) complex.[36, 42] FRET can be examined by monitoring the emission of the GUMBOS and the nanoGUMBOS in the presence and absence of energy transfer. Since $[C_6mim]$ has considerable absorbance at 340 nm, while the absorbance of europium (III) is negligible at this wavelength, it can be suggested that excitation of the GUMBOS and nanoGUMBOS at 340 nm will selectively excite the $[C_6mim]$. However, exciting at 395 nm will selectively excite the europium (III) since this is its absorption maxima, but an absorption mimima for $[C_6mim]$. Hence, it can be considered that excitation of the GUMBOS and the

nanoGUMBOS at 340 nm will lead to energy transfer from [C_6mim] to europium (III) and enhancement in europium (III) luminescence, which is weakly observed for excitation at 395 nm. Figure 2.10 shows the luminescence of the GUMBOS and nanoGUMBOS in the presence and absence of energy transfer. It was observed that the J(λ) and E values are much higher in organic solvent as compared to water (Table 2.2).[2] This supports our observation of approximately 66.8 times enhancement in europium (III) luminescence intensity of the GUMBOS in ethanol as compared to 7.46 times enhancement in nanoGUMBOS suspended in water. Since β-diketone is nearly non-fluorescent in the studied solvents, FRET from β-diketone is considered to be negligible. The β-diketone participates in ligand-to-metal charge-transfer when enhancing europium (III) luminescence.[42]

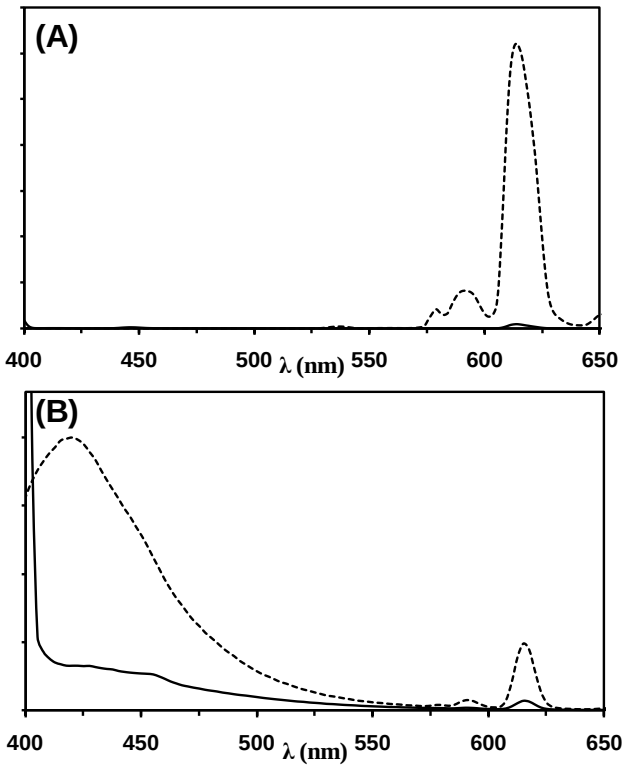


Figure 2.10 Energy transfer was observed from the [C_6mim] to the europium (III) as dissolved GUMBOS in ethanol (A) and suspended nanoGUMBOS in water (B) when excited at the absorption maxima (340 nm, dashed line) and absorption minima (395 nm, bold line) with slit widths at 5 nm.

Differences in emission intensity observed between the dissolved species and suspended nanoparticles are a resulted from water as a static quencher. The oxygen atom in water forms a complex with the formally luminescent compound rendering the compound nonluminescent.[43-44] Figure 2.7 shows an EEM spectrum of the nanoGUMBOS, revealing a slight red shift of the europium electric dipole peak from 613 nm to 615 nm ($^5D_0 \rightarrow {}^7F_2$). In contrast, the magnetic dipole emission peak intensity increased, with a solvatochromic shift from 596 nm to 591 nm.[45] The magnetic dipole transition of $^5D_0 \rightarrow {}^7F_1$, gave an 8% relative difference in emission intensity from the electric dipole transition dipole peak as a nanoparticle. Likewise, the magnetic dipole peak exhibited a relative emission difference of 18% as compared to the electric dipole emission peak of the dissolved species. Due to molecular aggregation into solid state particles, the electric dipole emission intensity peak decreased in intensity from the dissolved GUMBOS because of its sensitivity to the environment.[36, 46] The difference in intensities for the magnetic and electric dipole transitions explains the spectral characteristic sensitivity to the particles' environment.

2.4.2.3 Photostability and Lifetime Decay

When dissolved in organic solvents, the β-diketonate ligand was not photostable, requiring the spectral studies to be conducted directly. Nockemann *et al.* reported that the chelated-ligand retained 80% of its photostability over 10 days of constant daylight after dissolution in acetonitrile.[28, 47] The radiative lifetime decay times for the GUMBOS are relatively similar to other lanthanide luminescent lifetime decay times (micro- to millisecond timeframe) and have an exponential lifetime decay profile (Figure 2.11).[48] These studies were performed using a Fluoromax 4 with a Time Correlated Single Photon Counter, and excited through a sample compartment adapter at 340 and 390 nm for a pulsed nanoLED (800 ps at a rate of 1 MHz) for fast lifetimes (i.e. 430 nm) and spectralLED for long lifetimes (613 nm), respectively.

When dissolved in ethanol, the GUMBOS yielded slightly longer luminescent lifetime decay at the europium (III) emission (613 nm) relative to the nanoGUMBOS suspension in water (61.0 and 47.7 μs, respectively). In addition, there was not a recordable fluorescent lifetime decay for the suggested imidazolium fluorescence (420 nm) when dissolved in ethanol. Imidazolium fluorescence has been found to have a relatively short lifetime, i.e. shorter than 800 ps.[49] However, the imidazolium in the nanoGUMBOS had a lifetime decay of 1.75 ns. The changes in lifetime decay are directly proportional to the compounds relative emission intensities.

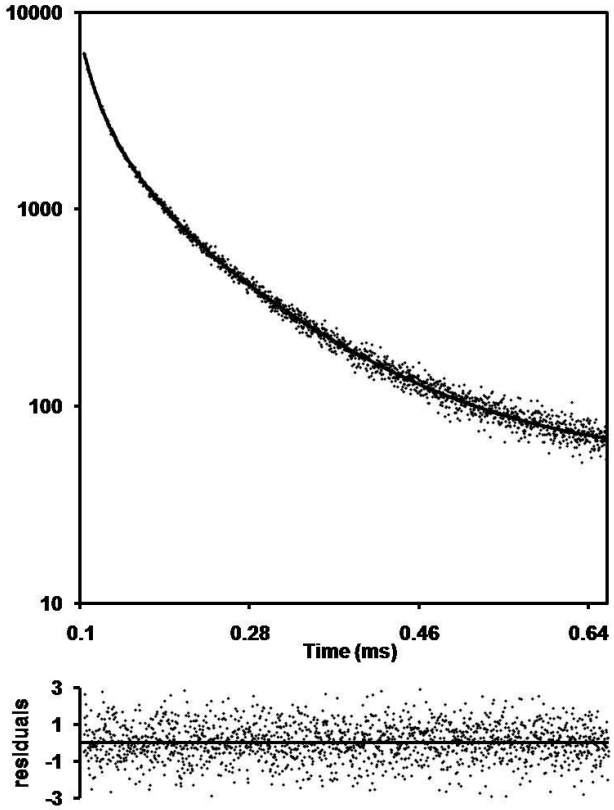


Figure 2.11 Time-domain europium (III) emission decay time of aerosolized nanoparticles, $[C_6mim][Eu(tta)_4]$, resuspended in water.

In comparing of the dissolved GUMBOS and nanoGUMBOS emission spectra, it can be concluded in parallel that with the emergence of $[C_6mim]$ fluorescence, a detectable lifetime was recorded. In addition, europium (III) luminescence decreases relative to that of the counter ion emission, leading to a decrease in lifetime decay. The increase in lifetime for the imidazole in

nanoGUMBOS is believed to be due to a reduction of collisional quenching and multiphonon relaxation onto the more relaxed fluorophore.[50] In contrast, the dissolved GUMBOS experience greater collisional quenching which supports the reasoning for a lower fluorescence obtained by the [C_6mim] cation as a dissolved species. Thereby, the decrease in luminescence suggests an aggregation of imidazolium cations around the anion in the morphology of the nanoparticle.

2.5 Conclusion

The formation, uniformity, and optical properties of [C_6mim][Eu(tta)$_4$] nano/GUMBOS has been thoroughly investigated. The increased surface area of the 39.5 ± 8.4 nm nanoGUMBOS and outer arrangement of the imidazolium cation afforded photoluminescence from cationic and anionic components. The imidazolium fluorescence was observed to be more intense than the europium (III) luminescence in the nanostate supporting Chaumont *et al.* computational theory of cations surrounding an anion with a lanthanide center. The cation fluorescence was due to a molecular outer arrangement within the nanoGUMBOS when producing an emission peak at 420 nm. These nanoGUMBOS emerge as promising candidates for sensory, optical, and photovoltaic applications.

2.6 References

1. Liu, G.; Chen, X. Spectrocopic Properties of Lanthanides in Nanomaterials. In *Handbook on the Physics and Chemistry of Rare Earths: Optical Spectroscopy*, Gschneidner, K. A.; Bünzli, J.-C. G.; Pecharsky, V. K., Eds. North-Holland: Amsterdam, 2007; Vol. 37, pp 99 - 170.

2. Tran, C. D.; Zhang, W. Luminescence Detection of Rare-Earth Ions by Energy Transfer from Counteranion to Crown Ether-Lanthanide Ion Complexes. *Anal. Chem.* **1990,** *62*, 835-840.

3. Alpturk, O.; Rusin, O.; Fakayode, S. O.; Wang, W. H.; Escobedo, J. O.; Warner, I. M.; Crowe, W. E.; Kral, V.; Pruet, J. M.; Strongin, R. M. Lanthanide complexes as fluorescent indicators for neutral sugars and cancer biomarkers. *Proc. Natl. Acad. Sci. USA* **2006,** *103 (26)*, 9756-9760.

4. Mwalupindi, A. G.; Ndou, T. T.; Warner, I. M. Characterization of Select Organic Analytes in Reverse Micelles Using Lanthanide Counterions as Acceptors. *Anal. Chem.* **1992,** *64 (17)*, 1840-1844.

5. Mwalupindi, A. G.; Agbaria, R. A.; Warner, I. M. Synthesis and Characterization of the Surfactant Terbium 3-[[1,2-Bis-[[(2-Ethylhexyl)Oxy]Carbonyl]Ethyl]Thio]Succinate as a Reagent for Determining Organic Analytes. *Appl. Spectrosc.* **1994,** *48 (9)*, 1132-1137.

6. Baek, N. S.; Kim, Y. H.; Eom, Y. K.; Oh, J. H.; Kim, H. K.; Aebischer, A.; Gumy, F.; Chauvin, A. S.; Bünzli, J.-C. G. Sensitized near-IR luminescence of lanthanide complexes based on push-pull diketone derivatives. *Dalton. Trans.* **2010,** *39 (6)*, 1532-1538.

7. Venkatramu, V.; Giarola, M.; Mariotto, G.; Enzo, S.; Polizzi, S.; Jayasankar, C. K.; Piccinelli, F.; Bettinelli, M.; Speghini, A. Nanocrystalline lanthanide-doped $Lu_3Ga_5O_{12}$ garnets: interesting materials for light-emitting devices. *Nanotechnology* **2010,** *21 (17)*, 175703.

8. He, M.; Huang, P.; Zhang, C. L.; Hu, H. Y.; Bao, C. C.; Gao, G.; He, R.; Cui, D. X. Dual Phase-Controlled Synthesis of Uniform Lanthanide-Doped NaGdF4 Upconversion Nanocrystals Via an OA/Ionic Liquid Two-Phase System for In Vivo Dual-Modality Imaging. *Adv. Funct. Mater.* **2011,** *21 (23)*, 4470-4477.

9. Li, M.; Ganea, G. M.; Lu, C. F.; De Rooy, S. L.; El-Zahab, B.; Fernand, V. E.; Jin, R. Y.; Aggarwal, S.; Warner, I. M. Lipophilic Phosphonium-Lanthanide Compounds with Magnetic, Luminescent, and Tumor Targeting Properties. *J. Inorg. Biochem.* **2012,** *107 (1)*, 40-46.

10. Feng, J.; Song, S. Y.; Deng, R. P.; Fan, W. Q.; Zhang, H. J. Novel Multifunctional Nanocomposites: Magnetic Mesoporous Silica Nanospheres Covalently Bonded with Near-Infrared Luminescent Lanthanide Complexes. *Langmuir* **2010,** *26 (5)*, 3596-3600.

11. Mezyk, J.; Di Nuzzo, D.; Mech, A.; Tubino, R.; Meinardi, F. Exciton-exciton annihilation in organic lanthanide complexes. *J. Chem. Phys.* **2010,** *132 (2)*, 024504.

12. Ye, Z. Q.; Tan, M. Q.; Wang, G. L.; Yuan, J. L. Preparation, characterization, and time-resolved fluorometric application of silica-coated terbium(III) fluorescent nanoparticles. *Anal. Chem.* **2004,** *76 (3)*, 513-518.

13. Escribano, P.; Julian-Lopez, B.; Planelles-Arago, J.; Cordoncillo, E.; Viana, B.; Sanchez, C. Photonic and nanobiophotonic properties of luminescent lanthanide-doped hybrid organic- inorganic materials. *J. Mater. Chem.* **2008,** *18 (1)*, 23-40.

14. Wang, F.; Liu, X. G. Recent advances in the chemistry of lanthanide-doped upconversion nanocrystals. *Chem. Soc. Rev.* **2009,** *38 (4)*, 976-989.

15. Bottrill, M.; Nicholas, L. K.; Long, N. J. Lanthanides in magnetic resonance imaging. *Chem. Soc. Rev.* **2006,** *35 (6)*, 557-571.

16. Bünzli, J.-C. G. Benefiting from the unique properties of lanthanide ions. *Acc. Chem. Res.* **2006,** *39 (1)*, 53-61.

17. Daiguebonne, C.; Kerbellec, N.; Guillou, O.; Bünzli, J.-C. G.; Gumy, F.; Catala, L.; Mallah, T.; Audebrand, N.; Gerault, Y.; Bernot, K.; Calvez, G. Structural and luminescent properties of micro- and nanosized particles of lanthanide terephthalate coordination polymers. *Inorg. Chem.* **2008,** *47 (9)*, 3700-3708.

18. Tiseanu, C.; Parvulescu, V. I.; Paun, C.; Dobroiu, S. Optical Properties of Nd3+ Doped Ionic Liquid Immobilized on Mesoporous Silica Support. *J. Nanosci. Nanotechno.* **2010,** *10 (4)*, 2921-2925.

19. Lunstroot, K.; Driesen, K.; Nockemann, P.; Viau, L.; Mutin, P. H.; Vioux, A.; Binnemans, K. Ionic liquid as plasticizer for europium(III)-doped luminescent poly(methyl methacrylate) films. *Phys. Chem. Chem. Phys.* **2010,** *12 (8)*, 1879-1885.

20. Tang, S. F.; Mudring, A. V. Terbium beta-Diketonate Based Highly Luminescent Soft Materials. *Eur. J. Inorg. Chem.* **2009,** *(19)*, 2769-2775.

21. Mudring, A. V.; Tang, S. F. Ionic Liquids for Lanthanide and Actinide Chemistry. *Eur. J. Inorg. Chem.* **2010,** *(18)*, 2569-2581.

22. Getsis, A.; Mudring, A. V. Switchable Green and White Luminescence in Terbium-Based Ionic Liquid Crystals. *Eur. J. Inorg. Chem.* **2011,** *(21)*, 3207-3213.

23. Tran, C. D.; Challa, S.; Franko, M. Ionic liquids as an attractive alternative solvent for thermal lens measurements. *Anal. Chem.* **2005,** *77 (22)*, 7442-7447.

24. Tesfai, A.; El-Zahab, B.; Bwambok, D. K.; Baker, G. A.; Fakayode, S. O.; Lowry, M.; Warner, I. M. Controllable formation of ionic liquid micro- and nanoparticles via a melt-emulsion-quench approach. *Nano Lett.* **2008,** *8 (3)*, 897-901.

25. Tesfai, A.; El-Zahab, B.; Kelley, A. T.; Li, M.; Garno, J. C.; Baker, G. A.; Warner, I. M. Magnetic and Nonmagnetic Nanoparticles from a Group of Uniform Materials Based on Organic Salts. *ACS Nano* **2009,** *3 (10)*, 3244-3250.

26. Li, M.; De Rooy, S. L.; Bwambok, D. K.; El-Zahab, B.; DiTusa, J. F.; Warner, I. M. Magnetic chiral ionic liquids derived from amino acids. *Chem. Commun.* **2009,** *(45)*, 6922-6924.

27. Bwambok, D. K.; El-Zahab, B.; Challa, S. K.; Li, M.; Chandler, L.; Baker, G. A.; Warner, I. M. Near-Infrared Fluorescent NanoGUMBOS for Biomedical Imaging. *ACS Nano* **2009,** *3 (12)*, 3854-3860.

28. Nockemann, P.; Beurer, E.; Driesen, K.; Van Deun, R.; Van Hecke, K.; Van Meervelt, L.; Binnemans, K. Photostability of a highly luminescent europium beta-diketonate complex in imidazolium ionic liquids. *Chem. Commun.* **2005,** *(34),* 4354-4356.

29. Verma, H. R. *Atomic and Nuclear Analytical Methods : XRF, Mössbauer, XPS, NAA and Ion-Beam Spectroscopic Techniques*. Springer: Berlin ; New York, 2007; p xiv, 375 p.

30. Zimmermann, T.; Rietdorf, J.; Girod, A.; Georget, V.; Pepperkok, R. Spectral Imaging and Linear Un-Mixing Enables Improved FRET Efficiency with a Novel GFP2-YFP FRET Pair. *FEBS Lett.* **2002,** *531,* 245-249.

31. Clapp, A. R.; Medintz, I. L.; Mauro, J. M.; Fisher, B. R.; Bawendi, M. G.; Mattoussi, H. Fluorescence Resonance Energy Transfer Between Quantum Dot Donors and Dye-Labeled Protein Acceptors. *J. Am. Chem. Soc.* **2004,** *126,* 301-310.

32. Muino, P. L.; Callis, P. R. Solvent Effects on the Fluorescence Quenching of Tryptophan by Amides via Electron Transfer. Experimental and Computational Studies. *J. Phys. Chem. B* **2009,** *113 (9),* 2572-2577.

33. Nockemann, P.; Binnemans, K.; Driesen, K. Purification of Imidazolium Ionic Liquids for Spectroscopic Applications. *Chem. Phys. Lett.* **2005,** *415 (1-3),* 131-136.

34. Lin, H.; Tanabe, S.; Lin, L.; Yang, D. L.; Liu, K.; Wong, W. H.; Yu, J. Y.; Pun, E. Y. B. Infrequent blue and green emission transitions from Eu^{3+} in heavy metal tellurite glasses with low phonon energy. *Phys. Lett. A* **2006,** *358 (5-6),* 474-477.

35. Billard, I.; Moutiers, G.; Labet, A.; El Azzi, A.; Gaillard, C.; Mariet, C.; Lutzenkirchen, K. Stability of divalent europium in an ionic liquid: Spectroscopic investigations in 1-methyl-3-butylimidazolium hexafluorophosphate. *Inorg. Chem.* **2003,** *42 (5),* 1726-1733.

36. Guillet, E.; Imbert, D.; Scopelliti, R.; Bünzli, J.-C. G. Tuning the emission color of europium-containing ionic liquid-crystalline phases. *Chem. Mater.* **2004,** *16 (21),* 4063-4070.

37. Yguerabide, J.; Yguerabide, E. E. Light-scattering submicroscopic particles as highly fluorescent analogs and their use as tracer labels in clinical and biological applications - I. Theory. *Anal. Biochem.* **1998,** *262 (2),* 137-156.

38. Cheng, P. P. H.; Silvester, D.; Wang, G. L.; Kalyuzhny, G.; Douglas, A.; Murray, R. W. Dynamic and static quenching of fluorescence by 1-4 nm diameter gold monolayer-protected clusters. *J. Phys. Chem. B* **2006,** *110 (10),* 4637-4644.

39. Landes, C. F.; Braun, M.; El-Sayed, M. A. On the nanoparticle to molecular size transition: Fluorescence quenching studies. *J. Phys. Chem. B* **2001,** *105 (43),* 10554-10558.

40. Chaumont, A.; Wipff, G. Solvation of M^{3+} lanthanide cations in room-temperature ionic liquids. A molecular dynamics investigation. *Phys. Chem. Chem. Phys.* **2003,** *5 (16)*, 3481-3488.

41. Chaumont, A.; Wipff, G. Solvation of fluoro and mixed fluoro/chloro complexes of Eu^{III} in the [BMI][PF_6] room temperature ionic liquid. A theoretical study. *Phys. Chem. Chem. Phys.* **2005,** *7 (9)*, 1926-1932.

42. Yu, G.; Liu, Y.; Wu, X.; Zhu, D.; Li, H.; Jin, L.; Wang, M. Soluble Europium Complexes for Light-Emitting Diodes. *Chem. Mater.* **2000,** *12*, 2537-2541.

43. Haas, Y.; Stein, G. Pathways of Radiative and Radiationless Transitions in Europium(III) Solutions: the Role of High Energy Vibrations. *J. Phys. Chem.* **1971,** *75 (24)*, 3677 - 3681.

44. Billard, I.; Mekki, S.; Gaillard, C.; Hesemann, P.; Moutiers, G.; Mariet, C.; Labet, A.; Bünzli, J.-C. G. Eu^{III} luminescence in a hygroscopic ionic liquid: effect of water and evidence for a complexation process. *Eur. J. Inorg. Chem.* **2004,** *2004 (6)*, 1190-1197.

45. Fujihara, S.; Tokumo, K. Multiband orange-red luminescence of Eu^{3+} ions based on the pyrochlore-structured host crystal. *Chem. Mater.* **2005,** *17 (22)*, 5587-5593.

46. Zhang, C.; Chen, J.; Zhou, Y. C.; Li, D. Q. Ionic liquid-based "all-in-one" synthesis and photoluminescence properties of lanthanide fluorides. *J. Phys. Chem. C* **2008,** *112 (27)*, 10083-10088.

47. Lunstroot, K.; Nockemann, P.; Van Hecke, K.; Van Meervelt, L.; Görller-Walrand, C.; Binnemans, K.; Driesen, K. Visible and Near-Infrared Emission by Samarium(III)-Containing Ionic Liquid Mixtures. *Inorg. Chem.* **2009,** *48 (7)*, 3018-3026.

48. Moore, E. G.; Samuel, A. P. S.; Raymond, K. N. From Antenna to Assay: Lessons Learned in Lanthanide Luminescence. *Acc. Chem. Res.* **2009,** *42 (4)*, 542-552.

49. Paul, A.; Mandal, P. K.; Samanta, A. On the optical properties of the imidazolium ionic liquids. *J. Phys. Chem. B* **2005,** *109 (18)*, 9148-9153.

50. Lakowicz, J. R. *Principles of Fluorescence Spectroscopy*. 3rd ed.; Springer: 2006; p 954.

Chapter 3. Photothermal Response of Near-Infrared NanoGUMBOS

3.1 Introduction

Dual properties from a single material have been achieved with tunable ionic materials known as GUMBOS (***G***roup of ***U***niform ***M***aterials ***B***ased on ***O***rganic ***S***alts). These GUMBOS have been shown to afford concerted properties such as fluorescence and magnetism,[1] chirality and magnetism,[2] chirality and fluorescence.[3] GUMBOS can also be specifically designed to achieve desired properties through a simple exchange of the appropriate counterions. In addition to tailoring GUMBOS with specific functional properties, other physical and chemical properties (e.g. viscosity, solubility, absorption and emission wavelengths, and melting point) can also be altered by careful selection of the constituent ions.[1]

Nanoparticles derived from GUMBOS, coined nanoGUMBOS, have been successfully synthesized by employing various methods including melt-emulsion-quench,[4] reverse-micelle,[1] reprecipitation,[5] and aerosolization.[6] Each of these methods has comparative advantages and limitations that include particle size range, particle monodispersity, and yield. Bulk GUMBOS often possess somewhat different spectral properties than the nanoscale equivalent (nanoGUMBOS).[6] Previously, Bwambok *et al*., utilized a reprecipitation approach to synthesize near-infrared (NIR) nanoGUMBOS for biomedical imaging inside cells.[7]

The NIR spectrum is of great interest for biomedical applications since the absorbance of skin tissue is low and the optical penetration depth is near maximum in this region.[8] Therefore, various studies have been conducted to investigate NIR compounds as biomedical fluorescent probes,[9] solid-state and dye lasers,[10] and for thermal energy generation.[11] Biomedical probes have been employed to visually locate an area of interest by producing fluorescence upon excitation.[12-14] In addition to a radiative transition, they also produce non-radiative transitions

which release energy in the form of heat. Photo-responsive materials that produce heat have recently gained interest due to their clinical applications and promising activity in destroying cancer through hyperthermia.[15]

Materials capable of converting photons efficiently to heat upon excitation by use of a near IR laser are of great interest for developing *in vivo* hyperthermic therapies.[16] Light-responsive organized media nanoparticles,[17] functionalized nanotubes,[18] gold nanoshells,[19] or polymer nanogels[20] are some of the nanomaterials previously utilized to achieve controlled cell destruction using hyperthermia. The aforementioned nanomaterials were photothermally activated using near infrared lasers in the range of 650 – 1064 nm. The organized media used in this study was developed from a porphysome supramolecular self-assembly which formed 100 nm nanovesicles capable of reaching temperatures of up to 60 °C in tissue within a minute of irradiation at 658 nm.[17] Since these nanovesicles are designed from phospholipid-porphyrin self-assembled conjugates, they are considered to be biodegradable. Other nanomaterials used external agents to increase biocompatibility; for example, carbon nanotubes have been functionalized with DNA, and gold composite nanoparticles have been coated with polyethylene glycol.[18-19] Gold nanomaterials have been observed to reach substantial photothermal temperatures of up to 60 °C in solution or tissue through decay of localized surface plasmon resonance modes.[11, 19] Unfortunately, these nanomaterials often require extensive syntheses to improve biocompatibility for use in applications such as cancer therapy.

Herein, we report a class of NIR nanoGUMBOS which were synthesized using a facile two step procedure with photothermal cations and biocompatibile anions[21-24] resulting in a stable nanoformulation.[4] Nanoparticles were derived from four NIR GUMBOS obtained using a combination of two cationic NIR dyes and two biocompatible anions and their physical, spectral,

and hyperthermal characteristics were investigated. Examination of the results suggests a possible use in cancer therapy. These studies also reveal altered morphological and photothermal characteristics in acidic, neutral, and basic environments which yield information regarding the true fate of the nanoparticles in the acidic environment of the tumors.

3.2 Experimental

3.2.1 Materials

Sodium ascorbate, sodium deoxycholate, 1-Butyl-2-[2-[3-[(1-butyl-6-chlorobenz[cd]indol-2(1*H*)-ylidene)ethylidene]-2-chloro-1-cyclohexen-1-yl]ethenyl]-6-chlorobenz[cd]indolium tetrafluoroborate ([1048][BF_4]) and 4-[2-[2-Chloro-3-[(2,6-diphenyl-4*H*-thiopyran-4-ylidene)ethylidene]-1-cyclohexen-1-yl]ethenyl]-2,6-diphenylthiopyrylium tetrafluoroborate ([1061][BF_4]), sodium hydroxide (NaOH), hydrochloric acid (HCl), dichloromethane (DCM), and acetone were purchased from Sigma-Aldrich (St. Louis, MO) and were used as received. Triply deionized water (18.2 MΩ**)** was obtained using an Elga Genetic Ultra-Pure water polishing system obtained from US Filter (Lowell, MA, USA).

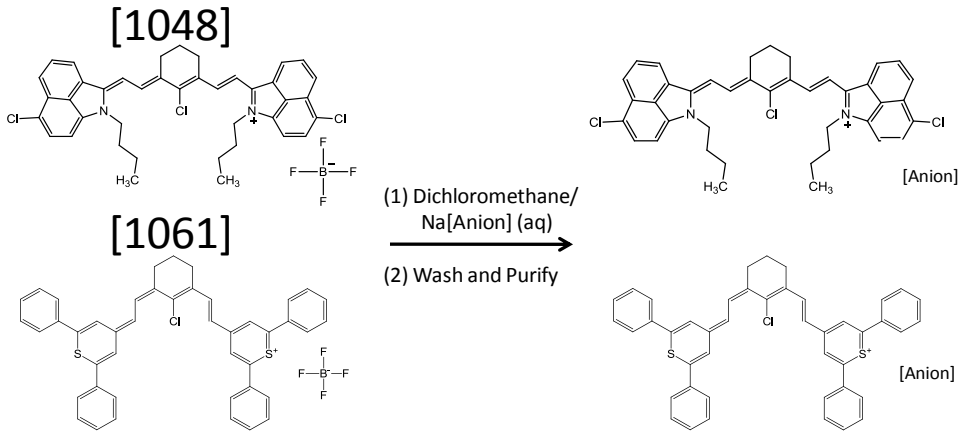
3.2.2 Characterization

The infrared absorption measurements of GUMBOS and nanoGUMBOS were performed using a Lambda 750 UV-Vis-NIR Spectrophotometer (Perkin-Elmer, Waltham, MA, USA) using a 1 cm pathlength quartz cuvette. Structural characterizations of these GUMBOS were elucidated by use of the following instrumentation: ^{1}H NMR Brüker DPX-400 (400 MHz) and ^{19}F NMR Brüker DPX-250 (250 MHz). The sizes and images of these nanoGUMBOS were acquired by use of a JEOL JEM-1011 (Peabody, MA, USA) transmission electron microscope. The zeta potentials of the nanoGUMBOS were obtained using a DTS1061 capillary cell in a Zetasizer Nanoseries Nano ZS (Malvern Instruments, Worcestershire, UK) instrument. The

melting points for these GUMBOS were measured in triplicate using a Digimelt MPA160 melting point apparatus (Stanford Research Systems Inc., Sunnyvale, CA, USA). The heat capacities (C_p) for the GUMBOS were measured by a modulated differential scanning calorimeter, model: DSC2920, (TA Instruments, New Castle, DE, USA) in hermetic aluminum pans (p/n: V0804805, Thermal Support, Lawrenceville, GA, USA).

3.2.3 Synthesis of GUMBOS and NanoGUMBOS

Scheme 3.1 Metathesis synthesis for the [1048] and [1061] GUMBOS were performed by an anion exchange method.



GUMBOS used in this study were synthesized via an anion exchange method (Scheme 3.1). Cationic dyes were individually dissolved in dichloromethane and mixed with aqueous anionic precursor salts in a 1:1.1 (mol:mol) ratio. These materials were then allowed to stir for two days while wrapped in aluminum foil to avoid photobleaching. These newly synthesized GUMBOS were washed three times with water, followed by decanting the water, and removing the solvent by use of a rotovap. NanoGUMBOS were synthesized by use of a reprecipitation method employing a High Intensity Ultrasonic Processor VC 750 (Sonics & Materials Inc., Newton, CT). The aqueous suspension was adjusted to variable pH values (2.0, 5.0, 7.0, 9.0, and 11.0) using HCl and NaOH prior to the formation of nanoGUMBOS. These GUMBOS were then dissolved in acetone at a concentration of 2 mM with an injection volume of 150 µL into 5 mL of

an aqueous suspension jacketed in ice to minimize overheating for the 10 minutes of continuous probe sonication. Following sonication, the newly formed nanoGUMBOS were allowed to equilibrate under ambient conditions in the dark for five days prior to characterization and further analyses.

3.2.4 Laser Irradiation

GUMBOS and nanoGUMBOS were irradiated using an infrared (1064 nm) diode-pumped solid state ($Nd:YVO_4$) laser (Lasermate Group Inc., Pomona, CA, USA) at variable power intensities for five minutes and measured by use of a Thermovision A40 thermal imaging camera and the ThermoCAM™ Researcher 2.8 SR-1 software (FLIR Systems Inc., Boston, MA, USA). Bulk GUMBOS were irradiated at the following four power intensities: 250, 500, 750, and 1000 mW. Bulk GUMBOS (4 mg) were placed on a watch glass orthogonal to the thermocamera. The laser was aligned 80° from the sample at a distance of 15 cm**.** The presented angle resulted in a laser spot having a diameter of approximately 2 mm. The power intensity at 250, 500, and 750 mW for the nanoGUMBOS did not yield a substantial increase in temperature; therefore, only 1000 mW power intensity is reported. The nanoGUMBOS photothermal responses were measured in a 1 x 1 cm fluorescence quartz cuvette at a volume of 500 µL.

3.3 Results and Discussion

3.3.1 Characterization of NIR GUMBOS and NanoGUMBOS

Preliminary structural information of the GUMBOS were elucidated by use of ^{1}H and ^{19}F NMR. Use of ^{19}F NMR confirmed a complete anion exchange and successful removal of the starting material, tetrafluoroborate, as indicated by the absence of a fluorine peak. The ^{1}H and ^{19}F NMR spectroscopy data of the four synthesized GUMBOS are provided in Appendix, Figures A3.1 A-F. Fourier Transform Infrared (FTIR) spectroscopy elucidation studies were also

performed to observe the protonation/deprotonation of anions when NIR nanoGUMBOS were synthesized at various pH values (Appendix, Figure A3.2 A-D). The FTIR absorbencies of the nanoGUMBOS were measured in the synthesis medium. The synthesis of nanoGUMBOS at various pH values (i.e. 2.0, 5.0, 7.0, 9.0, and 11.0) resulted in different shapes and sizes as determined by TEM. It was noticed that the nanoGUMBOS synthesized in a medium of pH 2 typically formed nanorods opposed to the nanoGUMBOS synthesized in the other pH media. The zeta potential of the nanoGUMBOS was measured as this is an important factor determining the stability of these colloidal systems. This is because increasing the positive or negative charge of the nanoGUMBOS will result in more stable particles due to enhanced repulsion among the particles,[25] while smaller zeta potentials indicate instability of the suspension leading to the aggregation of the particles.

3.3.1.1 [1048][Deoxycholate]

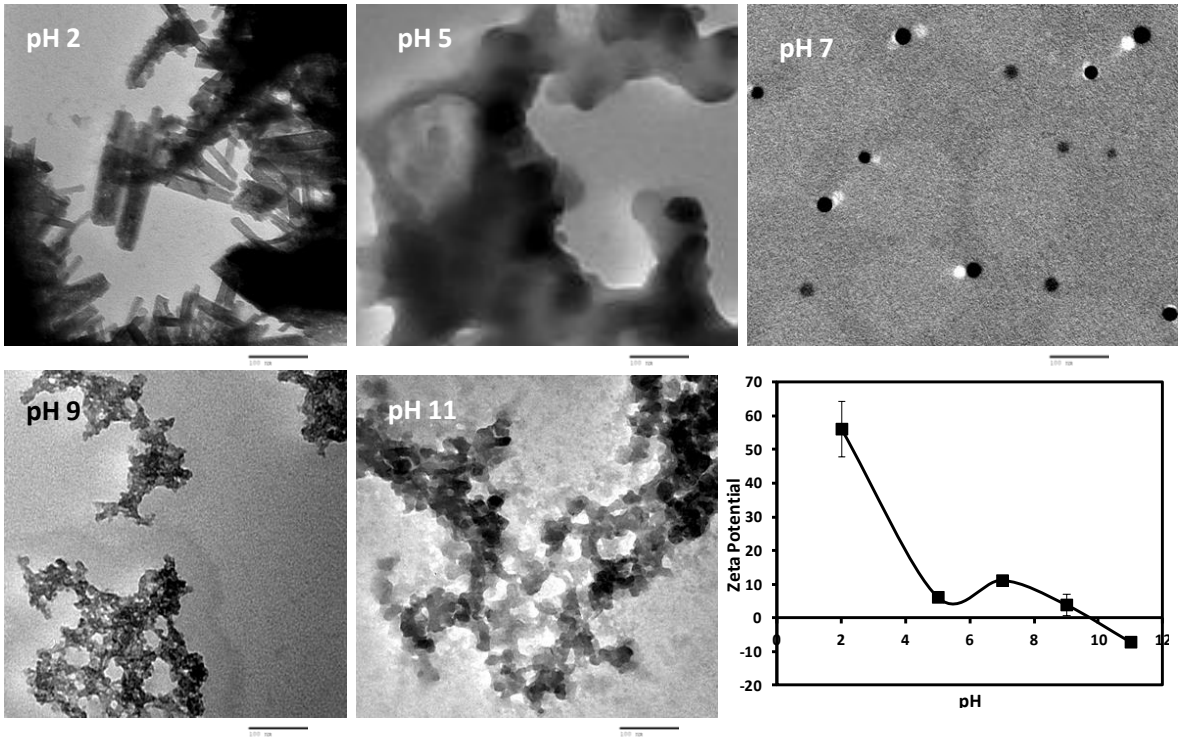
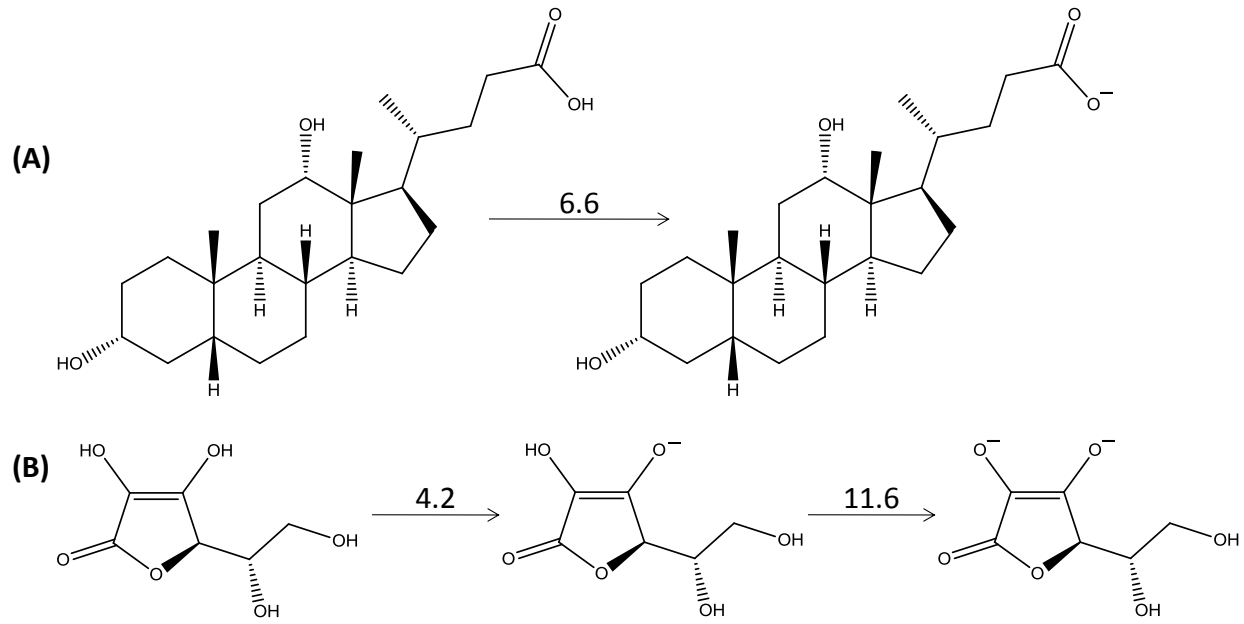


Figure 3.1 Representative TEM images of [1048][Deoxycholate] NIR nanoGUMBOS prepared in different pH media yielded different sizes and shapes (scale bars are 100 nm).

The nanoGUMBOS synthesized in pH 2.0 media resulted in rod-like shapes (Figure 3.1). These precipitated nanorods are believed to be solely composed of the cation, [1048], ionically bound to a chloride anion. It is likely that at a low pH the anions are protonated based on their pKa values (Scheme 3.2).[26] The chloride anion would thermodynamically favor the ionic bond with the cation dyes due to the excessive concentration of the chloride anion creating, [1048][Cl]. The protonated "would-be" anion (i.e. [Deoxycholate]) becomes water soluble, resulting in solely [1048][Cl] precipitating into nanorods. The rods formed at pH 2.0 for the [1048][Cl] nanoGUMBOS were dispersed with a resulting diameter of 23.5 ± 10.4 nm.

Scheme 3.2 The protonation to deprotonation of desired anions (A, Deoxycholate; B, Ascorbate) and their respective pKa help to gain understanding of the nanoGUMBOS structural formation.



The higher pH media that the nanoGUMBOS were synthesized in resulted in spherical-like shapes due to the ionic coordination of the intended anion (i.e. [Deoxycholate]). The nanoGUMBOS synthesized at pH 5.0 strongly aggregated (53.4 ± 7.4 nm) due to the anions pka of 6.6 and low zeta potential of +6.25 mV. Deprotonation of an anion occurs when nanoGUMBOS are synthesized near the pKa of the anion. The deprotonation of the anions

resulted in the formation of spherical shapes rather than rods as seen at pH 2.0. The FTIR studies were observed from the aqueous media to measure the protonation and deprotonation of the anions (Appendix, Figure A3.2A). The [1048][Cl] at pH 2.0 shows the strong –C-OH in-plane bends at 1420 and 1467 cm^{-1} for deoxycholic acid, while at pH 5.0 only one peak at 1427 cm^{-1} corresponding to [Deoxycholate]. The –C(=O)-O- and –C-O- stretches had a difference in intensities between nanoGUMBOS suggesting protonation-deprotonation of the anion in the two different pH media (i.e. pH 2 and 5). When the pH is above the pKa of deoxycholate (i.e. pH 7), the nanoGUMBOS become less aggregated and more stable having a size distribution of 117.9 ± 35.3 nm, and a zeta potential of +11.2 mV. At pH 9.0 and 11.0 the nanoGUMBOS are more aggregated with respective sizes for pH 9 and 11 of 12.7 ± 7.2 nm and 20.7 ± 5.4 nm. The aggregation of nanoGUMBOS synthesized in pH 9.0 and 11.0 media is likely the result of the respective small zeta potentials of +3.98 and -7.07 mV. The FTIR spectra for these nanoGUMBOS do not seem to differ significantly in terms of peak shifts or intensities, indicating little change in molecular structure.

3.3.1.2 [1048][Ascorbate]

The [1048][Ascorbate] nanoGUMBOS formed globular rod-like structures when synthesized in an aqueous medium at pH 2.0 (Figure 3.2). Similar to the aforementioned nanoGUMBOS, [1048][Deoxycholate], it is believed that these rods are entirely composed of [1048][Cl] due to the over abundance of chloride anion in this very acidic environment. These globular structures had an average diameter of 357 ± 38 nm, while the diameters of the rods were 48.5 ± 12.7 nm.

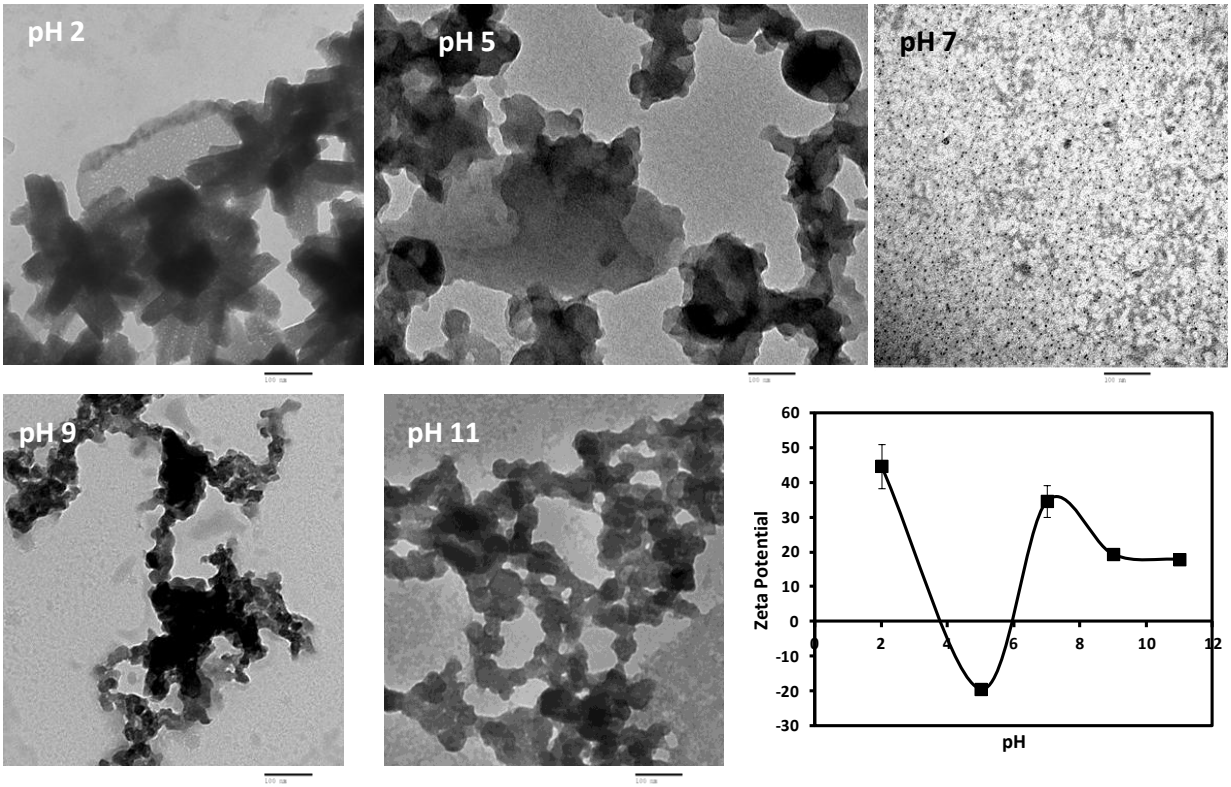


Figure 3.2 TEM images of [1048][Ascorbate] NIR nanoGUMBOS prepared in different pH media yielded different sizes and shapes (scale bars are at 100 nm).

According to the FTIR spectrum the ascorbate anion is completely protonated when the nanoGUMBOS were synthesized in pH 2.0 as indicated by the doublet in-plane C-O-H bend at 1429 and 1460 cm^{-1} (Appendix, Figure A3.2B). When synthesized in an increased pH media (pH 5.0) the absence of the 1460 cm^{-1} bend and a more pronounced 1424 cm^{-1} bend indicated deprotonation of the hydroxyl group, thus allowing the formation of an ionic bond with the [1048] cation. At this pH, aggregation of particles (142 ± 21.4 nm and zeta potential of -19.5 mV) occurs due to their instability in an acidic environment near the pKa of ascorbate 4.2. It was observed that nanoGUMBOS synthesized near the pKa of their anions tend to show more aggregation and less particle stability. The observed phenomenon can be attributed to partial dissociation of the anion due to protonation of the carboxylic groups. This in turn results in an increase in the sole anions hydrophilicity; unlike when the anion is ionically bound to the

intended cation making the molecule hydrophobic. The [1048][Ascorbate] nanoGUMBOS synthesized in pH 7.0 media resulted in monodispersed particles of 49.7 ± 11.3 nm and a zeta potential of +34.7 mV. The monodispersity of the pH 7.0 nanoGUMBOS is well-supported by the high zeta potential, suggesting that these particles have a high positive surface charge and therefore have stable repulsion forces. In basic environments at pH 9.0 and 11.0, the aggregated nanoGUMBOS (27.4 ± 5.4 and 39.0 ± 8.8 nm, respectively) experienced poor stability. These zeta potentials for the pH 9.0 and 11.0 nanoGUMBOS (+19.4 and +17.9 mV, respectively) are in agreement with the particles colloidal instability. The [1048] nanoGUMBOS synthesized in the various pH media had lower net surface charges in pH media 5.0, 9.0, and 11.0 resulting in nanoparticle aggregation (Table 3.1).

Table 3.1 A compiled list of the [1048] nanoGUMBOS spectral and morphological characteristics for [Deoxycholate] and [Ascorbate], respectively, show a trend of aggregation and zeta-potential with an increased pH media. The bold lines represent the divisions of pKa values.

[1048][Deoxycholate] - pKa 6.6						
pH	**Size (nm)**	**Aggregation**	**Zeta Potential (mV)**	**Absorbance (1064 nm)**	**ΔT Irradiation (°C)**	**GUMBOS Photothermal Efficiency %**
2	23.5	No	56.2	0.1469	19.00	19.66
5	53.4	Yes	6.25	0.1849	13.30	
7	117.9	No	11.2	0.1674	18.02	
9	12.7	Yes	3.98	0.2254	19.57	
11	20.7	Yes	-7.07	0.2168	16.08	

[1048][Ascorbate] - pKa 4.2, 11.6						
pH	**Size (nm)**	**Aggregation**	**Zeta Potential (mV)**	**Absorbance (1064 nm)**	**ΔT Irradiation (°C)**	**GUMBOS Photothermal Efficiency %**
2	357	No	44.8	0.1731	18.02	64.39
5	142	Yes	-19.5	0.0583	23.78	
7	49.7	No	34.7	0.0266	20.80	
9	27.4	Yes	19.4	0.0405	20.88	
11	39.0	Yes	17.9	0.0562	21.56	

3.3.1.3 [1061][Deoxycholate]

The [1061][Deoxycholate] nanoGUMBOS, synthesized at pH 2.0 formed globular rod structures similarly to the [1048] nanoGUMBOS at pH 2.0 (Figure 3.3). The average diameters

of these rods are 35.2 ± 13.3 nm that made a cluster of rods (228 ± 49 nm). The zeta potential of the globular structures is high at +43.9 mV and suggests that this is a stable conformation.

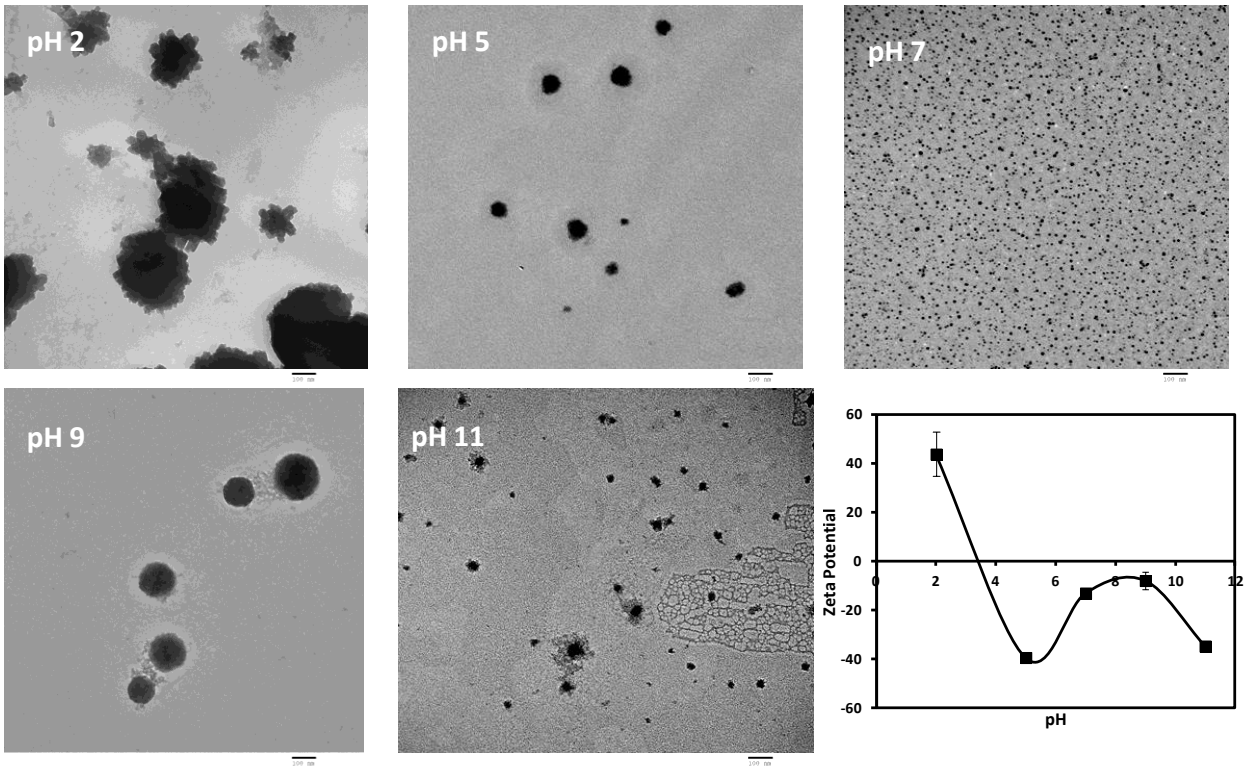


Figure 3.3 The NIR nanoGUMBOS, [1061][Deoxycholate] prepared in different pH media yielded different sizes and shapes (scale bars are at 100 nm).

The FTIR spectra for these nanoGUMBOS synthesized in pH 2.0 and 5.0 showed similar molecular changes as the aforementioned [1048] nanoGUMBOS with [Deoxycholate] anion (Appendix, Figure A3.2C), suggesting [1061][Cl] as the precipitating nanoGUMBOS in pH 2 aqueous medium. For pH values of 5.0, 7.0, 9.0, and 11.0, the respective size distributions for each synthesized nanoGUMBOS are 84.1 ± 21.2, 8.8 ± 1.7, 142.5 ± 40.5, and 55.0 ± 10.3 nm. The nanoGUMBOS synthesized at increased pH values were observed to be monodispersed with very limited aggregation which correlated well with respective zeta potentials of -39.4, -13.0, -7.87, and -34.7 mV at pH 5.0, 7.0, 9.0, and 11.0. The FTIR spectra for the nanoGUMBOS

synthesized in pH 7.0, 9.0, and 11.0 media suggest that the [1061] cation has an ionic bond to the [Deoxycholate] anion (Appendix, Figure A3.2C).

3.3.1.4 [1061][Ascorbate]

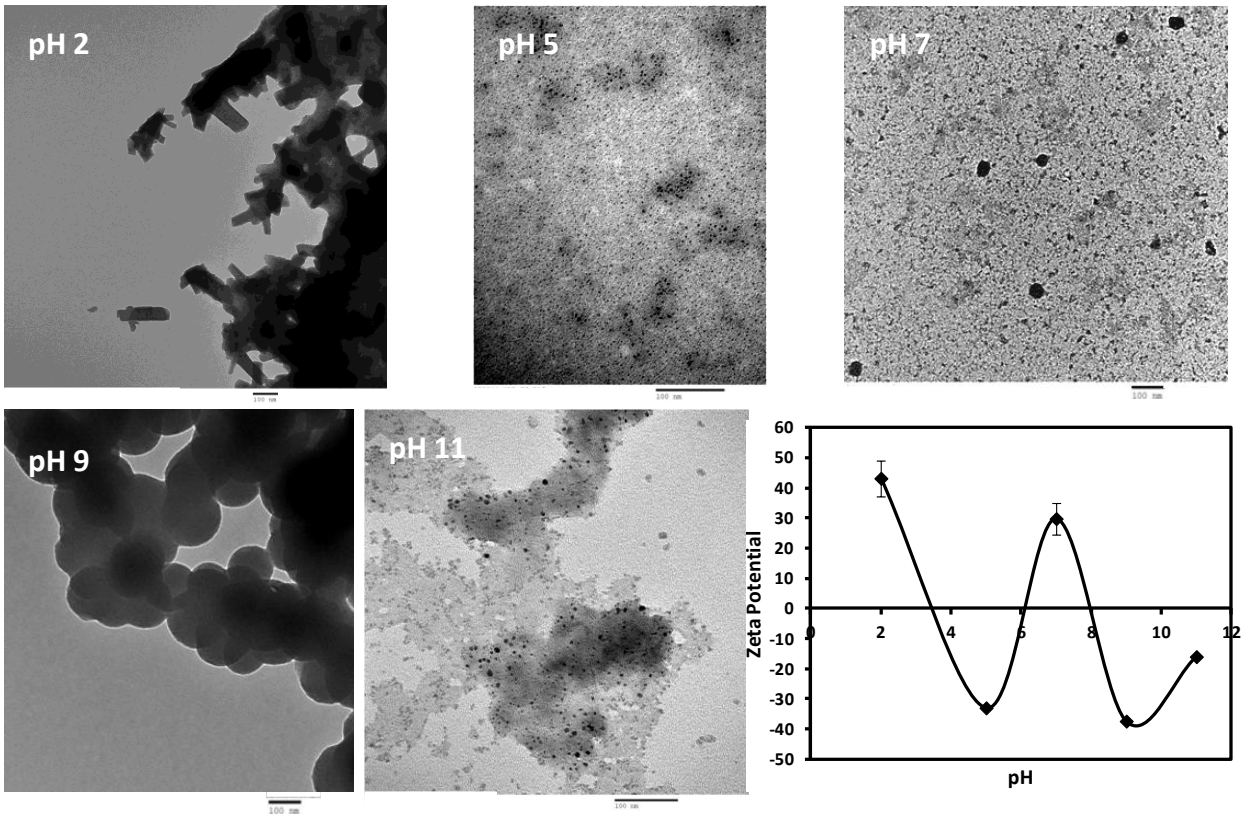


Figure 3.4. The NIR nanoGUMBOS, [1061][Ascorbate] prepared in different pH media yielded different sizes and shapes (scale bars are at 100 nm).

Synthesis of [1061][Ascorbate] nanoGUMBOS at pH 2.0 formed rods (38.8 ± 12.9 nm), but did not aggregate the rods into globular structures as seen with for other nanoGUMBOS (Figure 3.4). The zeta potential for the stable nanoGUMBOS in pH 2.0 media was +43.2 mV. The FTIR spectrum for the [1061][Ascorbate] nanoGUMBOS was similar to the [1048][Ascorbate] nanoGUMBOS due to the [Ascorbate] anion protonation, which resulted in a precipitated formation of [1061][Cl] (Appendix, Figure A3.2D). Nevertheless, protonation of the [Ascorbate] anion was not shown to take place with the nanoGUMBOS synthesized in pH 5.0,

7.0, 9.0, and 11.0 media. The respective particle sizes for nanoGUMBOS synthesized in pH 5.0, 7.0, 9.0, and 11.0 media are 5.0 ± 1.3 nm, 36.3 ± 8.7 nm, 22.5 ± 5.6 nm, and 8.3 ± 4.2 nm. These nanoGUMBOS were very stable within their respective media having zeta potentials of -33.0, +29.8, -37.4, and -16.0 mV. The nanoGUMBOS that ionically bonded to the [1061] cation were observed to have more spherical, stable, and less aggregated particles unlike the [1048] cation counterpart. The surface charges were high enough to prevent nanoparticle aggregation for the [1061] nanoGUMBOS when synthesized in different pH media (Table 3.2).

Table 3.2 A compiled list of the [1061] nanoGUMBOS spectral and morphological characteristics for [Deoxycholate] and [Ascorbate], respectively, show a trend of aggregation and zeta-potential with an increased pH media. The bold lines represent the divisions of pKa values.

[1061][Deoxycholate] - pKa 6.6						
pH	**Size (nm)**	**Aggregation**	**Zeta Potential (mV)**	**Absorbance (1064 nm)**	**ΔT Irradiation (°C)**	**GUMBOS Photothermal Efficiency %**
2	228	No	43.9	0.1184	26.16	13.03
5	84.1	No	-39.4	0.1495	24.77	
7	8.8	No	-13.0	0.1674	23.36	
9	142.5	No	-7.87	0.1500	19.84	
11	55.0	No	34.7	0.1530	24.48	

[1061][Ascorbate] - pKa 4.2, 11.6						
pH	**Size (nm)**	**Aggregation**	**Zeta Potential (mV)**	**Absorbance (1064 nm)**	**ΔT Irradiation (°C)**	**GUMBOS Photothermal Efficiency %**
2	38.8	No	43.2	0.0505	17.99	20.70
5	5.0	No	-33.0	0.0831	19.57	
7	36.3	No	29.8	0.0809	20.49	
9	22.5	No	-37.4	0.0569	16.21	
11	8.3	No	-16.0	0.0832	23.26	

3.4 Photospectral Characteristics of GUMBOS & NanoGUMBOS

An 80 µM concentration of bulk GUMBOS dissolved in acetone had absorbance maxima near their intended absorbance as shown in Figure 3.5. The [1048] GUMBOS' exhibited slight blue shifts due to the change in ionically-bound anions from the starting material (e.g $[BF_4]$, 1042 nm). This shift can be attributed to π-π stacking from the aromatic rings during dimerization self-assembly.[27-29] However, the [1061] GUMBOS' did not exhibit shifts of

absorbance maximum, but rather slight spectral changes. These spectral phenomena for the [1061] GUMBOS were similarly seen with the [1061] nanoGUMBOS (Figures 3.5 & 3.6); however, the absorbance maxima of nanoGUMBOS relative to GUMBOS red-shifted once synthesized.[29] The [1048] nanoGUMBOS maintained their absorbance spectral characteristic while the [1061] nanoGUMBOS lacked in clearly defined absorbance peaks (Figure 3.6).

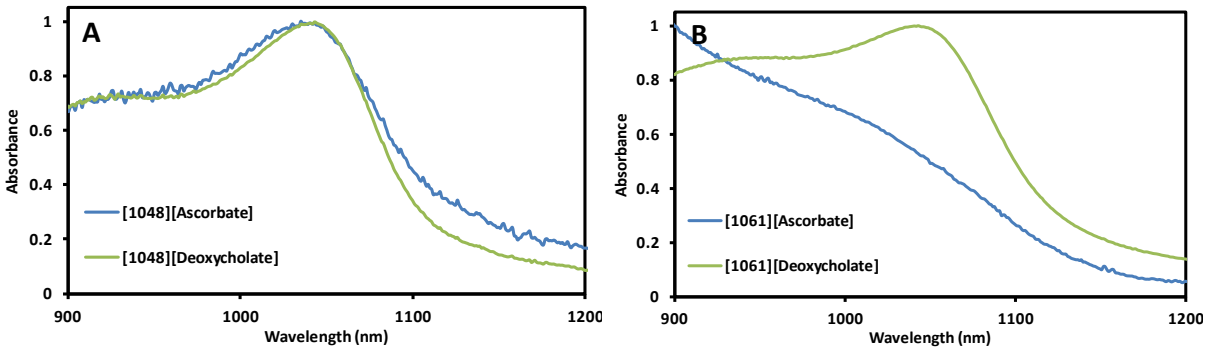


Figure 3.5 The GUMBOS were dissolved in acetone at a concentration of 80 μM and absorbance normalized. (A) [1048] GUMBOS maxima were, respectively, 1035 and 1045 nm. (B) [1061] GUMBOS apexes were at 1045 nm.

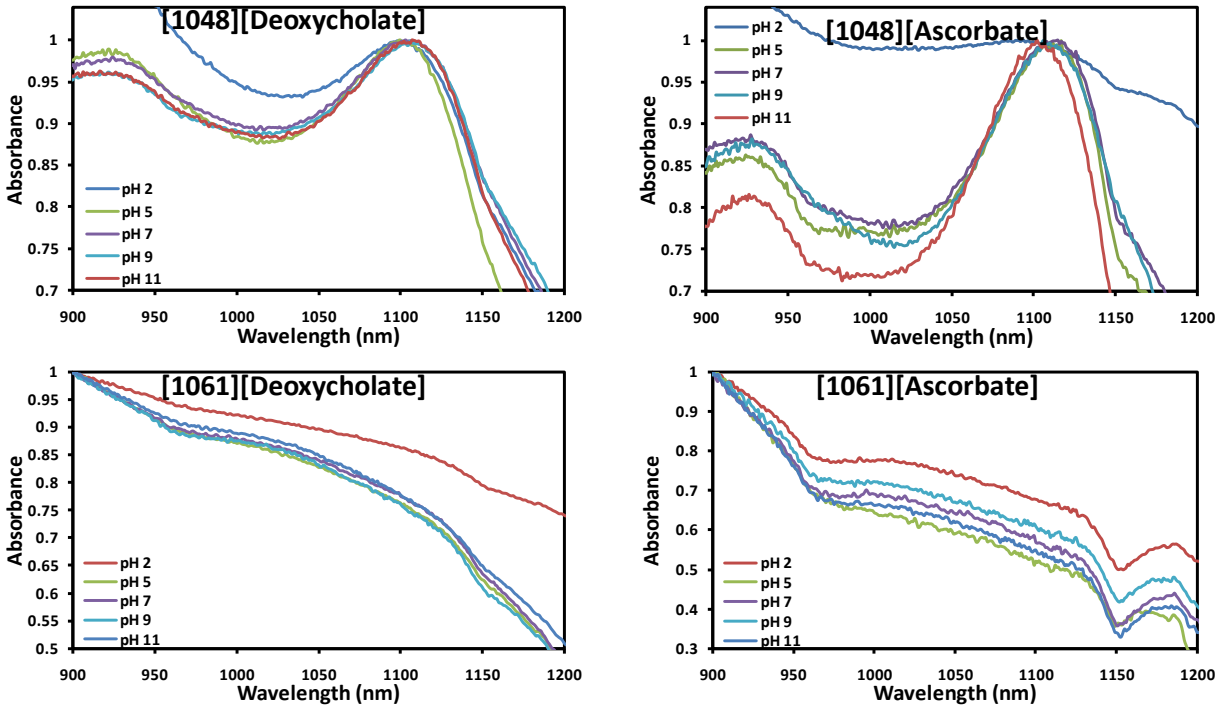


Figure 3.6 The [1048] nanoGUMBOS showed spectral shifts among different pH, while it was difficult to ascertain with the [1061] nanoGUMBOS.

The defined spectral characteristic shape and a trend in apex shift of absorbance of the [1048] nanoGUMBOS were maintained with increased pH values. The absorbance spectrum for [1061] nanoGUMBOS exhibited a broadening previously encountered in nanoGUMBOS attributed to dye aggregation.[30] The absorbance red-shifted for [1048][Deoxycholate] nanoGUMBOS as the pH of the aqueous media increased (Figure 3.7). Absorbance for [1048][Ascorbate] nanoGUMBOS in a pH 5 aqueous media was recorded at 1117 nm, however, with an increase in pH aqueous media the absorbance maxima blue-shifted (i.e. pH 11 = 1104 nm). The aggregation of the nanoGUMBOS, shapes, and sizes are possibly the cause for this spectral phenomenon. The wavelength of interest for these nanoGUMBOS is the emission wavelength of the Nd:YVO_4 (i.e. 1064 nm) used to create a photothermal response.

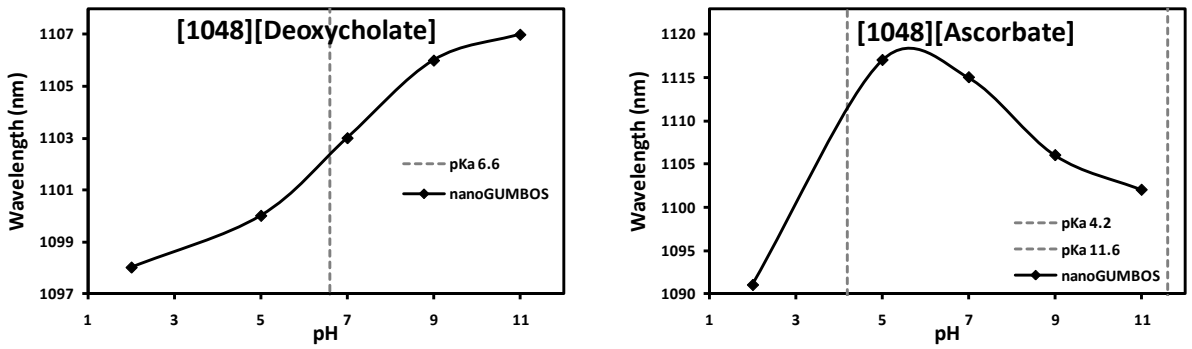


Figure 3.7 The nanoGUMBOS showed an inverse parabola trend of absorbance maximum with an increase in pH between the pKa values (grey vertical dashes).

3.5 Photothermal Characteristics

The bulk solid GUMBOS achieved temperatures between 200 – 500 °C within the first 10 seconds of continuous NIR irradiation at 1000 mW for 4 milligrams of sample. The [1048][Ascorbate] reached a temperature of 511 ± 41.9 °C, and the [1048][Deoxycholate] GUMBOS reached a temperature of 411 ± 70.3 °C after five minutes continuous NIR irradiation (Figure 3.8A). The bulk GUMBOS ionically bound to the [1061] cation yielded lower photothermal temperatures upon NIR irradiation (Figure 3.8B). The [1061][Deoxycholate]

yielded a temperature of 310 ± 46.3 °C, and [1061][Ascorbate] achieved a temperature of 267 ± 44.3 °C after five minutes.

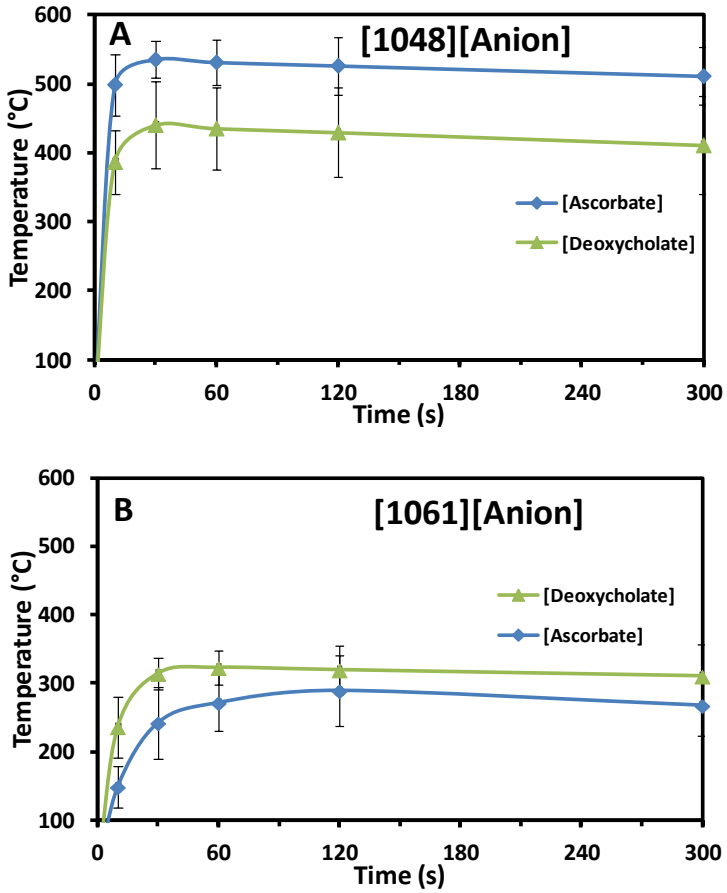


Figure 3.8 Photothermal profile of a 4 mg bulk (A) [1048] and (B) [1061] GUMBOS sample under continuous NIR irradiation for five minutes at a 1000 mW shows a dramatic temperature increase.

The photothermal response from 1000 mW of laser irradiation after five minutes on 0.500 mL aqueous suspension nanoGUMBOS sample shared parabola-like trends among the respective nanoGUMBOS in their pH media and their anions respective pKa values (Figures 3.9 and 3.10). The [1048] nanoGUMBOS overall averaged a temperature increase of 20.6°C. [1048][Ascorbate] in pH 5 transducing the most amount of heat difference at 23.8 °C, and [1048][Deoxycholate] in pH 11.0 with the least at 16.1 °C (Table 3.1).

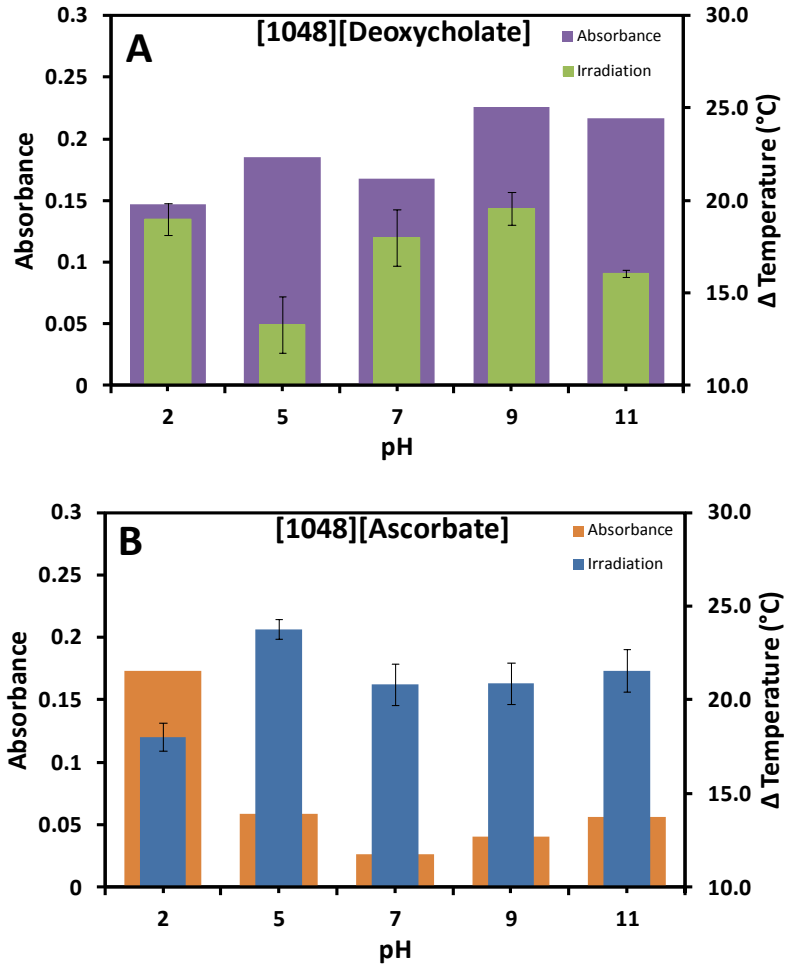


Figure 3.9 The absorbance at 1064 nm and photothermal response shows a trend as pH increases among the (A) [1048][Deoxycholate] and (B) [1048][Ascorbate] nanoGUMBOS.

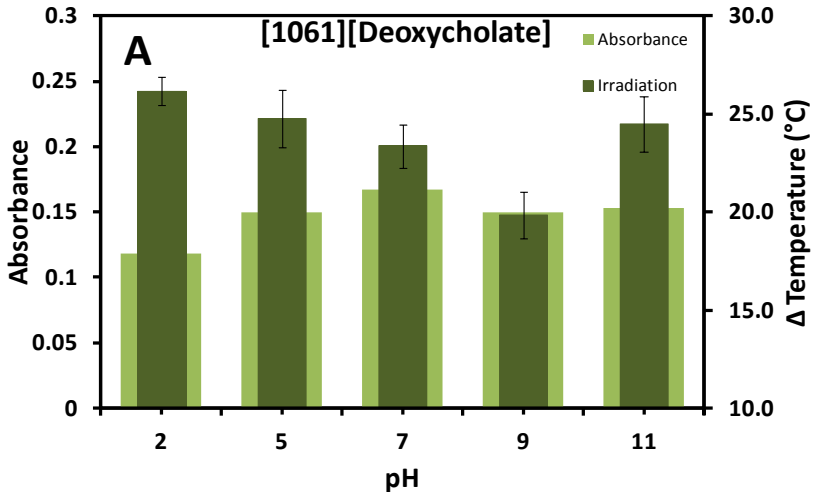
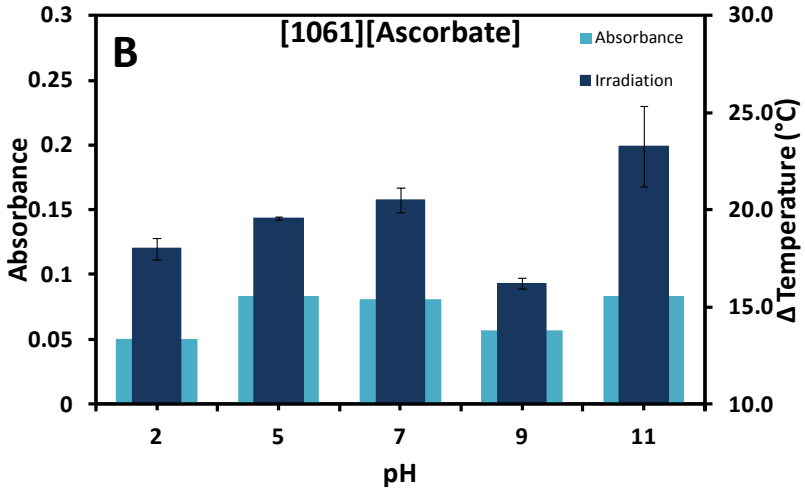


Figure 3.10 The absorbance at 1064 nm and photothermal response shows a trend as pH increases among the (A) [1061][Deoxycholate] and (B) [1061][Ascorbate] nanoGUMBOS.

Figure 3.10 *Continued.*



Among the [1048] anions, [1048][Ascorbate] generated a higher photothermal response at 21.0 °C, while [1048][Deoxycholate] at released 17.2 °C. The photothermal efficiencies (η) of the nanoGUMBOS were calculated using equation 3.1 established by Roper *et al*.[31]

$$\eta = \frac{hS(T_G - T_{ST}) - Q_0}{I(1-10^{-A_{1064}})} \qquad \text{Equation 3.1}$$

Herein, h is the heat transfer coefficient and S is the surface area of the cuvette that the nanoGUMBOS suspension was studied. T_G was the highest photothermal temperature recorded from the GUMBOS, and the T_{ST} was the temperature of the GUMBOS prior to irradiation. Q_0 is the thermal energy obtained from the quartz cuvette which was found to be negligible for our wavelength of interest unlike previous studies.[16, 31-32] I is the incident laser power (1 W), and A is the absorbance of the nanoGUMBOS at the laser's excitation wavelength, 1064 nm. The hS component was derived from equation 3.2 and the slope, τ_s, of time vs Ln(Θ) using the temperature increase upon laser irradiation (Figures 3.11).

$$hS = \frac{\sum mC_p}{\tau_s} \qquad \text{Equation 3.2}$$

In equation 3.2, m is the mass of the nanoGUMBOS in the sample, and C_p is the experimentally determined heat capacity for the GUMBOS (Table 3.3). Because the heat capacities were

measured using bulk GUMBOS opposed to suspended nanoGUMBOS, the photothermal efficiency variables were taken from the bulk measurements since the photoreaction chemistry occurs directly on the material.

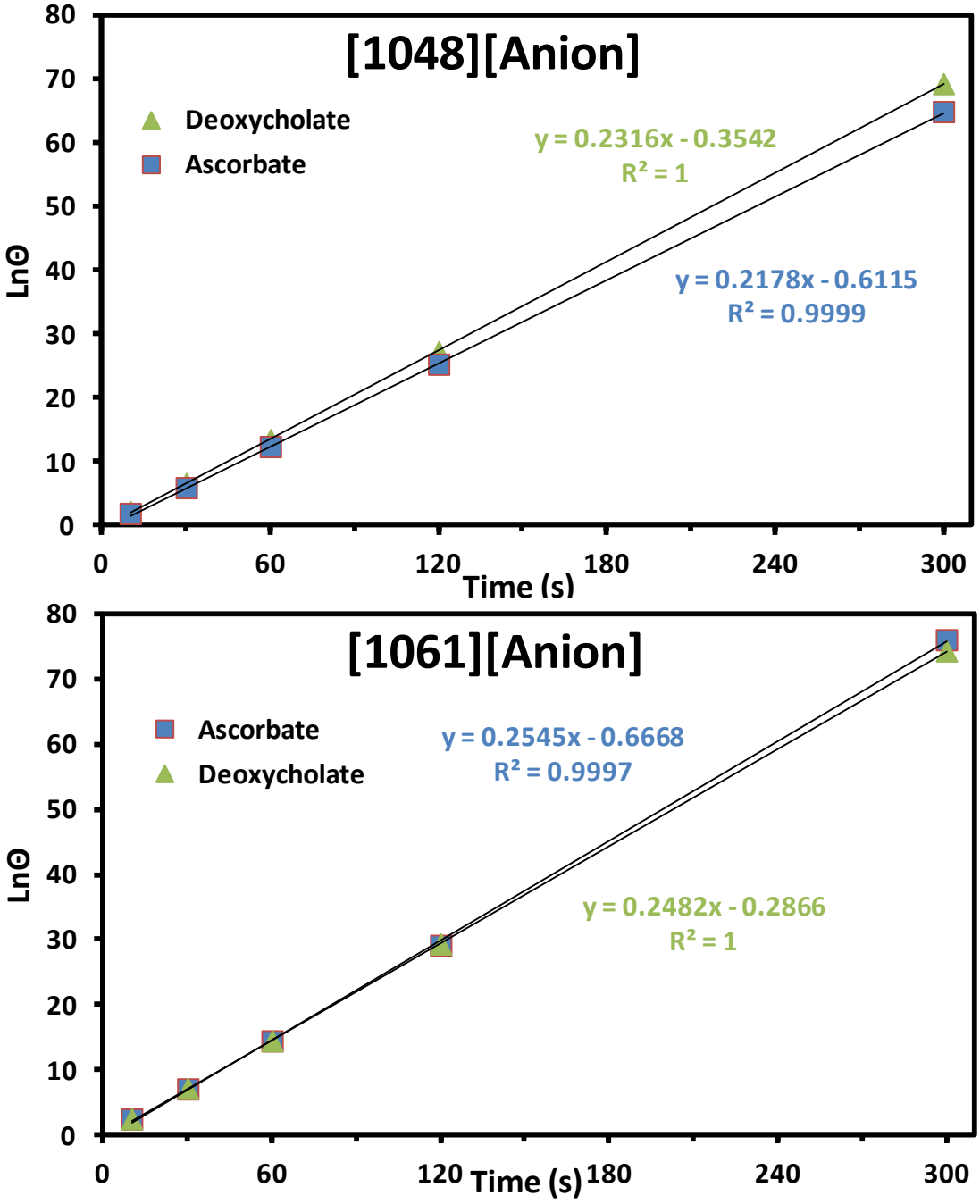


Figure 3.11 The slope of natural log of the driving force temperature versus time is an integral component for finding the photothermal efficiency of the nanoGUMBOS.

Table 3.3 The heat capacities (C_p) for the GUMBOS were experimentally determined in triplicate by a modulated DSC instrument.

Heat Capacity (C_p) J/(g °C)					
GUMBOS	**at 25 °C**	**at 40 °C**	**at 50 °C**	**at 60 °C**	**at 70 °C**
[1048][Deoxycholate]	0.9240	0.9805	1.0420	1.1335	1.1985
[1048][Ascorbate]	1.0877	1.1437	1.1893	1.2367	1.2787
[1061][Deoxycholate]	0.8184	0.8598	0.8880	0.9180	0.9504
[1061][Ascorbate]	0.8204	0.8552	0.8898	0.9207	0.9675

The dimensionless driving force temperature, Θ, was calculated using the room temperature, T_{RT}, along with a control temperature increase of the [Anion] independent from the [Cation], T_A, in equation 3.3:

$$\Theta = \frac{T_{RT} - T_A}{T_{RT} - T_G} \qquad \text{Equation 3.3}$$

A correlation was not observed with the photothermal response of the nanoGUMBOS with aggregation and size. It was noticed, however, that the [1048] and [1061] cations ionically bound to [Ascorbate] were more photothermally efficient when converting NIR light energy into thermal energy. The [1048][Ascorbate] and [1061][Ascorbate] were calculated from the bulk materials as having a photothermal efficiency of 64.4% and 20.7%, respectively. The less efficient GUMBOS, [1048][Deoxycholate] and [1061][Deoxycholate], were calculated to have a photothermal efficiency of 19.7% and 13.0%, respectively. This can be explained by dissecting the efficiency equation and qualitatively recognizing that those nanoGUMBOS had a lower absorbance value at the lasers wavelength. Speculation can be made about the higher photothermal efficiency due to the conjugate double bond in [Ascorbate]. The conjugated double bond decreases the highest occupied molecular orbital (HOMO) and lowest unoccupied molecular orbital (LUMO) band gap; therefore, requiring lesser energy to promote the electron upon excitation.[33-34]

3.6 Band Gap Calculations

Band gap distance is important in the understanding of how efficiently a photon can promote an electron from the HOMO to the LUMO.[35] Manipulating or using a compound that has a smaller band gap has been shown to increase the fluorescence efficiency,[36] or in this case the photothermal efficiency (Table 3.4). Calculating the band gap energies (eV) were performed by inserting absorbance onset (λ_{onset}) values from the aqueous suspension of nanoGUMBOS in equation 3.4:[34, 37-38]

$$E_{opt} = \frac{hc}{\lambda_{onset}} \qquad \text{Equation 3.4}$$

The constants in the equation are the speed of light (3.00×10^8 m s^{-1}), c, and Planck's constant, h (4.136×10^{-15} eV · s). The following are the trends for GUMBOS band gap energy relative to photothermal efficiency:

$$[1048][Ascorbate] - [1061][Ascorbate] - [1048][Deoxycholate] - [1061][Deoxycholate]$$

$\longrightarrow$ Increasing Band Gap Energy

$\longleftarrow$ Increasing Photothermal Efficiency

The four GUMBOS coincide with literature understanding of how electron withdrawing groups are typically more photo-efficient.[33-34, 37-38] By examining the molecular structure of the cations, [1048] and [1061], it is noticed that nitrogen and sulfur atoms exist in the ring systems, respectively. According to the electronegativity Pauling scale nitrogen is χ=3.04, and sulfur is 2.58.[26] The more electron pull of the nitrogen in concert with two additional chlorine atoms (χ=3.16) gives the [1048] cation a slightly smaller band gap than the [1061] cation as observed in previous literature.[39] The [Ascorbate] anion is more electron withdrawing than the [Deoxycholate] anion due to more oxygen atoms (χ=3.44) with a carbonyl and an oxygen within the conjugated lactone system. The electronegative atoms and electron withdrawing groups have

led to the decrease in band gap energies, thus allowing for more photothermal efficient GUMBOS.

Table 3.4 Photothermal efficiency (η) increases as band gap energy (eV) decreases due to the GUMBOS electron withdrawing groups.

	Deoxycholate				Ascorbate			
	η%	**eV**	**λ_{max} (nm)**	**λ_{onset} (nm)**	**η%**	**eV**	**λ_{max} (nm)**	**λ_{onset} (nm)**
1048	19.7	0.886	1097	1400	64.4	0.861	1114	1440
1061	13.0	0.892	1013	1390	20.7	0.881	1108	1408

3.7 Conclusion

NIR nanoGUMBOS were studied for characterization of photothermal effects and nanoparticle formation in different pH media. The NIR nanoGUMBOS formed nanorods when synthesized in a pH media of 2.0, which protonated the anions and forcing the cations to ionically bind to excess chloride anion. The data suggests that the surface charge required to limit aggregation for each type of nanoGUMBOS is different for each compound. For example, [1061] nanoGUMBOS had more stable surface charge resulting in limited nanoparticle aggregation. Nevertheless, [1048] nanoGUMBOS had higher electronegativity resulting to smaller band gap energies, thus higher photothermal efficiencies. The GUMBOS with the [Ascorbate] anion exhibited higher photothermal efficiency than the [Deoxycholate] anion due to smaller band gap energy from the electron withdrawing groups. This study helps provide a physical understanding of GUMBOS based photothermal materials for the potential use as hyperthermal therapeutics.

3.8 References

1. Tesfai, A.; El-Zahab, B.; Kelley, A. T.; Li, M.; Garno, J. C.; Baker, G. A.; Warner, I. M. Magnetic and Nonmagnetic Nanoparticles from a Group of Uniform Materials Based on Organic Salts. *ACS Nano* **2009,** *3 (10)*, 3244-3250.

2. Li, M.; De Rooy, S. L.; Bwambok, D. K.; El-Zahab, B.; DiTusa, J. F.; Warner, I. M. Magnetic Chiral Ionic Liquids Derived from Amino Acids. *Chem. Commun.* **2009,** *(45)*, 6922-6924.

3. Bwambok, D. K.; Challa, S. K.; Lowry, M.; Warner, I. M. Amino Acid-Based Fluorescent Chiral Ionic Liquid for Enantiomeric Recognition. *Anal. Chem.* **2010,** *82 (12)*, 5028-5037.

4. Tesfai, A.; El-Zahab, B.; Bwambok, D. K.; Baker, G. A.; Fakayode, S. O.; Lowry, M.; Warner, I. M. Controllable Formation of Ionic Liquid Micro- and Nanoparticles via a Melt-Emulsion-Quench Approach. *Nano Lett.* **2008,** *8 (3)*, 897-901.

5. de Rooy, S. L.; Das, S.; Li, M.; El-Zahab, B.; Jordan, A.; Lodes, R.; Weber, A.; Chandler, L.; Baker, G. A.; Warner, I. M. Ionically Self-Assembled, Multi-Luminophore One-Dimensional Micro- and Nanoscale Aggregates of Thiacarbocyanine GUMBOS. *J. Phys. Chem. C* **2012,** *116 (14)*, 8251-8260.

6. Dumke, J. C.; El-Zahab, B.; Challa, S.; Das, S.; Chandler, L.; Tolocka, M.; Hayes, D. J.; Warner, I. M. Lanthanide-Based Luminescent NanoGUMBOS. *Langmuir* **2010,** *26 (19)*, 15599-15603.

7. Bwambok, D. K.; El-Zahab, B.; Challa, S. K.; Li, M.; Chandler, L.; Baker, G. A.; Warner, I. M. Near-Infrared Fluorescent NanoGUMBOS for Biomedical Imaging. *ACS Nano* **2009,** *3 (12)*, 3854-3860.

8. Bashkatov, A. N.; Genina, E. A.; Kochubey, V. I.; Tuchin, V. V. Optical Properties of Human Skin, Subcutaneous and Mucous Tissues in the Wavelength Range from 400 to 2000 nm. *J. Phys. D: Appl. Phys.* **2005,** *38 (15)*, 2543-2555.

9. Luo, S. L.; Zhang, E. L.; Su, Y. P.; Cheng, T. M.; Shi, C. M. A Review of NIR dyes in Cancer Targeting and Imaging. *Biomaterials* **2011,** *32 (29)*, 7127-7138.

10. Liao, C. T.; Chen, H. F.; Su, H. C.; Wong, K. T. Tailoring Balance of Carrier Mobilities in Solid-State Light-Emitting Electrochemical Cells by Doping a Carrier Trapper to Enhance Device Efficiencies. *J. Mater. Chem.* **2011,** *21 (44)*, 17855-17862.

11. Kennedy, L. C.; Bickford, L. R.; Lewinski, N. A.; Coughlin, A. J.; Hu, Y.; Day, E. S.; West, J. L.; Drezek, R. A. A New Era for Cancer Treatment: Gold-Nanoparticle-Mediated Thermal Therapies. *Small* **2011,** *7 (2)*, 169-183.

12. Whitney, M. A.; Crisp, J. L.; Nguyen, L. T.; Friedman, B.; Gross, L. A.; Steinbach, P.; Tsien, R. Y.; Nguyen, Q. T. Fluorescent Peptides Highlight Peripheral Nerves During Surgery in Mice. *Nat. Biotechnol.* **2011,** *29 (4)*, 352-356.

13. Nguyen, Q. T.; Olson, E. S.; Aguilera, T. A.; Jiang, T.; Scadeng, M.; Ellies, L. G.; Tsien, R. Y. Surgery with Molecular Fluorescence Imaging Using Activatable Cell-Penetrating

Peptides Decreases Residual Cancer and Improves Survival. *Proc. Natl. Acad. Sci. U. S. A.* **2010,** *107 (9)*, 4317-4322.

14. Olson, E. S.; Jiang, T.; Aguilera, T. A.; Nguyen, Q. T.; Ellies, L. G.; Scadeng, M.; Tsien, R. Y. Activatable Cell Penetrating Peptides Linked to Nanoparticles as Dual Probes for In Vivo Fluorescence and MR Imaging of Proteases. *Proc. Natl. Acad. Sci. U. S. A.* **2010,** *107 (9)*, 4311-4316.

15. Bardhan, R.; Lal, S.; Joshi, A.; Halas, N. J. Theranostic Nanoshells: From Probe Design to Imaging and Treatment of Cancer. *Acc. Chem. Res.* **2011,** *44 (10)*, 936-946.

16. Tian, Q. W.; Jiang, F. R.; Zou, R. J.; Liu, Q.; Chen, Z. G.; Zhu, M. F.; Yang, S. P.; Wang, J. L.; Wang, J. H.; Hu, J. Q. Hydrophilic Cu_9S_5 Nanocrystals: A Photothermal Agent with a 25.7% Heat Conversion Efficiency for Photothermal Ablation of Cancer Cells In Vivo. *ACS Nano* **2011,** *5 (12)*, 9761-9771.

17. Lovell, J. F.; Jin, C. S.; Huynh, E.; Jin, H. L.; Kim, C.; Rubinstein, J. L.; Chan, W. C. W.; Cao, W. G.; Wang, L. V.; Zheng, G. Porphysome Nanovesicles Generated by Porphyrin Bilayers for Use as Multimodal Biophotonic Contrast Agents. *Nat. Mater.* **2011,** *10 (4)*, 324-332.

18. Ghosh, S.; Dutta, S.; Gomes, E.; Carroll, D.; D'Agostino, R.; Olson, J.; Guthold, M.; Gmeiner, W. H. Increased Heating Efficiency and Selective Thermal Ablation of Malignant Tissue with DNA-Encased Multiwalled Carbon Nanotubes. *ACS Nano* **2009,** *3 (9)*, 2667-2673.

19. Gobin, A. M.; Watkins, E. M.; Quevedo, E.; Colvin, V. L.; West, J. L. Near-Infrared-Resonant Gold/Gold Sulfide Nanoparticles as a Photothermal Cancer Therapeutic Agent. *Small* **2010,** *6 (6)*, 745-752.

20. Kang, H. Z.; Trondoli, A. C.; Zhu, G. Z.; Chen, Y.; Chang, Y. J.; Liu, H. P.; Huang, Y. F.; Zhang, X. L.; Tan, W. H. Near-Infrared Light-Responsive Core-Shell Nanogels for Targeted Drug Delivery. *ACS Nano* **2011,** *5 (6)*, 5094-5099.

21. Arrigoni, C.; Camozzi, D.; Imberti, B.; Mantero, S.; Remuzzi, A. The Effect of Sodium Ascorbate on the Mechanical Properties of Hyaluronan-Based Vascular Constructs. *Biomaterials* **2006,** *27 (4)*, 623-630.

22. Majd, E. S.; Goldberg, M.; Stanislawski, L. In Vitro Effects of Ascorbate and Trolox on the Biocompatibility of Dental Restorative Materials. *Biomaterials* **2003,** *24 (1)*, 3-9.

23. Bhattacharjee, J.; Verma, G.; Aswal, V. K.; Date, A. A.; Nagarsenker, M. S.; Hassan, P. A. Tween 80-Sodium Deoxycholate Mixed Micelles: Structural Characterization and Application in Doxorubicin Delivery. *J. Phys. Chem. B* **2010,** *114 (49)*, 16414-16421.

24. Selvam, S.; Andrews, M. E.; Mishra, A. K. A Photophysical Study on the Role of Bile Salt Hydrophobicity in Solubilizing Amphotericin B Aggregates. *J. Pharm. Sci.* **2009,** *98 (11),* 4153-4160.

25. Zeta Potential Theory. In *Zetasizer Nano Series*, 2.1 ed.; Malvern Instruments Ltd.: 2004; pp 1-12.

26. *CRC Handbook of Chemistry and Physics*. 88th ed.; Lide, D. R., Ed. CRC Press: Boca Raton, FL, 2008; Chapter 8, p 42-51.

27. Arena, G.; Scolaro, L. M.; Pasternack, R. F.; Romeo, R. Synthesis, Characterization, and Interaction with DNA of the Novel Metallointercalator Cationic Complex (2,2'6',2"-Terpyridine)Methylplatinum(II). *Inorg. Chem.* **1995,** *34 (11),* 2994-3002.

28. Kubat, P.; Lang, K.; Janda, P.; Anzenbacher, P. Interaction of Porphyrins with a Dendrimer Template: Self-Aggregation Controlled by pH. *Langmuir* **2005,** *21 (21),* 9714-9720.

29. Jordan, A. N.; Das, S.; Siraj, N.; de Rooy, S. L.; Li, M.; El-Zahab, B.; Chandler, L.; Baker, G. A.; Warner, I. M. Anion-Controlled Morphologies and Spectral Features of Cyanine-Based NanoGUMBOS - An Improved Photosensitizer. *Nanoscale* **2012,** *4 (16),* 5031-5038.

30. Das, S.; Bwambok, D.; El-Zahab, B.; Monk, J.; de Rooy, S. L.; Challa, S.; Li, M.; Hung, F. R.; Baker, G. A.; Warner, I. M. Nontemplated Approach to Tuning the Spectral Properties of Cyanine-Based Fluorescent NanoGUMBOS. *Langmuir* **2010,** *26 (15),* 12867-12876.

31. Roper, D. K.; Ahn, W.; Hoepfner, M. Microscale Heat Transfer Transduced by Surface Plasmon Resonant Gold Nanoparticles. *J. Phys. Chem. C* **2007,** *111 (9),* 3636-3641.

32. Cole, J. R.; Mirin, N. A.; Knight, M. W.; Goodrich, G. P.; Halas, N. J. Photothermal Efficiencies of Nanoshells and Nanorods for Clinical Therapeutic Applications. *J. Phys. Chem. C* **2009,** *113 (28),* 12090-12094.

33. Eakins, G. L.; Alford, J. S.; Tiegs, B. J.; Breyfogle, B. E.; Stearman, C. J. Tuning HOMO-LUMO Levels: Trends Leading to the Design of 9-Fluorenone Scaffolds with Predictable Electronic and Optoelectronic Properties. *J. Phys. Org. Chem.* **2011,** *24 (11),* 1119-1128.

34. Ellinger, S.; Graham, K. R.; Shi, P. J.; Farley, R. T.; Steckler, T. T.; Brookins, R. N.; Taranekar, P.; Mei, J. G.; Padilha, L. A.; Ensley, T. R.; Hu, H. H.; Webster, S.; Hagan, D. J.; Van Stryland, E. W.; Schanze, K. S.; Reynolds, J. R. Donor-Acceptor-Donor-based p-Conjugated Oligomers for Nonlinear Optics and Near-IR Emission. *Chem. Mater.* **2011,** *23 (17),* 3805-3817.

35. Wang, R.; Deng, L.; Zhang, T.; Li, J. Substituent Effect on the Photophysical Properties, Electrochemical Properties and Electroluminescence Performance of Orange-Emitting Iridium Complexes. *Dalton Trans.* **2012,** *41 (22),* 6833-6841.

36. Kwak, J.; Bae, W. K.; Lee, D.; Park, I.; Lim, J.; Park, M.; Cho, H.; Woo, H.; Yoon, D. Y.; Char, K.; Lee, S.; Lee, C. Bright and Efficient Full-Color Colloidal Quantum Dot Light-Emitting Diodes Using an Inverted Device Structure. *Nano Lett.* **2012,** *12 (5),* 2362-2366.

37. Poriel, C.; Rault-Berthelot, J.; Barrière, F.; Slawin, A. M. Z. New Dispiro Compounds: Synthesis and Properties. *Org. Lett.* **2008,** *10 (3),* 373-376.

38. Zhang, G. B.; Fu, Y. Y.; Xie, Z. Y.; Zhang, Q. Synthesis and Photovoltaic Properties of New Low Bandgap Isoindigo-Based Conjugated Polymers. *Macromolecules* **2011,** *44 (6),* 1414-1420.

39. Özen, A. S.; Atilgan, C.; Sonmez, G. Noncovalent Intramolecular Interactions in the Monomers and Oligomers of the Acceptor and Donor Type of Low Band Gap Conducting Polymers. *J. Phys. Chem. C* **2007,** *111 (44),* 16362-16371.

Chapter 4. Tumor-Targeting Hyperthermal Near-Infrared NanoGUMBOS

4.1 Introduction

The American Cancer Society estimates that more than two million new cases of cancer will be recorded in 2012. Fortunately, only about 32% of the victims will become terminal due to the increasing and successful cancer research being performed.[1] One of the oldest therapeutics for cancer treatments dating back to antiquity is the use of cauterization, or heat.[2] Heat to destroy cancerous tumors is practiced presently, but less invasive using photothermal nanoparticles generated from radiowaves,[3] microwaves,[4] magnetic field,[5] or near infrared laser.[6] Nanoparticles such as gold[7-8] and porphysomes have provided greater than the necessary temperature threshold of 41 – 45 °C to initiate cancer cell death.[9-10] These nanoparticles underwent photothermal conversion when subjected to near infrared (NIR) laser light. NIR laser irradiation is advantageous due to the human skin weakly absorbent window between wavelength ranges 750 – 1100 nm.[11] Many cancer therapeutic nanoparticles conjugate folate molecules to selectively target cancer cells.[12-13] Folate (or vitamin B_9) is used to synthesize DNA, repair DNA, and for cell proliferation.[14] The cellular division process is facilitated by folic acid, because cancer cells divide uncontrollably thus having an overexpression of folate-receptor alpha proteins.[15] The folate molecule has a large affinity towards this protein; hence using it is a targeting agent. The plethora of percutaneous hyperthermia techniques demonstrates promising methods for cancer therapy.

A new class of nanomaterials has been derived from a group of uniformed materials based on organic salts (GUMBOS). GUMBOS have a unique set of properties such as limited volatility, variable viscosity and solubility, and melting temperature range of 25 – 250 °C. By performing a metathesis reaction properties are tunable depending on the ionic species whether

the cations and/or anions are fluorescent,[16-19] magnetic,[19-21] chiral,[18, 21-22] and antibiotic.[23] GUMBOS have been further synthesized into nanomaterials (nanoGUMBOS) to increase surface area, thus allowing for more potential of the desired property. These facile tunable compounds have allowed for a vast number of possible applications towards areas of solar cells,[24] sensors,[25] separations, and biomedical.[16, 19, 23] Herein, a hyperthermal technique involving laser irradiation to generate heat photothermally from a GUMBOS-based near infrared cationic dye and tumor-targeting folate anion is presented.

4.2 Materials and Characterization

4.2.1 Materials

The following chemicals were purchased from Sigma-Aldrich (St. Louis, MO) without further purification: folic acid**,** 1-Butyl-2-[2-[3-[(1-butyl-6-chlorobenz[cd]indol-2(1*H*)-ylidene)ethylidene]-2-chloro-1-cyclohexen-1-yl]ethenyl]-6-chlorobenz[cd]indolium tetrafluoroborate ([1048][BF_4]) and 4-[2-[2-Chloro-3-[(2,6-diphenyl-4*H*-thiopyran-4-ylidene)ethylidene]-1-cyclohexen-1-yl]ethenyl]-2,6-diphenylthiopyrylium tetrafluoroborate ([1061][BF_4]), 18.2 MΩ water, sodium hydroxide (NaOH), dichloromethane (DCM), dimethyl sulfoxide (DMSO), and acetone. AlamarBlue® assay, LIVE/DEAD® Viability/Cytotoxicity Kit (live: calcein-AM and dead: ethidium homodimer-1), and Dulbecco's Modified Eagle Media (DMEM) were purchased from Life Technologies Corporation (Grand Island, NY). The DMEM was modified with 10% Fetal Bovine Serum, 15 mM HEPES, glutamax 100X, non-essential amino acids (NEAA 100X), and sodium pyruvate (NaPyr 100X). Phosphate buffer saline (PBS) was purchased from Fisher Scientific: BioReagents (Fair Lawn, NJ).

4.2.2 Characterization

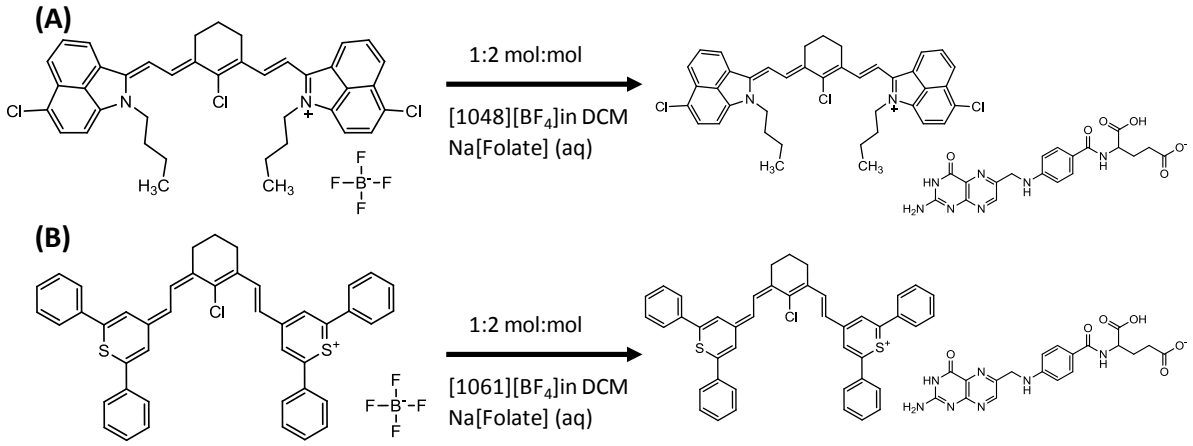
The GUMBOS and nanoGUMBOS infrared absorption measurements were characterized by a Lambda 750 UV-Vis-NIR Spectrophotometer (Perkin-Elmer, Waltham, MA, USA) using a 1 cm pathlength quartz cuvette. Structural characterizations of the GUMBOS were elucidated by the following instruments: Agilent 6210 Electrospray Time-of-Flight Mass Spectrometer, ^{19}F NMR Brüker DPX-250 (250 MHz). Transmission electron microscopy (TEM) images were taken using a JEOL JEM-1011 at the School of Veterinary Medicine (LSU). Dynamic light scattering (DLS) studies were performed with a Zetasizer Nanoseries Nano ZS (Malvern Instruments, Worcestershire, UK) instrument. Fluorescence intensity from the cell assays were recorded from a Wallace Victor2™ (Perkin-Elmer, Waltham, MA, USA) plate reader. Visualizations of the fluorescent live/dead probes were observed by an Olympus IX81 microscope and Hammamatsu C4742 fluorescence detector.

4.2.3 Synthesis of GUMBOS and NanoGUMBOS

Folic acid was synthesized into sodium folate by a 1:1 mol:mol ratio of folic acid and NaOH. Sodium folate confirmation was supported by electrospray mass spectrometry (ESI MS) (Appendix, Figure A4.1). The ESI MS spectrum shows that the folate peak (m/z = 464) was about half of the folic acid peak (m/z = 442), suggesting that only half of the reactant was deprotonated forming sodium folate. The GUMBOS were synthesized via anion exchange method. The cationic dyes were individually dissolved in DCM and mixed with the aqueous anionic precursor salts in a 1:2 mol:mol ratio (Scheme 4.1). The materials were then allowed to mix thoroughly for two days wrapped in aluminum foil to avoid photobleaching prior to washing and purification. The newly synthesized GUMBOS were washed three times and then stored in

the dark at ambient temperatures. Successful metathesis reactions were supported by ^{19}F NMR (Appendix, Figure A4.2).

Scheme 4.1 A metathesis reaction exchanging a folate anion with tetrafluoroborate was done in a 1:2 mol:mol ratio.



NanoGUMBOS were synthesized by a microwave-assisted reprecipitation method in triply distilled 18.2 MΩ water. The GUMBOS were dissolved in acetone at concentration of 2 mM and injected accordingly to have final nanoGUMBOS concentration of 320 μg mL^{-1} in 5 mL of an aqueous suspension. The microwave parameters were set to ramp quickly to 150 °C and hold for five minutes. The nanoGUMBOS product was drop-cast on a 400 mesh ultrathin carbon-film copper TEM grid (Ted Pella Inc., Redding, CA, USA) and DLS was measured.

4.3 Methods

4.3.1 Laser Irradiation

Laser irradiation source was from an infrared (1064 nm) diode-pumped continuous solid-state Nd:YVO_4 laser (Lasermate Group Inc., Pomona, CA, USA). The variable concentrations of nanoGUMBOS were subjected to NIR laser irradiation for at least 30 minutes. Incremental volumes (i.e. 0, 32, 64, and 128 μL) of 320 μg mL^{-1} nanoGUMBOS were added to a glass NMR tube filled with 100 μL of DMEM media. The final nanoGUMBOS concentrations were the

following, respectively: 0, 77.6, 124.9, and 179.6 μg mL^{-1}. The samples experienced a 2 mm diameter focal spot of NIR laser irradiation in triplicates at a power of 32 W cm^{-2}, and measured with a TA (Thermal Analysis) Instruments Thermacouple and Universal Analysis 2000 program (version 4.3A) (Appendix, Figure A4.3).

4.3.2 Cytotoxicity/NanoGUMBOS Control

Cytotoxicity of nanoGUMBOS in malignant MDA-MB-231 breast cancer cells were studied using a concentration of 10,000 cells. The cytotoxicity of nanoGUMBOS were studied in a concentration of 5,000 normal breast cells, HS-578-BST. Live and dead (3% H_2O_2 injection) controls for both cell lines were administered. All cells were incubated at 32 °C and 5% CO_2 in 100 μL modified DMEM and studied in a 96 well-plate with optically clear bottoms and performed in triplicate. Different volume increments (i.e. 4, 16, 32, 64, and 128 μL) of 320 μg mL^{-1} nanoGUMBOS were added in triplicates to individual wells of 100 μL DMEM leading to a final concentration of 12.3, 44.1, 77.6, 124.9, and 179.6 μg mL^{-1}. The nanoGUMBOS were allowed to incubate for 24 hours before preparing the alamarBlue® assay. The medium was removed and washed with PBS solution. The cells were incubated in 100 μL of 10% (v/v) alamarBlue® dye in DMEM media (AB/DMEM) for eight hours. Incubation for eight hours of a concentration of 10,000 cells was determined appropriately for the cells (Appendix, Figure A4.4). The alamarBlue® dye (resazurin) is nonfluorescent in an oxidized environment, but fluorescent (resorufin) in a reduced environment (living cells). Fluorescence from the cell assays were observed in a fluorescence plate reader.

4.3.3 NIR Laser Irradiation Control

Cells prepared as previously mentioned underwent variable duration NIR laser irradiation at 32 W cm^{-2} *sans* nanoGUMBOS. The cells were irradiated for 10, 20, or 30 minutes followed

by immediate removal of the media, then washed with PBS, and incubated in AB/DMEM. Assay plate readings were performed eight hours after 100 µL addition of AB/DMEM media.

4.3.4 Hyperthermal Technique

Cells were prepared as previously mentioned. NanoGUMBOS with final concentrations of 77.6, 124.9, and 179.6 µg mL^{-1} were irradiated with a NIR laser (Appendix, Figure A4.5). The nanoGUMBOS were incubated for four hours before irradiation preparations. Preparations included removal of media, washing cells with PBS, and adding 100 µL of DMEM media to each well plate. Each well plate was exposed to continuous NIR laser irradiation for either 10, 20, or 30 minutes with a laser power density of 32 W cm^{-2}. Post irradiation: media was removed, cells washed with PBS, and incubated with AB/DMEM media for eight hours prior to measuring the fluorescence.

4.3.5 Fluorescence Microscopy

A fluorescence image depicting cell death via hyperthermia was performed by use of fluorescence microscopy. A concentration of 250,000 MDA-MB-231 breast cancer cells were grown in a 12 well-plate in DMEM and allowed to grow to confluency. The cells were injected with 77.6 µg mL^{-1} NIR nanoGUMBOS incubated at 32 °C with 5% CO_2. The NIR nanoGUMBOS were allowed to incubate for four hours before a 30 minute irradiation. Following irradiation the cells were treated with the live/dead assays to exemplify the selectivity of irradiation and nanoGUMBOS towards hyperthermia.

4.3.6 Cellular Uptake

Cellular uptake of nanoGUMBOS was measured employing modified previous methods.[26-27] NanoGUMBOS (final concentration of 77.6 µg mL^{-1}) were injected in 2 mL of modified DMEM media with 250,000 MDA-MB-231 cells in a 12 well-plate. The

nanoGUMBOS incubated for four hours before the media was removed and saved. The cells were washed three times with PBS followed by digestion of the cell walls and dissolution of the nanoGUMBOS using 2 mL DMSO. The resulting solution was saved to measure absorbance from the GUMBOS against a DMSO-digested cell reference. The absorbance measurements were compared to a concentration gradient of variable GUMBOS concentrations dissolved in DMSO (Figure 4.1).

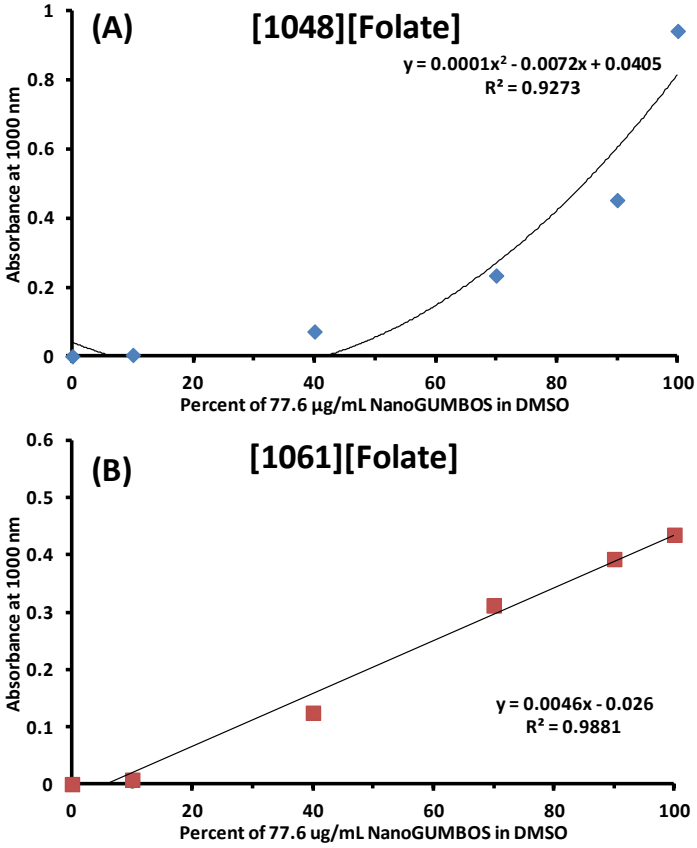


Figure 4.1 Concentration absorbance at 1000 nm gradient of percent of 77.6 µg mL^{-1} (A) [1048][Folate] and (B) [1061][Folate] nanoGUMBOS in DMSO was used to determine the concentration of nanoGUMBOS that entered the MDA-MB-231 cells.

4.4 Results

Presently, literature has gravitated towards gold nanomaterials (e.g. shells, particles, and rods) in producing heat by NIR laser irradiation for hyperthermia.[30-32] Herein a new class of

materials called NIR nanoGUMBOS demonstrates photothermal generation for a hyperthermal cancer therapeutic. The two different NIR nanoGUMBOS, [1048][Folate] and [1061][Folate], were used in the study.

4.4.1 NIR NanoGUMBOS Characterization

A microwave-assisted reprecipitation method was used to synthesize NIR nanoGUMBOS from NIR GUMBOS (Figure 4.2). The TEM micrographs and DLS for [1048][Folate] and [1061][Folate] NIR nanoGUMBOS revealed monodisperse particles with very limited aggregation (Table 4.1). Nanoparticles will typically be recorded to have a larger size with DLS because the instrument measures the average hydrodynamic radius (or slipping plane). The hydrodynamic radius is averaged due to particles being in constant Brownian motion from solvent and other molecule bombardment.

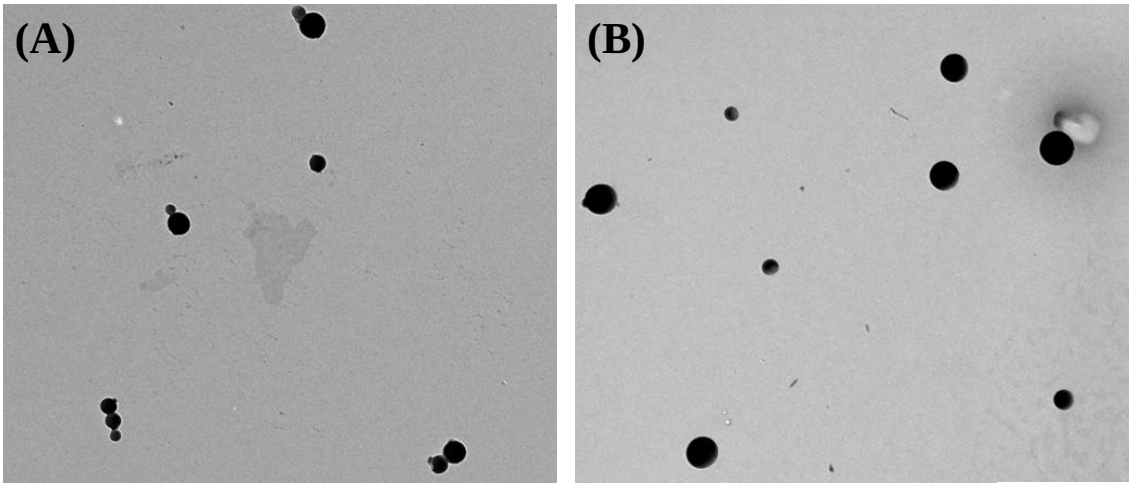


Figure 4.2 The NIR nanoGUMBOS TEM micrograph shows particle sizes for (A) [1048][Folate] at 121 ± 32.5 nm and (B) [1061][Folate] at 144 ± 46.8 nm.

Table 4.1 The NIR nanoGUMBOS were monodisperse under microwave-assisted reprecipitation synthesis.

NanoGUMBOS	NanoGUMBOS size (nm)		
	TEM Micrograph	DLS	PDI
[1048][Folate]	121 ± 32.5	157 ± 2.4	0.137
[1061][Folate]	144 ± 46.8	176 ± 1.2	0.066

The NIR nanoGUMBOS were determined to be 89-93% insoluble after a two week study of the particles suspended in water (Table 4.2). The particles were centrifuged for 20 minutes at 3500 rpm before the top foremost liquid was measured for absorbance (Appendix, Figure A4.6). The wavelength chosen to compare absorbance values was determined by the absorbance maxima from the controlled NIR nanoGUMBOS concentration.

Table 4.2 NIR nanoGUMBOS remained significantly insoluble in an aqueous suspension media.

NanoGUMBOS	Wavelength (nm)	Absorbance		% Difference	% Insoluble
		Control	Centrifuged		
[1048][Folate]	1077	0.219123	0.015503	7.08	92.92
[1061][Folate]	1118	0.051012	0.005738	11.25	88.75

4.4.2 NIR NanoGUMBOS Cytotoxicity

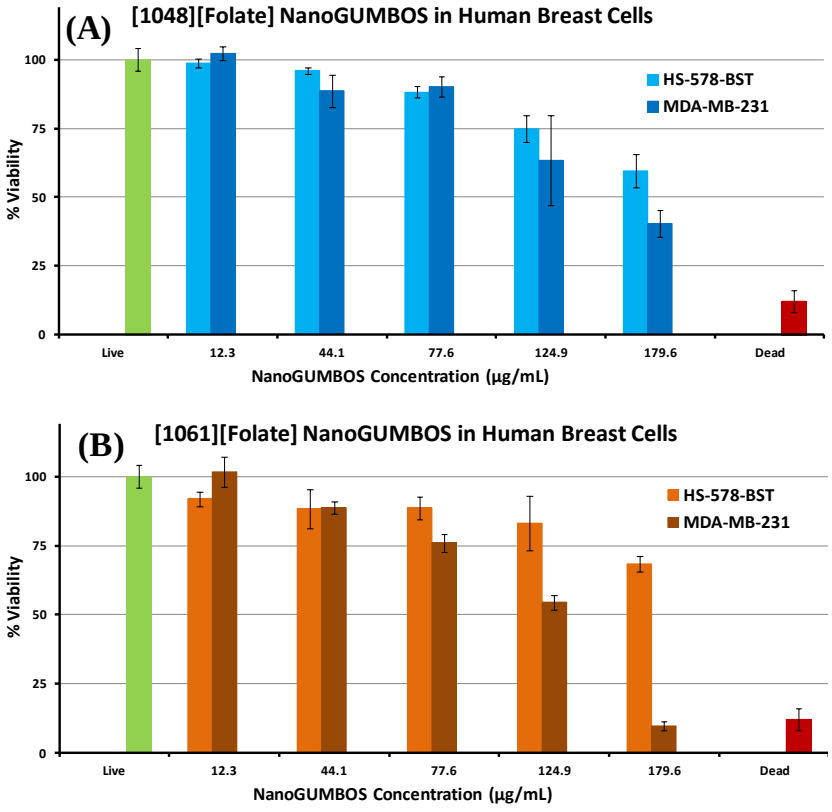


Figure 4.3 Viability studies of (A) [1048][Folate] and (B) [1061][Folate] NIR nanoGUMBOS using an alamarBlue® assay was performed on breast cell lines.

NIR nanoGUMBOS toxicity was determined in a cancerous breast cell line (MDA-MB-231) and noncancerous breast cell line (HS-578-BST) by an alamarBlue® assay (Figure 4.3). The NIR nanoGUMBOS naturally resulted in being toxic to the both cell lines with an increase in concentration; however, the NIR nanoGUMBOS were seemingly more toxic to MDA-MB-231 cells. The median lethal dose (LD_{50}) of NIR nanoGUMBOS was calculated from the slope at which the cell viability decreased (Figure 4.4). The LD_{50} for NIR nanoGUMBOS [1048][Folate] in MDA-MB-231 and HS-578-BST cell lines are 158 and 214 µg mL^{-1}, respectively. The [1061][Folate] NIR nanoGUMBOS LD_{50} for MDA-MB-231 and HS-578-BST are 123 and 278 µg mL^{-1}, respectively.

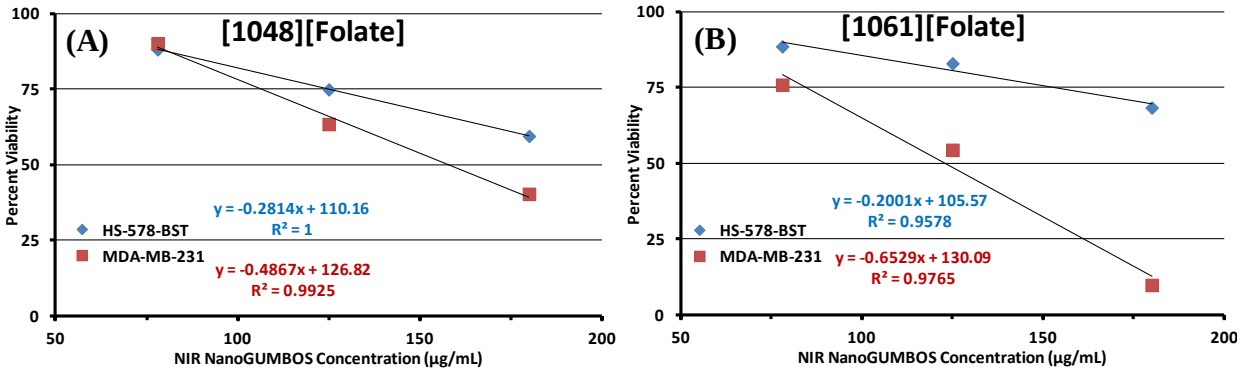


Figure 4.4 The LD_{50} was calculated from the linear slope of the cytotoxicity in different cell lines of NIR nanoGUMBOS.

4.4.3 Laser Irradiation Cytotoxicity

Since the late 19th century, it has been known that healthy cells are more robust than cancer cells in terms of extreme temperatures.[28, 33] Unfortunately for that time, the notion of robustness was merely a state of observation and not quantification. Irradiating cells was performed orthogonally to a 96 well-plate over a set time period. The cells were not influenced by NIR nanoGUMBOS in order to observe "cytotoxicity" from only the laser. Laser irradiation control supports the previous claims as the normal breast cells retained 93-95% viability after

continuous irradiation unlike the cancerous cells which decreased in viability (Figure 4.5). Cancer cells are more susceptible to heat due to disorganized cellular structure and functions.

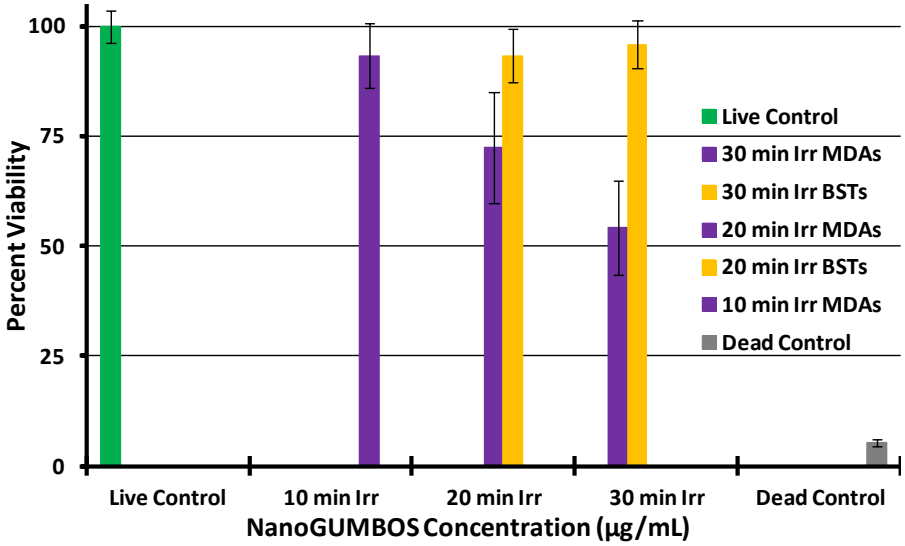


Figure 4.5 Laser irradiation over cancerous MDA-MB-231 (MDAs) and noncancerous HS-578-BST (BSTs) were observed.

4.4.4 Laser Irradiation Photothermal Response

There have been many different procedures in the literature on measuring photothermal response such as using a NIR thermal camera on brass plate,[34] confocal fluorescence thermal imaging in optofluidic device,[35] thermocouple in vacuum apparatus,[36] or thermocouple in a sealed cuvette.[37] In an effort to accurately record the photothermal generation towards a hyperthermal therapeutic, a glass NMR tube as the sample compartment was used to mimic the conditions cells would experience in a 96 well-plate. Recording hyperthermal generation proved difficult in a 96 well-plate due to the laser irradiating the thermocouple directly. The NIR nanoGUMBOS were irradiated in 100 µL modified DMEM media for 30 minutes while the thermocouple measured photothermal generation (Figure 4.6). NIR nanoGUMBOS concentrations for laser irradiation were a result of the viability critical concentrations: 77.6, 124.9, and 179.6 µg mL^{-1}.

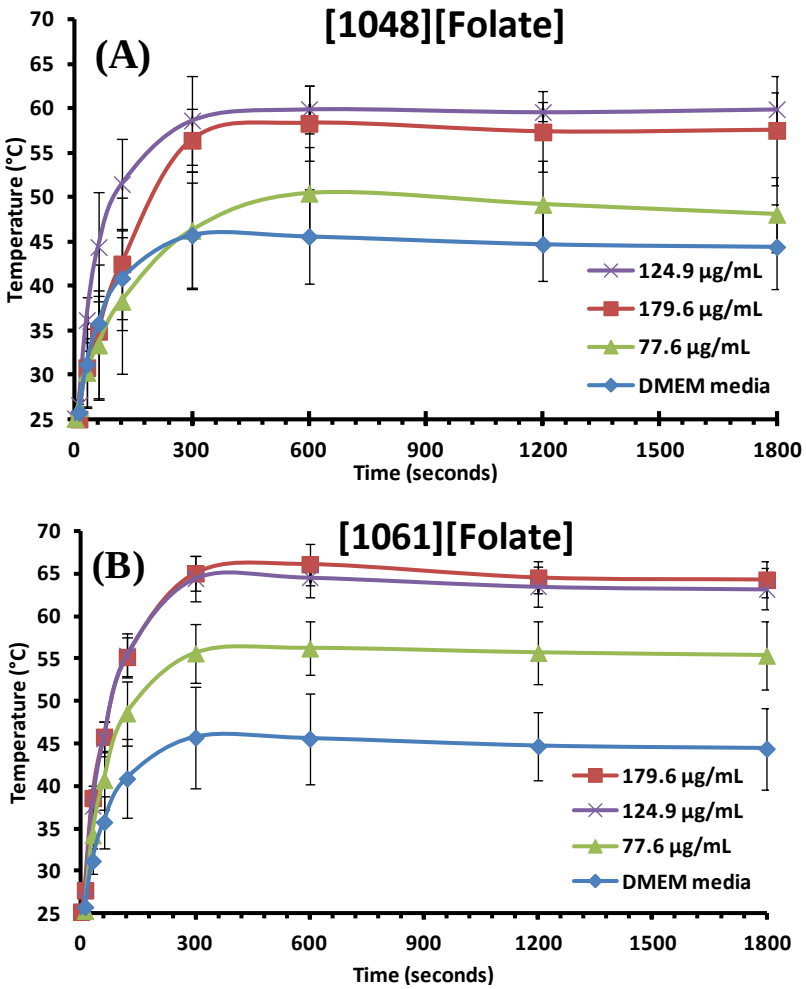


Figure 4.6 Substantial heat was generated from the NIR nanoGUMBOS (A) [1048][Folate] and (B) [1061][Folate].

The [1048][Folate] NIR nanoGUMBOS collectively reached a constant photothermal generation after 10 minutes of continuous irradiation. After 30 minutes of irradiation [1048][Folate] NIR nanoGUMBOS concentrations of 77.6, 124.9, and 179.6 µg mL^{-1} respectively heated to 48.1 ± 4.2, 59.9 ± 1.9, and 57.5 ± 6.2 °C. The [1061][Folate] NIR nanoGUMBOS achieving full photothermal potential after 5 minutes also generated more heat upon irradiation. The [1061][Folate] NIR nanoGUMBOS of concentrations 77.6, 124.9, and 179.6 µg mL^{-1} respectively heated to 55.4 ± 4.0, 63.2 ± 2.4, 64.3 ± 2.2 °C. The NIR nanoGUMBOS generate heat during the vibrational relaxations after excitation to the first excited singlet state.

4.4.5 Hyperthermia Cancer Therapeutic

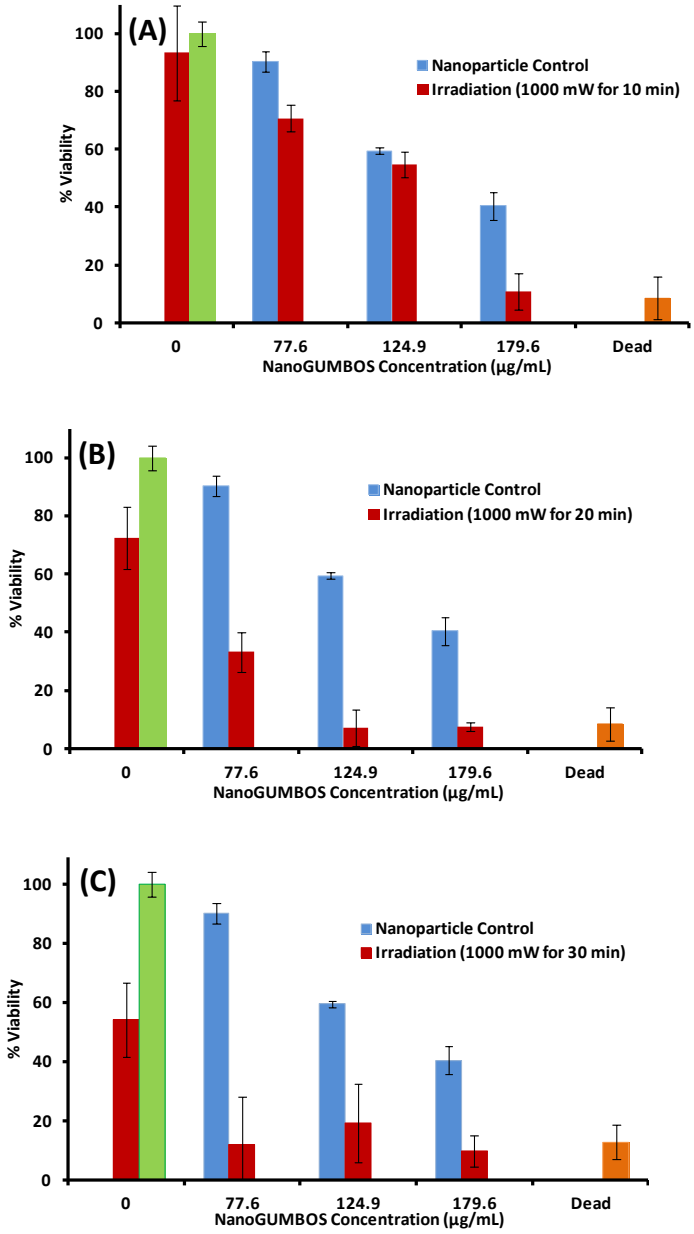


Figure 4.7 [1048][Folate] NIR nanoGUMBOS with MDA-MB-231 breast cancer cells shows live-green and dead-orange controls, nanoGUMBOS control-blue, and hyperthermal (laser and nanoGUMBOS)-red at (A) 10 minute, (B) 20 minute, and (C) 30 minute lasing time intervals.

The hyperthermal method was performed by orthogonally placing the laser 2.5 cm above the 96 well-plate and irradiating in time increments of 10, 20, and 30 minutes. After the MDA-MB-213 cells with NIR nanoGUMBOS were irradiated, it was concluded that the 77.6 µg mL^{-1}

concentration under irradiation for 20 – 30 minutes greatly kills tumor cells. Representative graphs further compare side-by-side difference in [1048][Folate] (Figure 4.7) and [1061][Folate] (Figure 4.8) nanoGUMBOS cytotoxicities, hyperthermia responses, and laser control toxicity with MDA-MB-231 cancer cells.

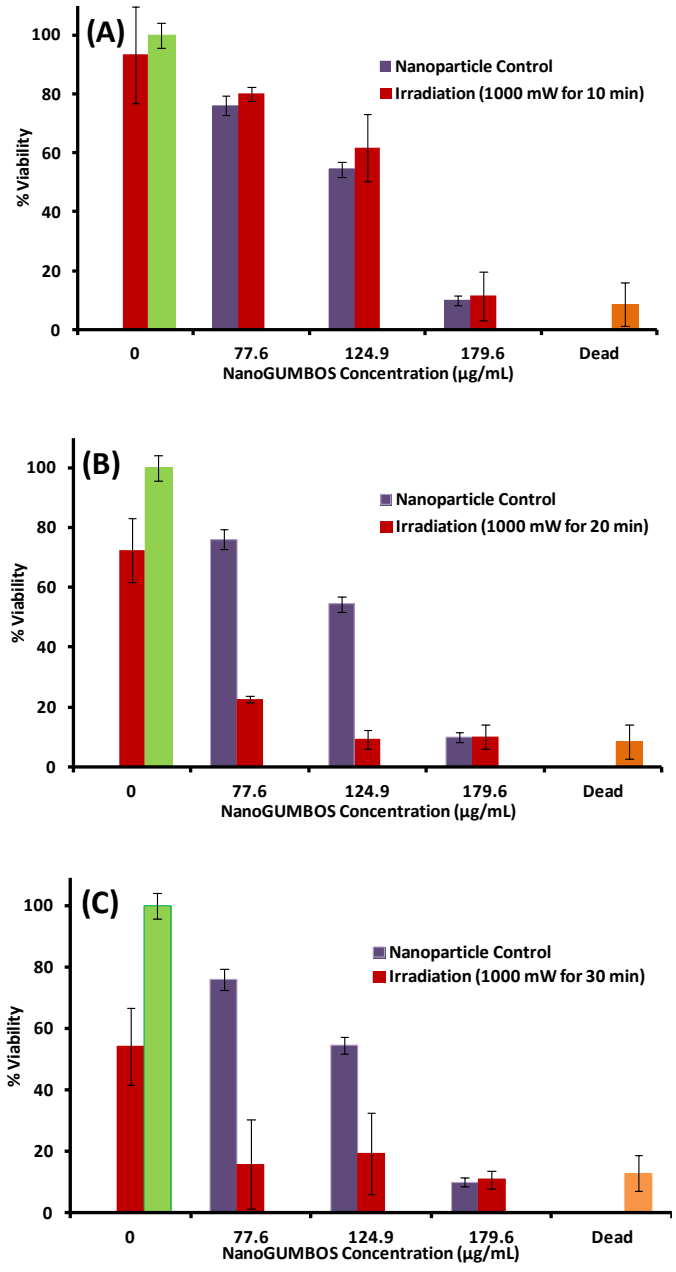


Figure 4.8 [1061][Folate] NIR nanoGUMBOS with MDA-MB-231 breast cancer cells shows live-green and dead-orange controls, nanoGUMBOS control-blue, and hyperthermal (laser and nanoGUMBOS)-red at (A) 10 minute, (B) 20 minute, and (C) 30 minute lasing time intervals.

The [1048][Folate] nanoGUMBOS in concert with NIR laser irradiation substantially killed cancerous cells. It was shown that with an increase in irradiation time and nanoGUMBOS concentration the percentage of cell death increased. The concentration of 77.6 μg mL^{-1} and 10, 20, and 30 minutes irradiation resulted in respective cell death percentages of 70.7, 33.2, and 12.0%. This concentration would be the ideal use since the nanoGUMBOS control yielded 90.2% cell viability.

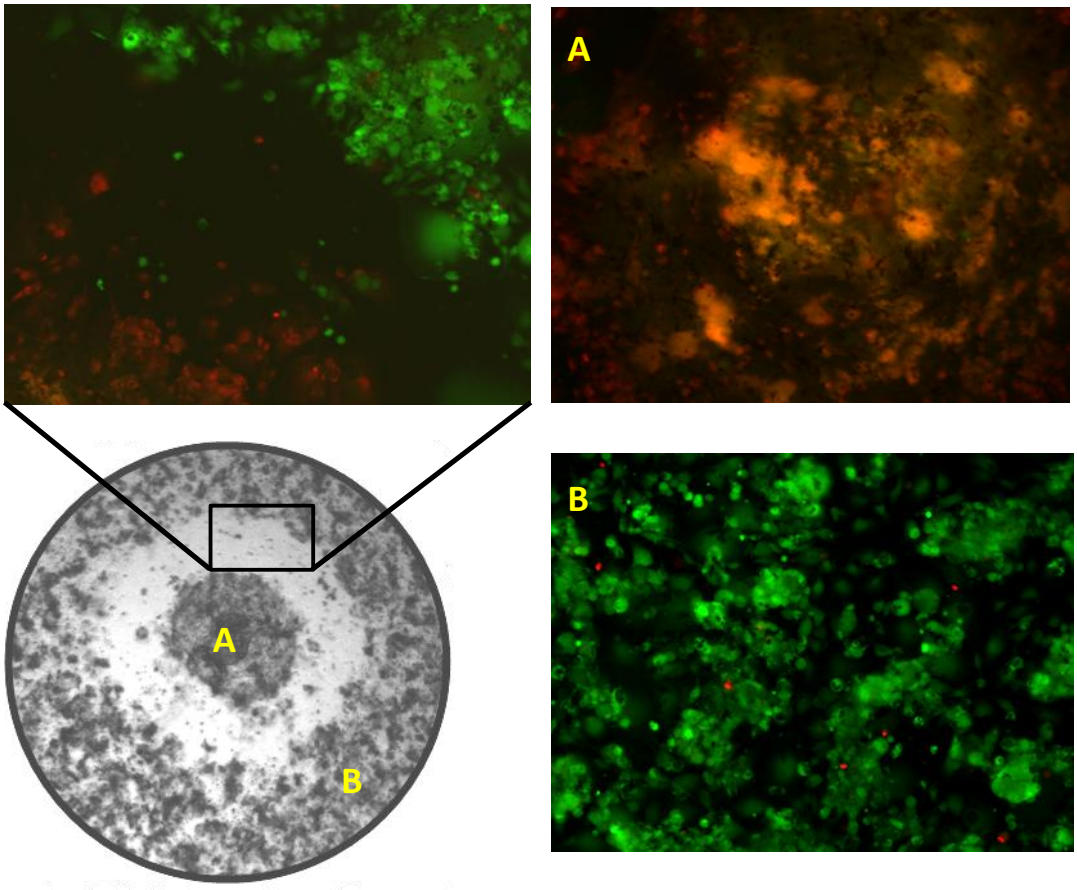


Figure 4.9 A fluorescence microscopy image distinctively shows cell death from the selective area where (A) laser irradiation occurred, (B) did not occur, and (inset) cusp of irradiation/nonirradiation. (Note: the diameter of the laser spot matches the laser focal spot in image, 2 mm.)

The [1061][Folate] nanoGUMBOS in concert with NIR laser irradiation substantially killed cancerous cells at a concentration of 77.6 μg mL^{-1}. This concentration with 10, 20, and 30

minute irradiation resulted in respective cell viabilities of 80.0, 22.6, and 19.2%. After 10 minutes of irradiation, the nanoGUMBOS control and nanoGUMBOS with irradiation resulted in similar cell death not specifying the contribution of the photothermal effects. However, 20 and 30 minutes irradiation clearly demonstrate the hyperthermal effects (Figure 4.9). The fluorescence microscopy image shows the selectivity of cell death when a NIR laser is irradiating cancerous breast cells that have incubated nanoGUMBOS. Cells that have died (red fluorescence) exhibited ablation resulting in fusion to the well-plate and leading to congregation of dead cells; however cells that have died, but not ablated became detached leaving a halo.

4.4.6 Cellular Uptake of NIR NanoGUMBOS

Based on previous literature, the folate molecule has been used for targeting cancerous cells allowing nanomaterials to enter cells via receptor-mediated endocytosis. Receptor-mediated endocytosis enters cells by attaching to the proper receptor invaginating nanomaterials in the cell interior. After performing the method (*vide supra*) for cellular uptake it was determined that only about 6% of the injected (77.6 μg mL^{-1}) entered the MDA-MB-231 cells (Table 4.3). Confirmation of the cellular uptake was performed by calculating the theoretical percent by comparing the absorbencies of a controlled 10% nanoGUMBOS dissolved in DMSO and samples, and the sample absorbance with the slope equation from the concentration gradient. The two respective values show a 96.9% and 92.2% agreement for [1048][Folate] and [1061][Folate], respectively, when performing the calculations.

Table 4.3 The percent of nanoGUMBOS were calculated by difference in absorbance from the control (10% dissolved in DMSO) and from the concentration gradient equation (%Slope).

NanoGUMBOS	Sample	Wavelength (nm)	Absorbance	%Overall Uptake	%Slope
[1048][FA]	Cells	1000	0.004986	6.34	6.15
	DMSO (10%)		0.007864		
[1061][FA]	Cells	1000	0.002146	5.64	6.12
	DMSO (10%)		0.003808		

4.5 Conclusion

The [1048][Folate] and [1061][Folate] NIR nanoGUMBOS successfully destroyed via hyperthermia the MDA-MB-231 breast cancer cells when photothermal generation was activated by 1064 nm NIR laser irradiation despite. NIR nanoGUMBOS without photothermal generation showed little toxicity to both cancerous and noncancerous (HS-578-BST) breast cells. While both NIR nanoGUMBOS were successful in killing cancer cells by hyperthermia, neither nanoGUMBOS were lesser effective in killing when irradiated for more than 20 minutes. These types of NIR nanoGUMBOS have thus demonstrated the applicability as a hyperthermal therapeutic towards cancer therapy.

4.6 References

1. American Cancer Society. Cancer Facts & Figures 2012. American Cancer Society: Atlanta, 2012.

2. Glazer, E. S.; Curley, S. A. The Ongoing History of Thermal Therapy for Cancer. *Surg. Oncol. Clin. N. Am.* **2011,** *20 (2)*, 229-235.

3. Kitture, R.; Ghosh, S.; Kulkarni, P.; Liu, X. L.; Maity, D.; Patil, S. I.; Jun, D.; Dushing, Y.; Laware, S. L.; Chopade, B. A.; Kale, S. N. Fe_3O_4-Citrate-Curcumin: Promising Conjugates for Superoxide Scavenging, Tumor Suppression and Cancer Hyperthermia. *J. Appl. Phys.* **2012,** *111 (6)*, 064702.

4. Kim, D. K.; Amin, M. S.; Elborai, S.; Lee, S. H.; Koseoglu, Y.; Muhammed, M. Energy Absorption of Superparamagnetic Iron Oxide Nanoparticles by Microwave Irradiation. *J. Appl. Phys.* **2005,** *97 (10)*, 10J510.

5. Bae, K. H.; Park, M.; Do, M. J.; Lee, N.; Ryu, J. H.; Kim, G. W.; Kim, C.; Park, T. G.; Hyeon, T. Chitosan Oligosaccharide-Stabilized Ferrimagnetic Iron Oxide Nanocubes for Magnetically Modulated Cancer Hyperthermia. *ACS Nano* **2012,** *6 (6)*, 5266-5273.

6. Su, Y. Y.; Wei, X. P.; Peng, F.; Zhong, Y. L.; Lu, Y. M.; Su, S.; Xu, T. T.; Lee, S. T.; He, Y. Gold Nanoparticles-Decorated Silicon Nanowires as Highly Efficient Near-Infrared Hyperthermia Agents for Cancer Cells Destruction. *Nano Lett.* **2012,** *12 (4)*, 1845-1850.

7. Huang, X. H.; El-Sayed, I. H.; Qian, W.; El-Sayed, M. A. Cancer Cell Imaging and Photothermal Therapy in the Near-Infrared Region by Using Gold Nanorods. *J. Am. Chem. Soc.* **2006,** *128 (6)*, 2115-2120.

8. Hirsch, L. R.; Stafford, R. J.; Bankson, J. A.; Sershen, S. R.; Rivera, B.; Price, R. E.; Hazle, J. D.; Halas, N. J.; West, J. L. Nanoshell-Mediated Near-Infrared Thermal Therapy of Tumors Under Magnetic Resonance Guidance. *Proc. Natl. Acad. Sci. USA* **2003,** *100 (23)*, 13549-13554.

9. Lal, S.; Clare, S. E.; Halas, N. J. Nanoshell-Enabled Photothermal Cancer Therapy: Impending Clinical Impact. *Acc. Chem. Res.* **2008,** *41 (12)*, 1842-1851.

10. Huang, H. W.; Liauh, C. T. Review: Therapeutical Applications of Heat in Cancer Therapy. *J. Med. Biol. Eng.* **2012,** *32 (1)*, 1-10.

11. Bashkatov, A. N.; Genina, E. A.; Kochubey, V. I.; Tuchin, V. V. Optical Properties of Human Skin, Subcutaneous and Mucous Tissues in the Wavelength Range from 400 to 2000 nm. *J. Phys. D: Appl. Phys.* **2005,** *38 (15)*, 2543-2555.

12. Bhattacharya, D.; Das, M.; Mishra, D.; Banerjee, I.; Sahu, S. K.; Maiti, T. K.; Pramanik, P. Folate Receptor Targeted, Carboxymethyl Chitosan Functionalized Iron Oxide Nanoparticles: A Novel Ultradispersed Nanoconjugates for Bimodal Imaging. *Nanoscale* **2011,** *3 (4)*, 1653-1662.

13. van Dam, G. M.; Themelis, G.; Crane, L. M. A.; Harlaar, N. J.; Pleijhuis, R. G.; Kelder, W.; Sarantopoulos, A.; de Jong, J. S.; Arts, H. J. G.; van der Zee, A. G. J.; Bart, J.; Low, P. S.; Ntziachristos, V. Intraoperative Tumor-Specific Fluorescence Imaging in Ovarian Cancer by Folate Receptor-Alpha Targeting: First In-Human Results. *Nat. Med.* **2011,** *17 (10)*, 1315-U1202.

14. Rosen, J. E.; Chan, L.; Shieh, D. B.; Gu, F. X. Iron Oxide Nanoparticles for Targeted Cancer Imaging and Diagnostics. *Nanomed. Nanotechnol. Biol. Med.* **2012,** *8 (3)*, 275-290.

15. Liong, M.; Lu, J.; Kovochich, M.; Xia, T.; Ruehm, S. G.; Nel, A. E.; Tamanoi, F.; Zink, J. I. Multifunctional Inorganic Nanoparticles for Imaging, Targeting, and Drug Delivery. *ACS Nano* **2008,** *2 (5)*, 889-896.

16. Bwambok, D. K.; El-Zahab, B.; Challa, S. K.; Li, M.; Chandler, L.; Baker, G. A.; Warner, I. M. Near-Infrared Fluorescent NanoGUMBOS for Biomedical Imaging. *ACS Nano* **2009,** *3 (12)*, 3854-3860.

17. de Rooy, S. L.; El-Zahab, B.; Li, M.; Das, S.; Broering, E.; Chandler, L.; Warner, I. M. Fluorescent One-Dimensional Nanostructures from a Group of Uniform Materials Based on Organic Salts. *Chem. Commun.* **2011,** *47 (31)*, 8916-8918.

18. Bwambok, D. K.; Challa, S. K.; Lowry, M.; Warner, I. M. Amino Acid-Based Fluorescent Chiral Ionic Liquid for Enantiomeric Recognition. *Anal. Chem.* **2010,** *82 (12)*, 5028-5037.

19. Li, M.; Ganea, G. M.; Lu, C. F.; De Rooy, S. L.; El-Zahab, B.; Fernand, V. E.; Jin, R. Y.; Aggarwal, S.; Warner, I. M. Lipophilic Phosphonium-Lanthanide Compounds with Magnetic, Luminescent, and Tumor Targeting Properties. *J. Inorg. Biochem.* **2012,** *107 (1)*, 40-46.

20. Tesfai, A.; El-Zahab, B.; Kelley, A. T.; Li, M.; Garno, J. C.; Baker, G. A.; Warner, I. M. Magnetic and Nonmagnetic Nanoparticles from a Group of Uniform Materials Based on Organic Salts. *ACS Nano* **2009,** *3 (10)*, 3244-3250.

21. Li, M.; De Rooy, S. L.; Bwambok, D. K.; El-Zahab, B.; DiTusa, J. F.; Warner, I. M. Magnetic Chiral Ionic Liquids Derived from Amino Acids. *Chem. Commun.* **2009,** *(45)*, 6922-6924.

22. de Rooy, S. L.; Li, M.; Bwambok, D. K.; El-Zahab, B.; Challa, S.; Warner, I. M. Ephedrinium-Based Protic Chiral Ionic Liquids for Enantiomeric Recognition. *Chirality* **2011,** *23 (1)*, 54-62.

23. Cole, M. R.; Li, M.; El-Zahab, B.; Janes, M. E.; Hayes, D.; Warner, I. M. Design, Synthesis, and Biological Evaluation of beta-Lactam Antibiotic-Based Imidazolium- and Pyridinium-Type Ionic Liquids. *Chem. Biol. Drug Des.* **2011,** *78 (1)*, 33-41.

24. Jordan, A. N.; Das, S.; Siraj, N.; de Rooy, S. L.; Li, M.; El-Zahab, B.; Chandler, L.; Baker, G. A.; Warner, I. M. Anion-Controlled Morphologies and Spectral Features of Cyanine-Based NanoGUMBOS - An Improved Photosensitizer. *Nanoscale* **2012,** *4 (16)*, 5031-5038.

25. Regmi, B. P.; Monk, J.; El-Zahab, B.; Das, S.; Hung, F. R.; Hayes, D. J.; Warner, I. M. A Novel Composite Film for Detection and Molecular Weight Determination of Organic Vapors. *J. Mater. Chem.* **2012,** *22 (27)*, 13732-13741.

26. Kumar, A.; Ma, H. L.; Zhang, X.; Huang, K. Y.; Jin, S. B.; Liu, J.; Wei, T.; Cao, W. P.; Zou, G. Z.; Liang, X. J. Gold Nanoparticles Functionalized with Therapeutic and Targeted Peptides for Cancer Treatment. *Biomaterials* **2012,** *33 (4)*, 1180-1189.

27. Oo, M. K. K.; Yang, Y. M.; Hu, Y.; Gomez, M.; Du, H.; Wang, H. J. Gold Nanoparticle-Enhanced and Size-Dependent Generation of Reactive Oxygen Species from Protoporphyrin IX. *ACS Nano* **2012,** *6 (3)*, 1939-1947.

28. Byrne, J. A Digest of 20 Years' Experience in the Treatment of Cancer of the Uterus by Galvanocautery. *Am. J. Obstet. Gynecol.* **1899,** *22*, 1052.

29. Whitrow, M. Wagner-Jauregg and Fever Therapy. *Med. Hist.* **1990,** *34 (3)*, 294-310.

30. Kennedy, L. C.; Bickford, L. R.; Lewinski, N. A.; Coughlin, A. J.; Hu, Y.; Day, E. S.; West, J. L.; Drezek, R. A. A New Era for Cancer Treatment: Gold-Nanoparticle-Mediated Thermal Therapies. *Small* **2011,** *7 (2)*, 169-183.

31. Khlebtsov, B. N.; Panfilova, E. V.; Terentyuk, G. S.; Maksimova, I. L.; Ivanov, A. V.; Khlebtsov, N. G. Plasmonic Nanopowders for Photothermal Therapy of Tumors. *Langmuir* **2012,** *28 (24)*, 8994-9002.

32. Liu, H. Y.; Liu, T. L.; Wu, X. L.; Li, L. L.; Tan, L. F.; Chen, D.; Tang, F. Q. Targeting Gold Nanoshells on Silica Nanorattles: a Drug Cocktail to Fight Breast Tumors via a Single Irradiation with Near-Infrared Laser Light. *Adv. Mater.* **2012,** *24 (6)*, 755-761.

33. Loeb, L. Further Investigations in Transplantation of Tumors. *J. Med. Res.* **1902,** *8 (1)*, 44-73.

34. Boldor, D.; Gerbo, N. M.; Monroe, W. T.; Palmer, J. H.; Li, Z. R.; Biris, A. S. Temperature Measurement of Carbon Nanotubes Using Infrared Thermography. *Chem. Mater.* **2008,** *20 (12)*, 4011-4016.

35. Choudhury, D.; Jaque, D.; Rodenas, A.; Ramsay, W. T.; Paterson, L.; Kar, A. K. Quantum Dot Enabled Thermal Imaging of Optofluidic Devices. *Lab Chip* **2012,** *12 (13)*, 2414-2420.

36. Cole, J. R.; Mirin, N. A.; Knight, M. W.; Goodrich, G. P.; Halas, N. J. Photothermal Efficiencies of Nanoshells and Nanorods for Clinical Therapeutic Applications. *J. Phys. Chem. C* **2009,** *113 (28)*, 12090-12094.

37. Ghosh, S.; Dutta, S.; Gomes, E.; Carroll, D.; D'Agostino, R.; Olson, J.; Guthold, M.; Gmeiner, W. H. Increased Heating Efficiency and Selective Thermal Ablation of Malignant Tissue with DNA-Encased Multiwalled Carbon Nanotubes. *ACS Nano* **2009,** *3 (9)*, 2667-2673.

Chapter 5. Conclusion and Future Studies

5.1 Concluding Remarks

GUMBOS and nanoGUMBOS have great promise towards a facile fabrication of task-specific materials. This monograph exemplified just a minute fraction of the possibilities that GUMBOS can perform, such as lanthanide-based luminescent nanoGUMBOS and photothermal NIR nanoGUMBOS as a hyperthermal cancer therapeutic.

Lanthanide nanoGUMBOS luminescence had high intensity at 613 nm as GUMBOS dissolved in ethanol. However, the lanthanide luminescence intensity decreased as nanoGUMBOS due to quenching from the imidazolium cation fluorescence at 420 nm. The imidazolium cation contributed to FRET when dissolved, but as nanoGUMBOS the imidazolium produced fluorescence. In addition to the luminescent spectrum, this was supported by energy transfer efficiency of GUMBOS having higher efficiency verses the nanoGUMBOS at 65.7% and 7.48%, respectively.

NanoGUMBOS were also synthesized with NIR cations (i.e. [1048] and [1061]) and biocompatible anions (i.e. [Ascorbate], [Deoxycholate], and [Folate]). While the anions, [Ascorbate] and [Deoxycholate], were used to demonstrate the feasibility of photothermal efficiency; the [Folate] anion was used as a hyperthermal cancer therapeutic towards the destruction of breast cancer. The formerly mentioned anions were found to be generous in efficiently converting laser irradiation to thermal generation. A trend shows nanoGUMBOS having [1048] cation and nanoGUMBOS having [Ascorbate] anion being more efficient in converting light to heat than [1061] cation and [Deoxycholate] anions, respectively.

NIR nanoGUMBOS were used towards breast cancer therapy by hyperthermal methods was used. Capable of reaching temperatures around 60 °C, NIR nanoGUMBOS successfully

destroyed cancer cells without cytotoxicity prior to laser irradiation. Concentrations of 77.6 μg mL^{-1} NIR nanoGUMBOS and 20 minutes irradiation yielded cell death equivalent to the dead control.

Throughout history there have been many giant leaps in scientific research that has advanced current research from tasting molten salts to light amplification by stimulated emission to manipulating molecules to perform work. NanoGUMBOS exemplify material that is easily tunable for a task-specific application opposed to solely being used as a solvent.

5.2 Future Studies

Organic light emitting diodes (OLED) have become of great interest since an intense green emission from aluminum tris(8-hydroxyquinolinate) in 1987. It was not long before OLED research used lanthanide complexes. In 1990, a terbium (III) tris(acetylacetonate) complex was used as the emissive layer. A basic single-layer OLED device is made up of three main components: an anode (e.g. Indium Tin Oxide), organic emitting compound, and a cathode (e.g. Ca, Mg, or Al). Multiple-layer OLED devices employ electron and/or hole transport media such as 2-(4-biphenyl)-5-(4-*tert*-butylphenyl)-1,3,4-oxadiazole and *N*,*N*-diphenyl-*N*,*N'*-bis(3-methylphenyl)-[1,1'-biphenyl]-4,4'-diamine, respectively. These electron transports correspond to the conduction band (LUMO), while hole transports correspond to the valence band (HOMO). Due to the ability to combine properties using GUMBOS, it would be interesting to use an electron or hole transport cation with the previously designed lanthanide anion.

Electron transport molecules that would be synthesized into a cation would be bathocuproine due to its efficient electron injection thus giving higher quantum efficiency. The europium (III) tetra(beta-diketonate) would be the acting emissive layer and anion. These

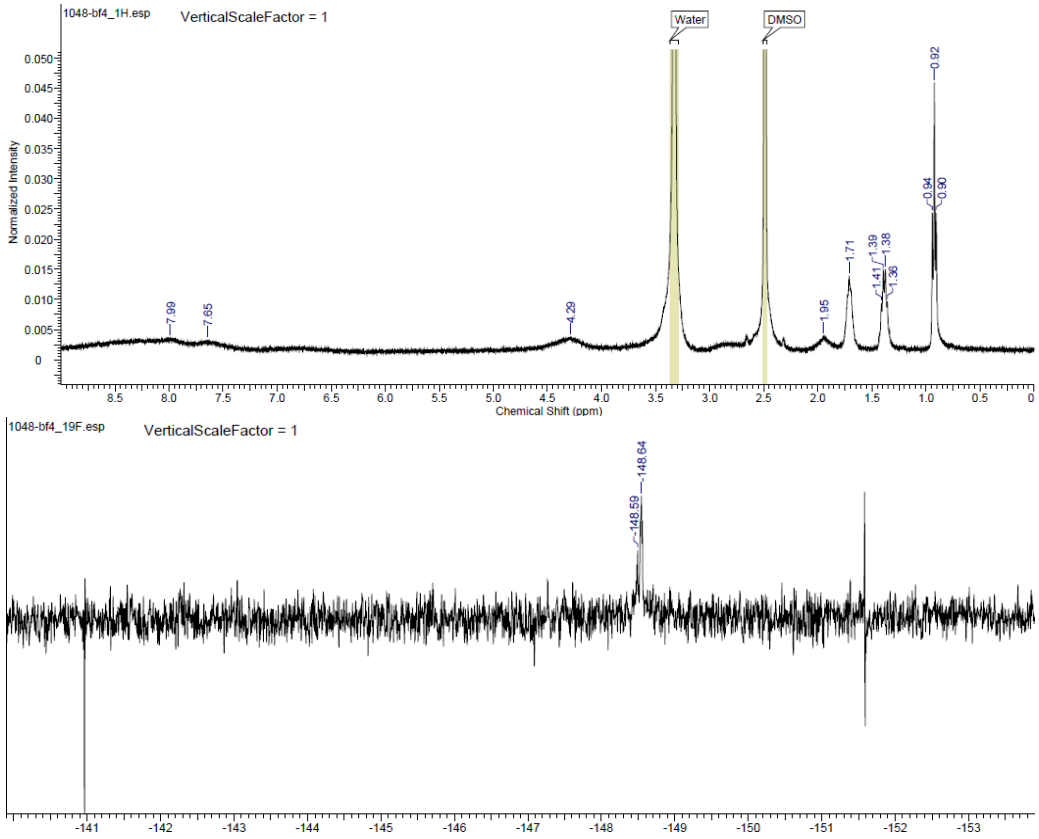
lanthanide nanoGUMBOS would have a greater surface area which would result in more intense radiative emissions from the europium.

There have been many types of nanomaterials employed for hyperthermal cancer therapeutics that have used *in vivo* mouse models to demonstrate the success of tumor reduction. It would be paramount for the NIR hyperthermal nanoGUMBOS effectiveness to be studied using SCID (severe combined immunodeficiency) mice with artificially grown MDA-MB-231 cancer tumors. The study would include the three studied concentrations from the *in vitro* studies (77.6, 124.9, and 179.6 μg mL^{-1} per 0.1 cm^3 of the tumor). The tumor would be measured pre-nanoGUMBOS injection for its volume followed by the corresponding injection of NIR nanoGUMBOS. Laser irradiation would be set at 1000 mW and use a continuous irradiation for 10, 20, and 30 minutes. The mice tumors would be studies using NIR nanoGUMBOS controls, NIR laser irradiation controls, and a combined study.

Appendix 1. Supplemental Information for Chapter 3

Chapter 3 - Photothermal Response of Near-Infrared NanoGUMBOS

A.) [1048][BF_4]



B.) [1048][Deoxycholate]

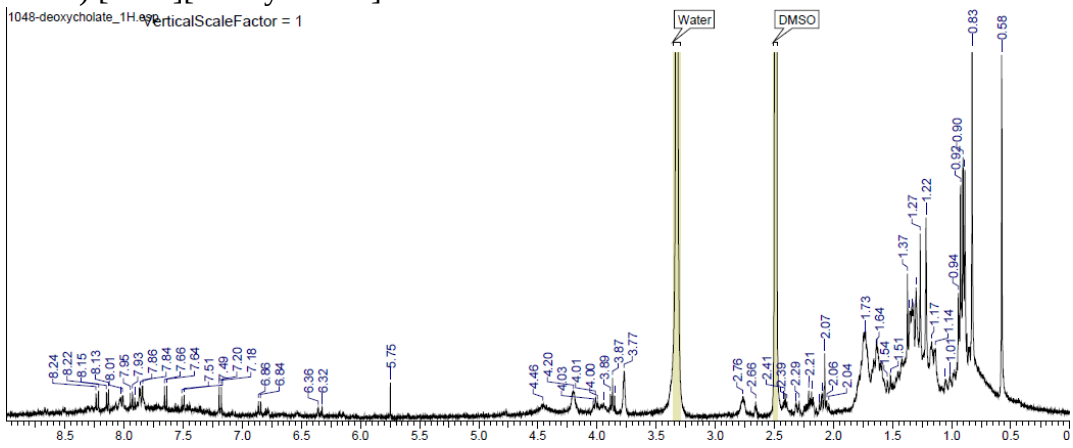
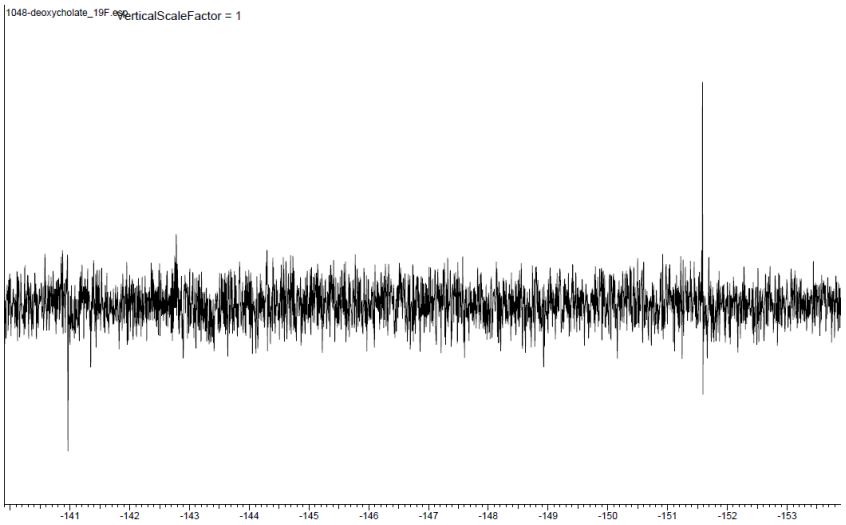


Figure A3.1 ^{1}H and ^{19}F NMR of the GUMBOS in d-DMSO.



C.) [1048][Ascorbate]

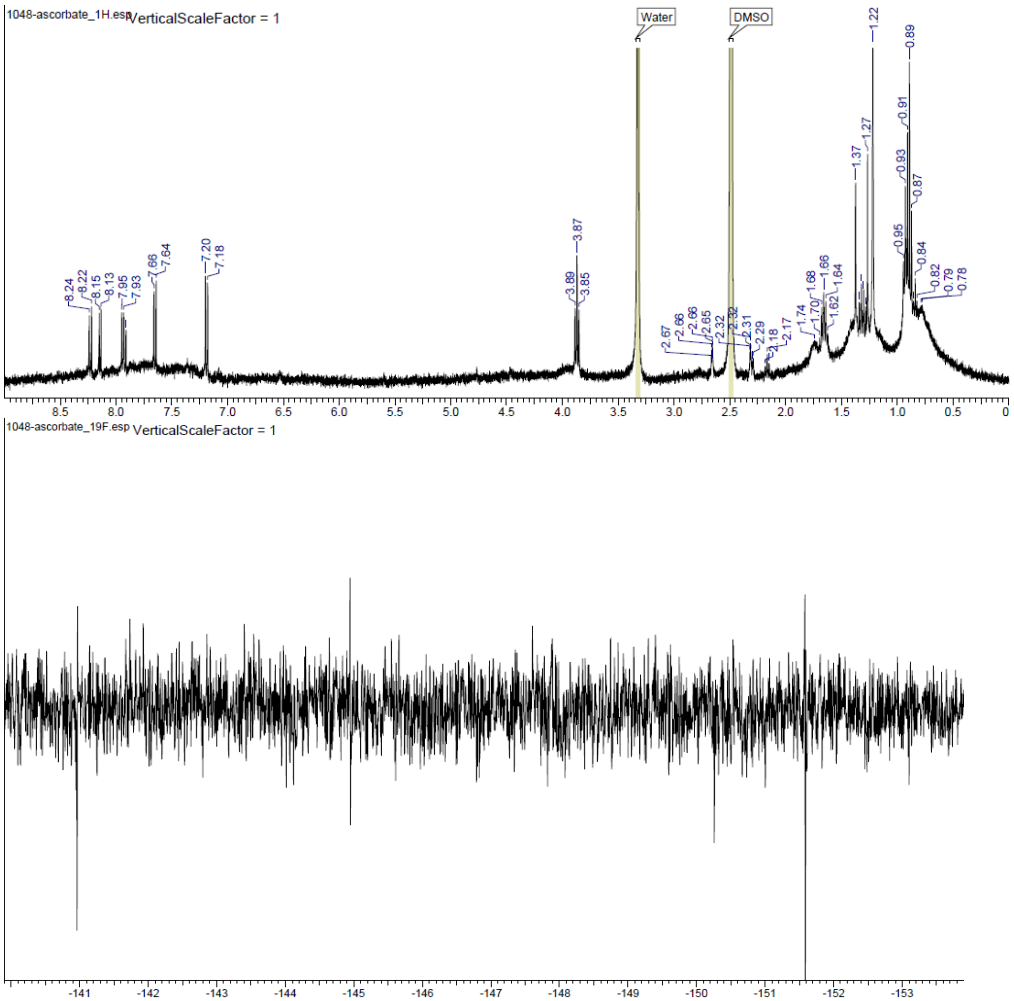
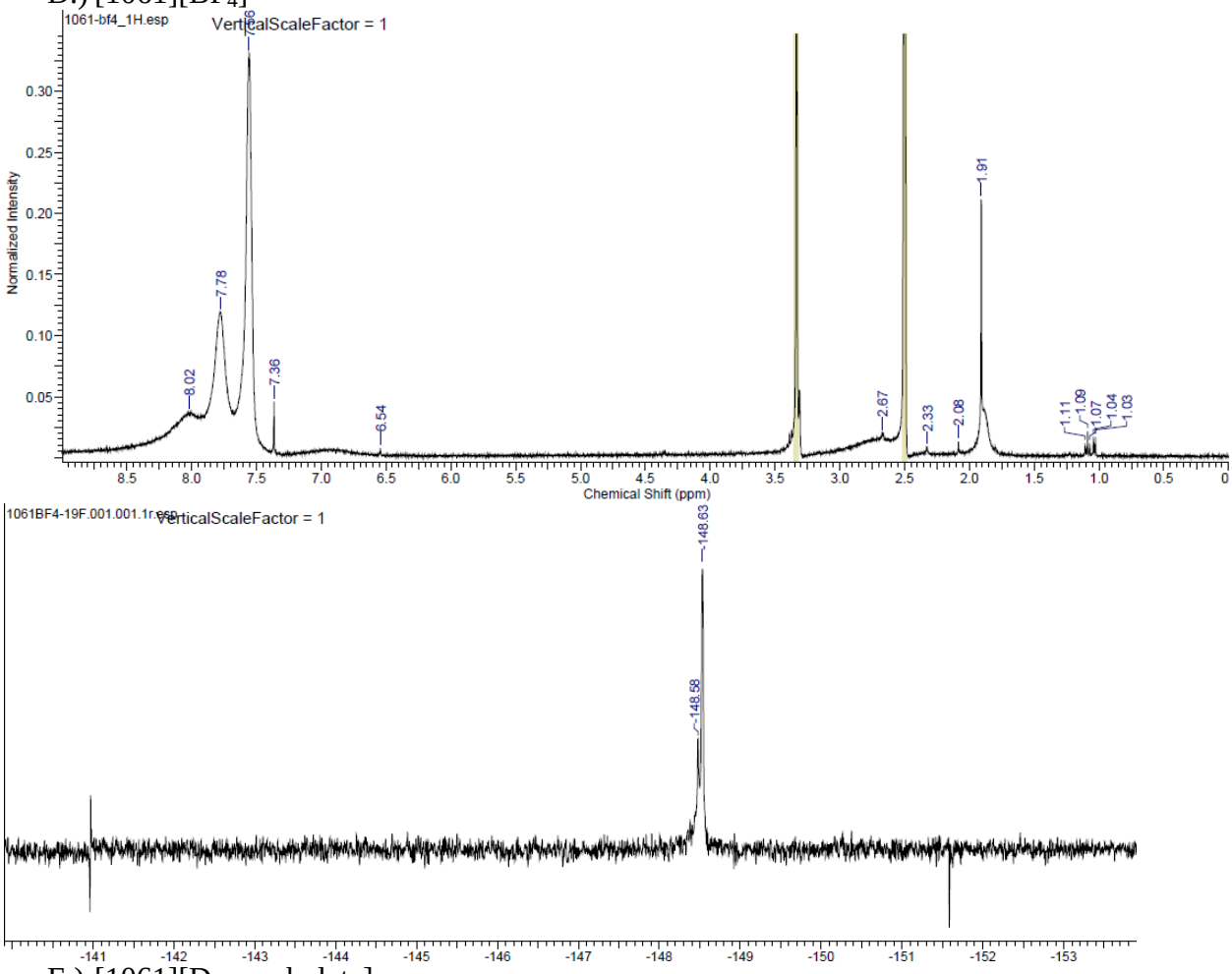


Figure A3.1 *Continued.*

D.) [1061][BF_4]



E.) [1061][Deoxycholate]

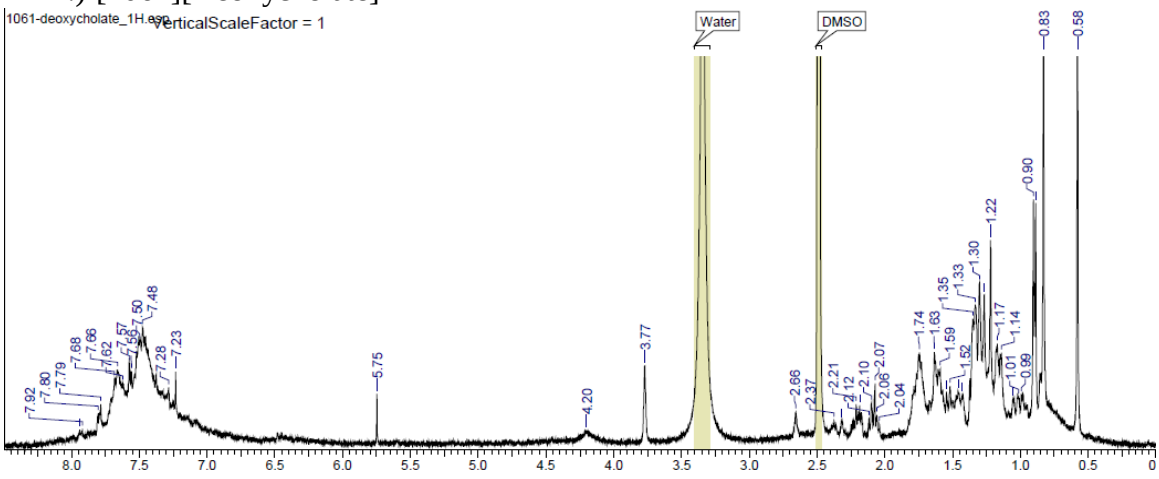
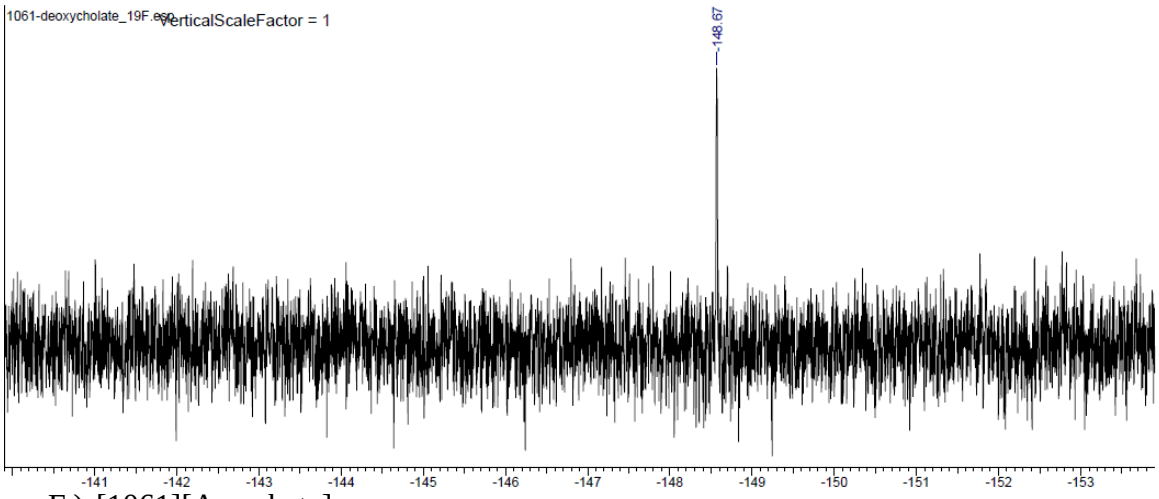


Figure A3.1 *Continued.*



F.) [1061][Ascorbate]

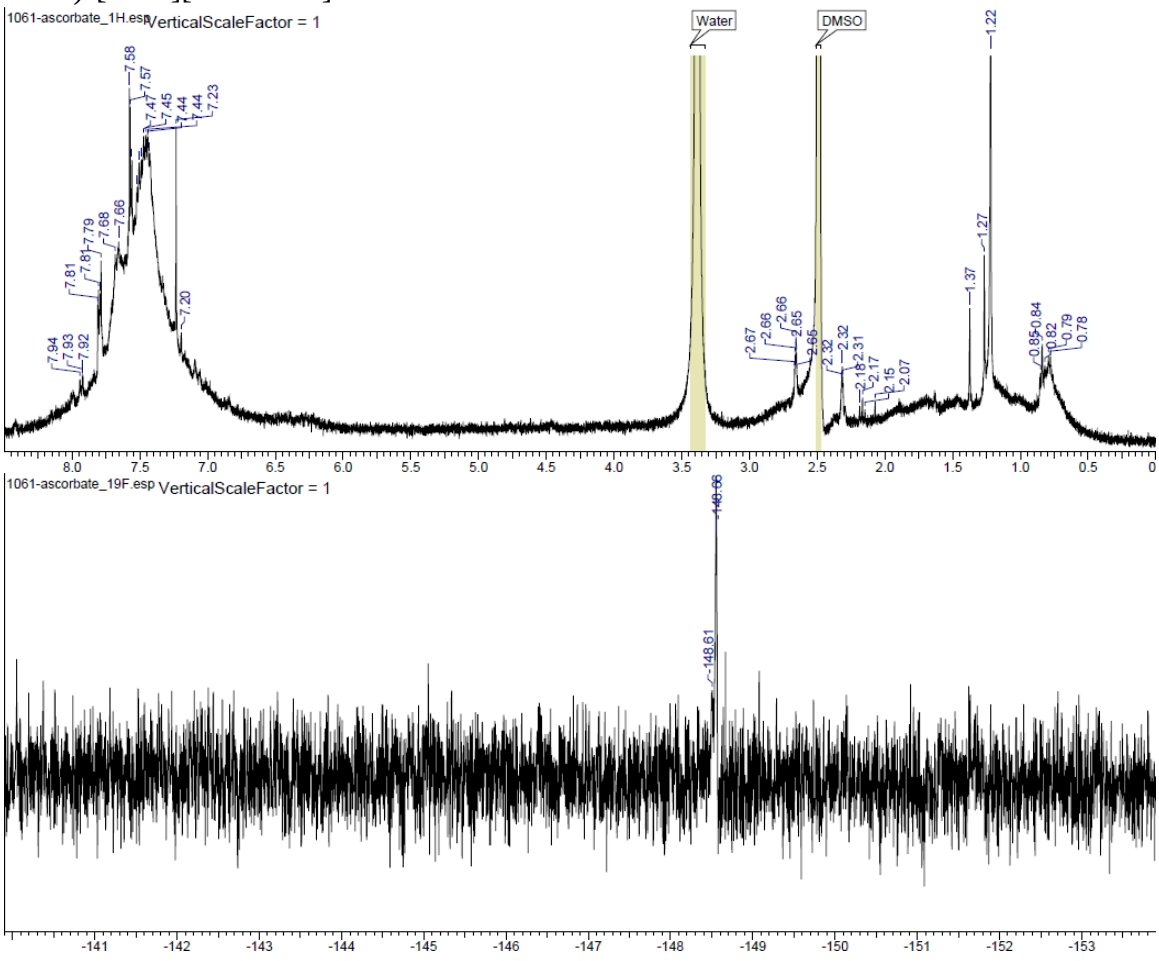
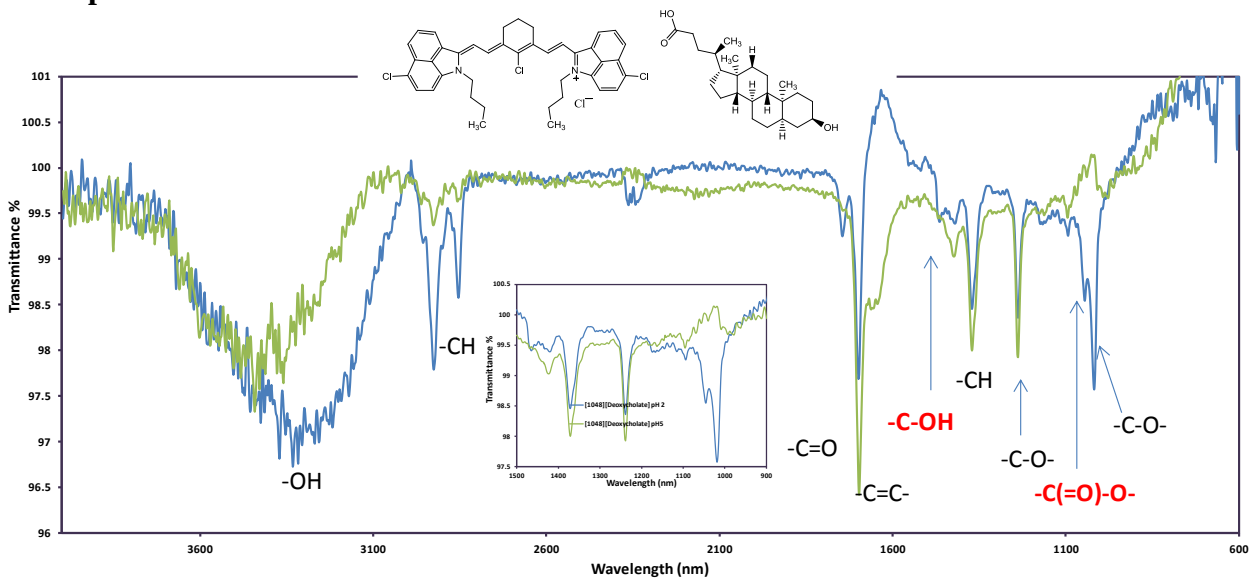


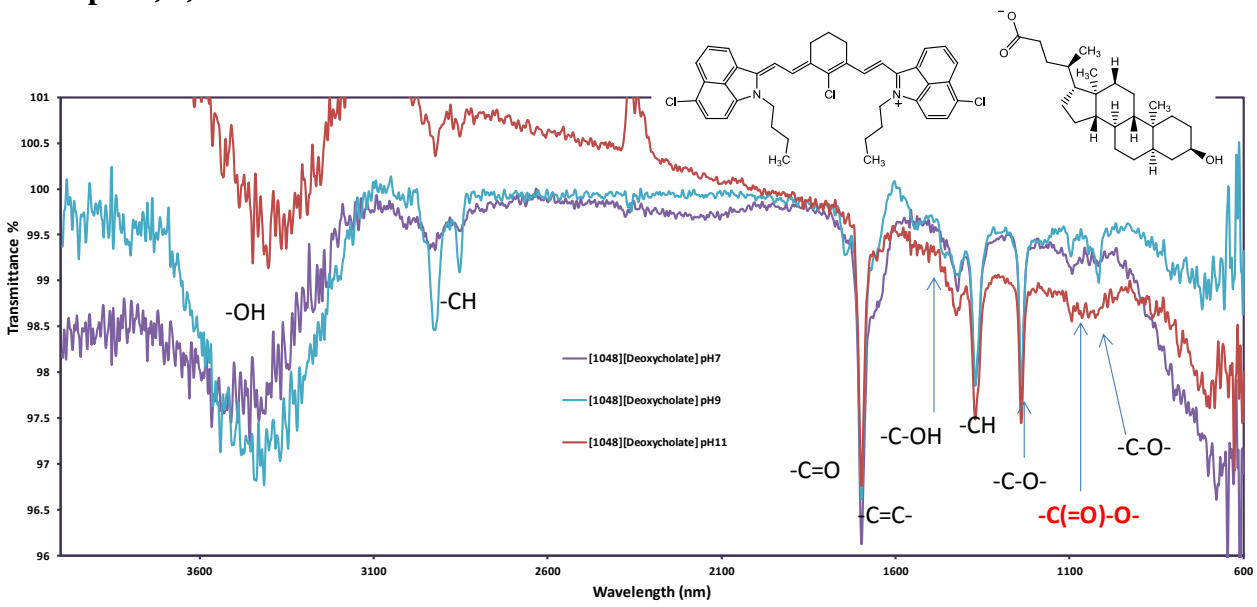
Figure A3.1 *Continued.*

A.) [1048][Deoxycholate]

pH 2 & 5



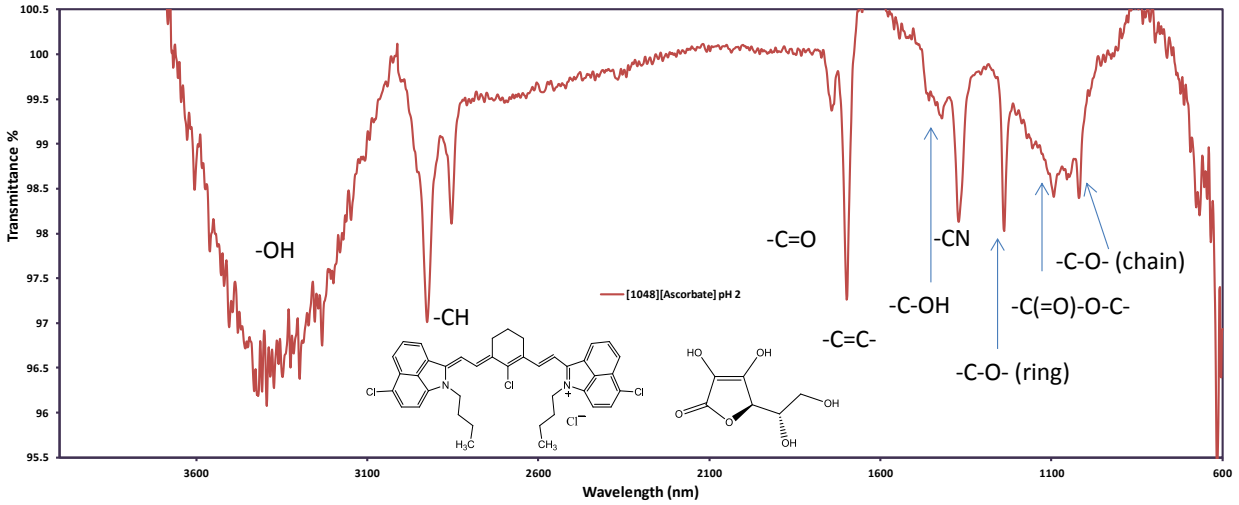
pH 7, 9, & 11



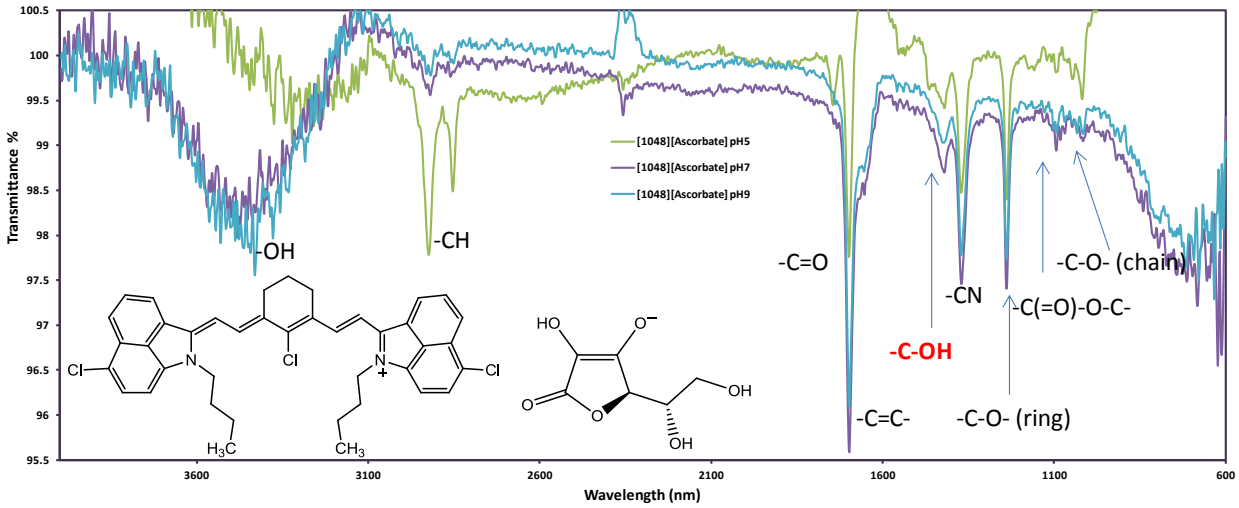
B.) [1048][Ascorbate]

pH 2

Figure A3.2 FT-IR of the nanoGUMBOS synthesized in different pH media suggests that the material is deprotonated with an increasing pH media.



pH 5, 7, & 9



pH 11

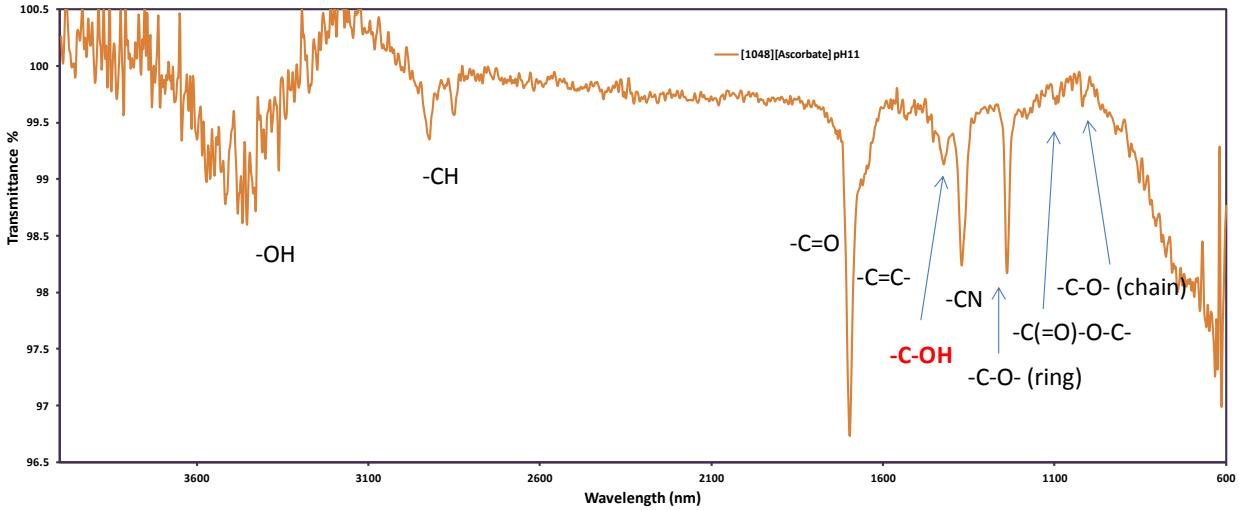
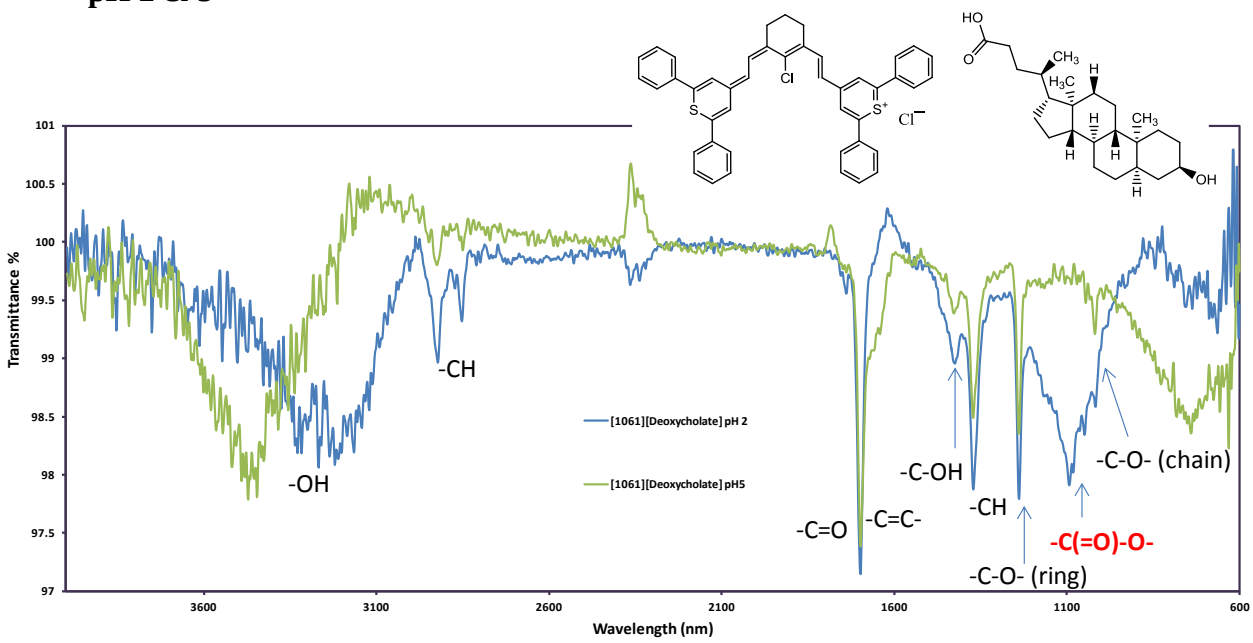


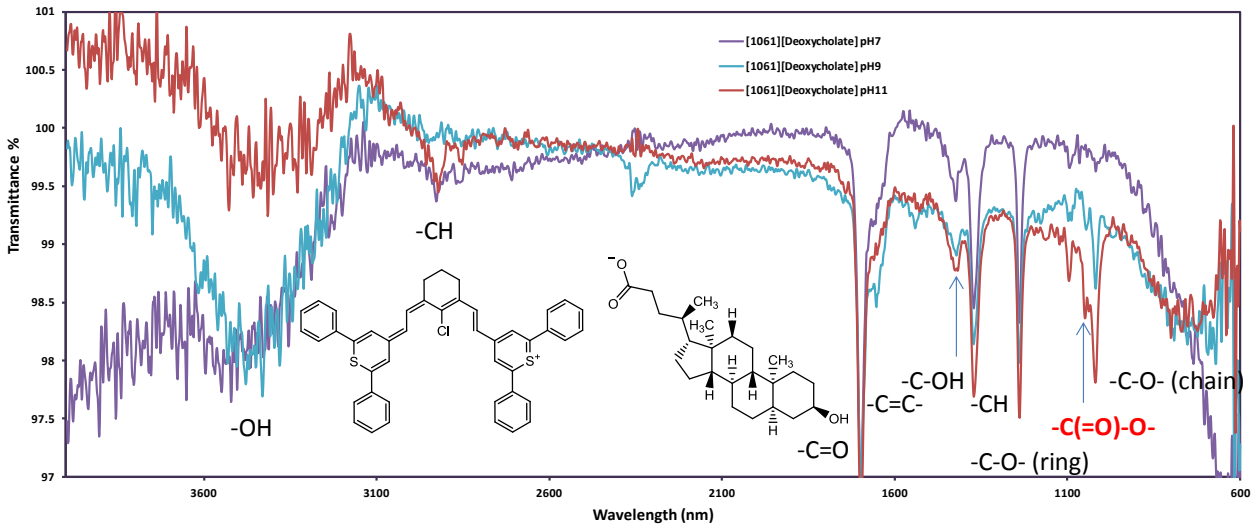
Figure A3.2 *Continued.*

C.) [1061][Deoxycholate]

pH 2 & 5



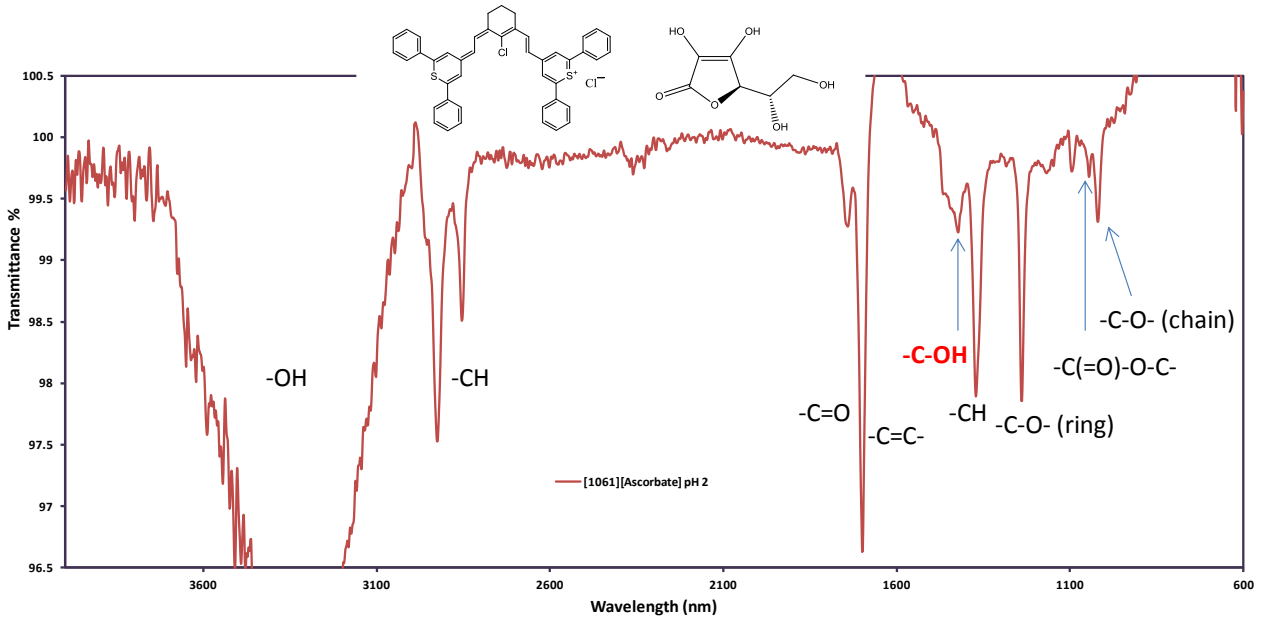
pH 7, 9, & 11



D.) [1061][Ascorbate]

pH 2

Figure A3.2 *Continued.*



pH 5, 7, and 9

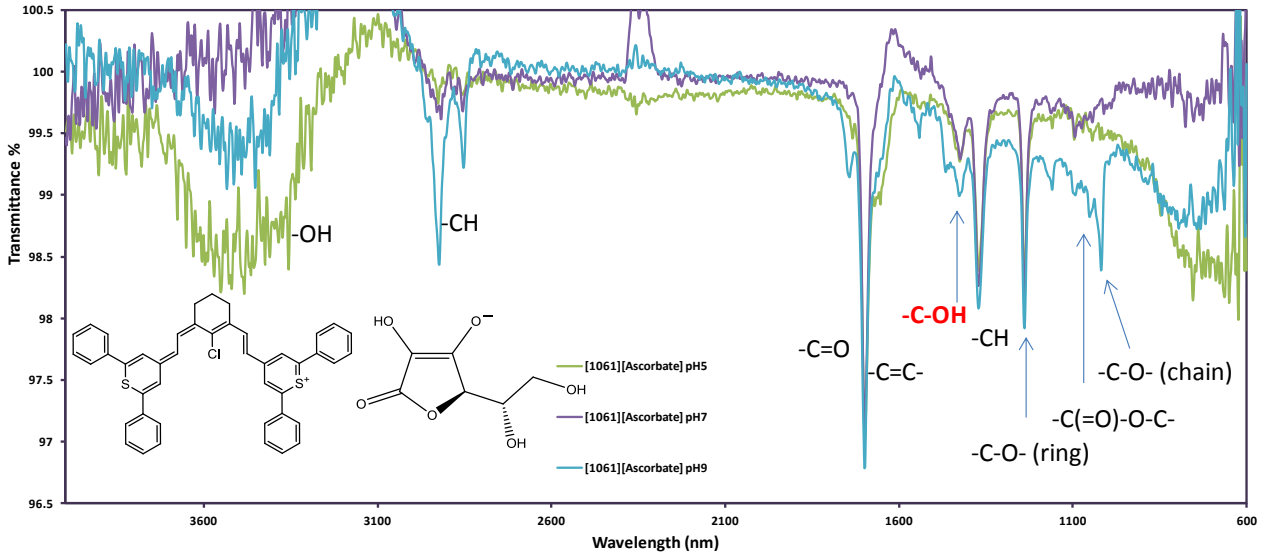


Figure A3.2 *Continued.*

pH 11

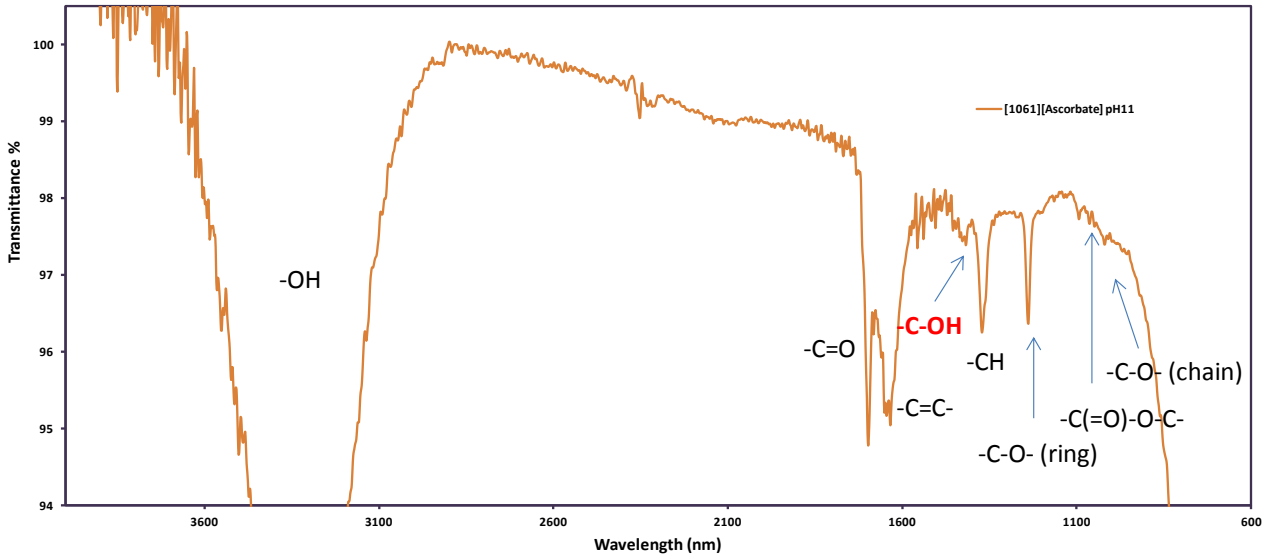


Figure A3.2 *Continued.*

Appendix 2. Supplemental Information for Chapter 4

Chapter 4 - Tumor-Targeting Hyperthermal Near-Infrared NanoGUMBOS

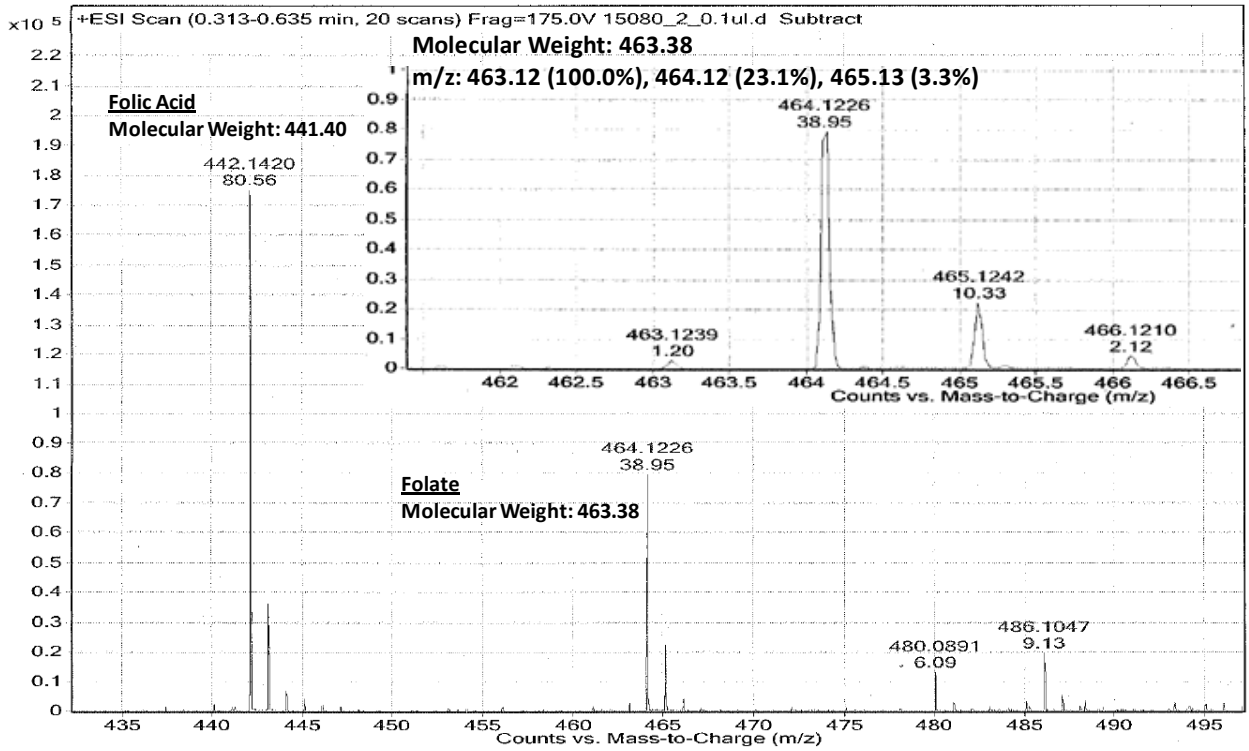


Figure A4.1 ESI MS of the folate product after synthesis reveals that the folic acid precursor is higher in concentration by two fold. (The inset is a scan on only the folate.)

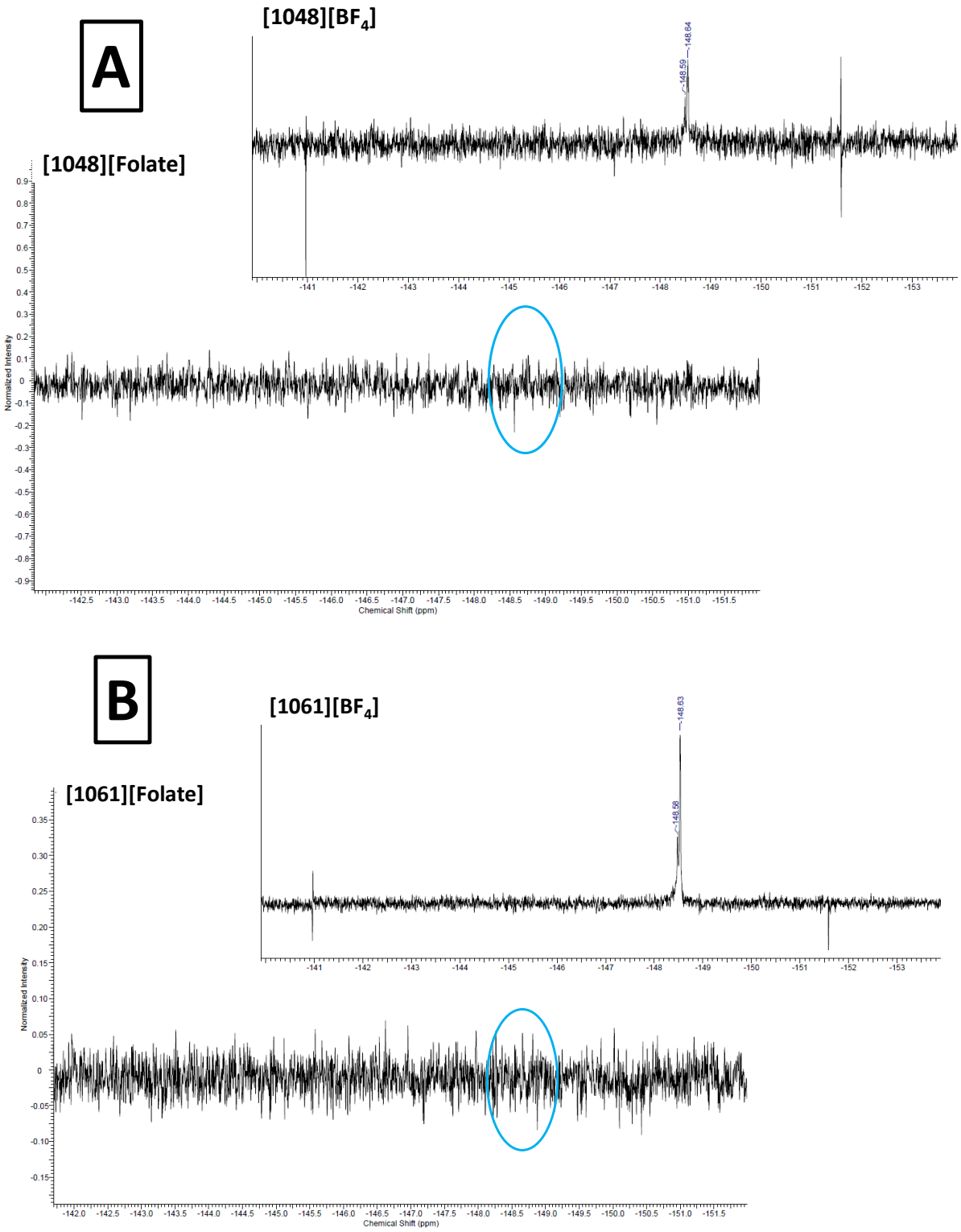


Figure A4.2 ^{19}F NMR was used to observe the anion exchange from the anion precursor [BF_4] to non-fluorinated product [Folate] for the (A) [1048] and (B) [1061] GUMBOS.



Figure A4.3 Photothermal measurements were recorded by a thermocouple placed about 2 mm above the laser beam.

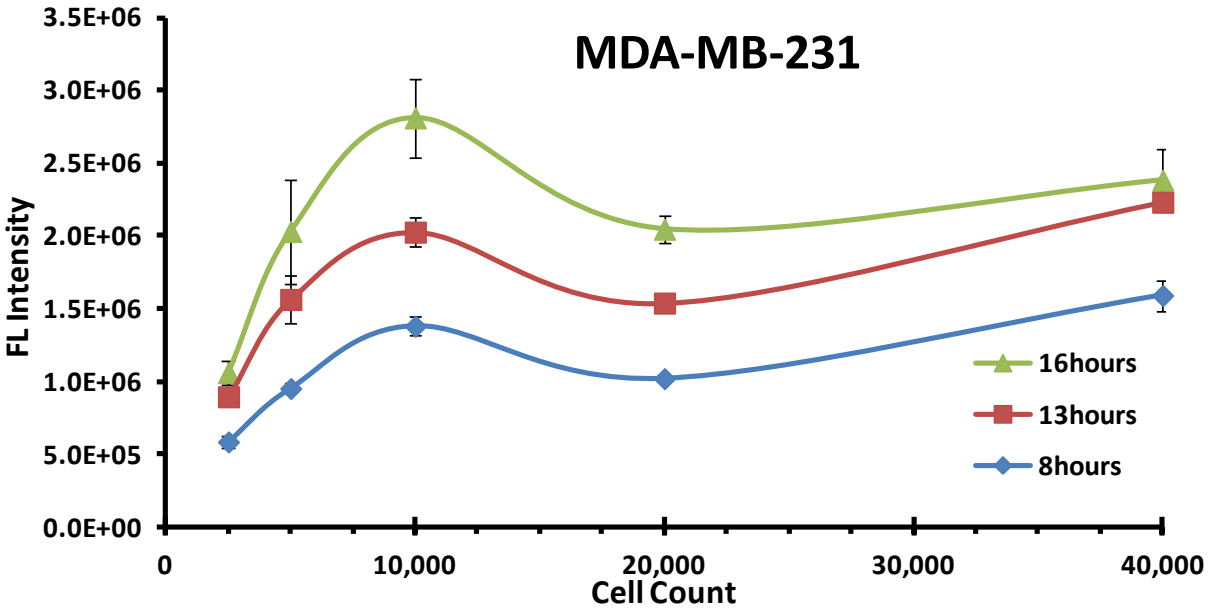


Figure A4.4 Incubation of eight hours for 10,000 cells with the alamarBlue® assay was preferred due to the higher fluorescence intensity and smaller standard deviation.



Figure A4.5 *In vivo* hyperthermal experiments were conducted in a 96 well-plate.

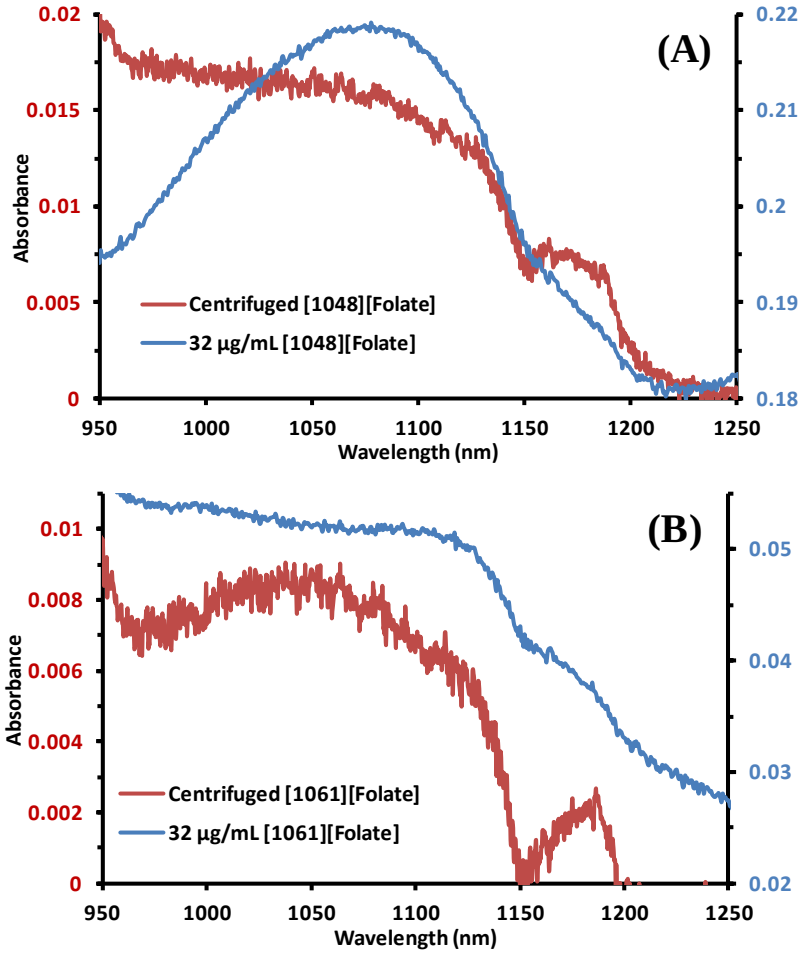
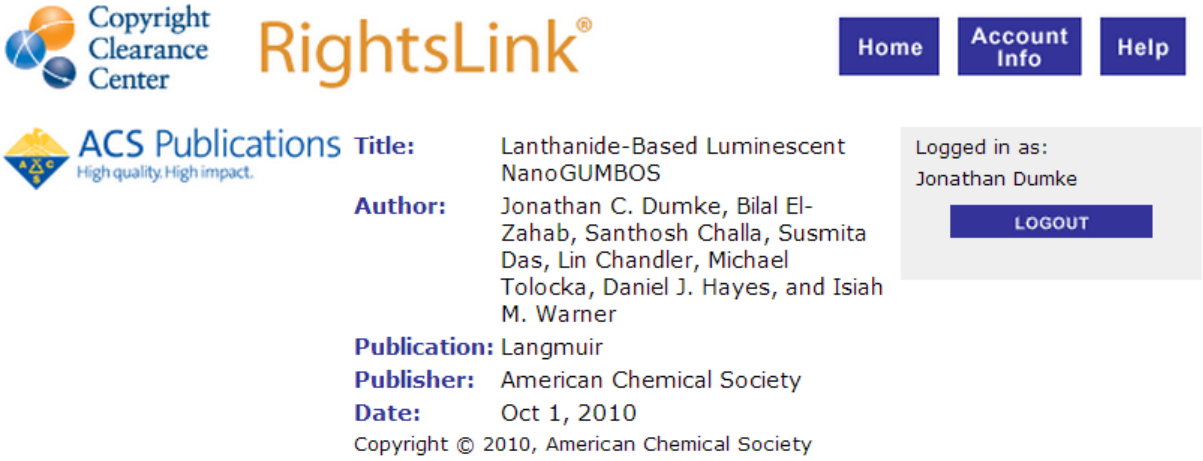


Figure A4.6 Absorbance measurements were conducted for comparison of a fixed concentration (32 µg mL^{-1}) and of the top aqueous layer of post-centrifugation nanoGUMBOS. (A) [1048][Folate] was calculated to be 92.92% insoluble, and (B) [1061][Folate] was calculated to be 88.75% insoluble. (Note: Absorbance shoulder between 1150-1200 nm was determined to be from the folate anion.)

Appendix 3. Letter of Permission



Copyright Clearance Center RightsLink®

Home | Account Info | Help

ACS Publications High quality. High impact.

Title: Lanthanide-Based Luminescent NanoGUMBOS

Author: Jonathan C. Dumke, Bilal El-Zahab, Santhosh Challa, Susmita Das, Lin Chandler, Michael Tolocka, Daniel J. Hayes, and Isiah M. Warner

Publication: Langmuir

Publisher: American Chemical Society

Date: Oct 1, 2010

Copyright © 2010, American Chemical Society

Logged in as: Jonathan Dumke

LOGOUT

PERMISSION/LICENSE IS GRANTED FOR YOUR ORDER AT NO CHARGE

This type of permission/license, instead of the standard Terms & Conditions, is sent to you because no fee is being charged for your order. Please note the following:

- Permission is granted for your request in both print and electronic formats, and translations.
- If figures and/or tables were requested, they may be adapted or used in part.
- Please print this page for your records and send a copy of it to your publisher/graduate school.
- Appropriate credit for the requested material should be given as follows: "Reprinted (adapted) with permission from (COMPLETE REFERENCE CITATION). Copyright (YEAR) American Chemical Society." Insert appropriate information in place of the capitalized words.
- One-time permission is granted only for the use specified in your request. No additional uses are granted (such as derivative works or other editions). For any other uses, please submit a new request.

BACK | CLOSE WINDOW

Copyright © 2012 Copyright Clearance Center, Inc. All Rights Reserved. Privacy statement.
Comments? We would like to hear from you. E-mail us at customercare@copyright.com

Vita

Jonathan Carver Dumke was born in Southfield, Michigan at Providence Hospital to Carver Albert Dumke and Allison Dumke (Seibold). He has an older sister, Kendra Alpert (Dumke) and brother-in-law Daniel Alpert. On January 11th 2013 he will marry his best friend, Alyce Amber Hopper, adding her to his family. Soon thereafter his birth, the family moved to Tampa, Florida and lived there for 12 years until his father was transferred to Dearborn, Michigan in which he lived there throughout academic grades 6 – 12. Attending Dearborn High School, he was very active in varsity athletics (i.e. football, swimming, and baseball) and chemistry experiments with his high school teacher, Mr. Thomas Brown. After synthesizing and successfully "reacting" ammonium triiodide he became engaged in learning more about chemistry leading him to take advanced placement (college credit) chemistry. Jonathan's actions in swimming and chemistry experiments were his driving force for picking colleges.

Jonathan attended Hillsdale College (Hillsdale, Michigan) after he graduated high school in 2001. He was a student of the Tae Park Tae Kwon Do – Anderson Institute (ultimately receiving his 1st Dan black belt under 6th Dan Senior Master Brian Anderson) and NCAA II swimming team. Jonathan joined the Alpha Tau Omega – Beta Kappa chapter in the spring of 2002 where throughout his tenure at Hillsdale College has been chosen to be social chairman and president of the fraternity.

Jonathan was mentored by three amazing professors in the chemistry program at Hillsdale College, Drs. Mark Nussbaum, Chris VanOrman, and Lee Baron. While in the chemistry program he was chosen to be president of the American Chemical Society – Student Affiliates. In 2004, Jonathan started his undergraduate research under the guidance of Dr. Nussbaum titled, "Adaptation of a Commercial Capillary Electrophoresis Instrument for Chemiluminescence

Detection." This work was published in the American Chemical Society journal, Analytical Chemistry in 2007. While Jonathan was working towards his bachelor of science in chemistry, he also worked as a pharmacy technician in Hillsdale at Rite Aid Pharmacy and a local pharmacy called Nash Drugs.

Graduating from Hillsdale College in the spring of 2006 he started work as a quality control technician at the adhesive and coating company, N.D. Industries in Troy, Michigan. Within a few months he was promoted to research associate and successfully lowered the pre-cure volatility of an adhesive (proprietary).

Jonathan started his graduate studies in the fall of 2007 at the Louisiana State University joining the Isiah M. Warner research group. Under the guidance of Isiah Warner, Jonathan gained his erudition on luminescence studies of organic salts in the nanoregime. He has since been president of the Chemistry Graduate Student Council, mentored an undergraduate, teacher-assistantships, received travel awards, presented (oral and poster) at government and non-government conferences, ACS session chair for a conference, published, and acknowledged for a chapter editorial. Jonathan will graduate with the degree of Doctor of Philosophy in chemistry at the Louisiana State University in December 2012. His accomplishments are listed below:

Publications

1. **Dumke, J. C.**; El-Zahab, B.; Challa, S.; Das, S.; Chandler, L.; Tolocka, M.; Hayes, D. J.; Warner, I. M. Lanthanide-Based Luminescent NanoGUMBOS. *Langmuir* **2010,** *26 (19),* 15599-15603.
2. **Dumke, J. C.**; Nussbaum, M. A. Adaptation of a Commercial Capillary Electrophoresis Instrument for Chemiluminescence Detection. *Anal. Chem.* **2007,** *79 (3),* 1262-1265.

3. **Dumke, J. C.**; Hamdan, S.; El-Zahab, B.; Li, M.; Das, Susmita, Hayes, D. J.; Rupnik, K.; Warner, I. M. The Photothermal Response of Near-Infrared NanoGUMBOS (*in preparation*)
4. **Dumke, J. C.**; Qureshi, A.; El-Zahab, B.; Li, M.; Fernand, V.; Das, S.; Hayes, D. J.; Warner, I. M. Tumor-Targeting Hyperthermal Near-Infrared NanoGUMBOS (*in preparation*)

Acknowledgement

1. Bünzli, J.-C. G.; Eliseeva, S. V. Basics of Lanthanide Photophysics. In *Lanthanide Luminescence: Photophysical, Analytical, and Biological Aspects*, 1st ed.; Hänninen, P.; Härmä, H., Eds. Springer: Berlin, 2011; Vol. 7, pp 1-45.

Professional Presentations

Oral

1. **Dumke, J. C.**; Qureshi, A.; El-Zahab, B.; Li, M.; Fernand, V.; Das, S.; Hayes, D. J.; Warner, I. M. "Tumor-Targeting Hyperthermal Near-Infrared NanoGUMBOS," presented at the 68th Southwest Regional Meeting of the American Chemical Society, Baton Rouge, November 4-7, 2012.
2. **Dumke, J. C.**; Qureshi, A.; El-Zahab, B.; Li, M.; Boldor, D.; Hayes, D. J.; Warner, I. M. "Hyperthermia Cancer Therapy Using Near-Infrared GUMBOS Nanoparticles," presented at the 66th Southwest and 62nd Southeastern Regional Meeting of the American Chemical Society, New Orleans, Nov. 30-Dec. 4, 2010.

Poster

1. **Dumke, J. C.**; De Rooy, S. L.; Wright, A.; Jordan, A. N.; Magut, P. K. S.; Hamdan, S.; Warner, I. M. "Applications of GUMBOS for NanoTechnology," presented at the 9th

NanoTechnology for [Department of] Defense (NT4D) Conference, Bellevue, October 24-27, 2011.

2. **Dumke, J. C.**; Qureshi, A.; El-Zahab, B.; Li, M.; Boldor, D.; Hayes, D. J.; Warner, I. M. "Hyperthermia Cancer Therapy Using Near-Infrared GUMBOS Nanoparticles," presented at the 8th Annual Nanotechnology for [Department of] Defense (NT4D) Conference, Atlanta, May 3-6, 2010.
3. Allen, A.; **Dumke, J. C.**; Warner, I. M. "A Disulfide Cross-linked Nanogel for the Thermal Insulation of a Hyperthermal Therapeutic," presented at the LSU Summer Undergraduate Research Forum (SURF) Forum, Baton Rouge, Louisiana, July 29, 2010.

Certifications

- Institutional Animal Care and Use Committee (IACUC) Certified
- OSHA Blood Borne Pathogen Standard Certified
- Trained in proper Laser Safety up to Class IV lasers

Awards and Nominations

2012 – Presided over the General – Analytical Section for the 68th Southwest Regional Meeting of the American Chemical Society, Baton Rouge, November 6th 2012.

2011 – Graduate School Coates Conference Travel Award (NT4D)

2010 – Graduate School Coates Conference Travel Award (NT4D)

2009 – Nominated for the International Workshop on Nanomaterials and Functional Materials Workshop, Campinas, Brazil, August 9-11, 2009.